Internal Report
DESY F35-92-01
January 1992

Hamburg DESY

Influence of Calorimeter Calibration Errors on the Measurement of Deep Inelastic Scattering

by

T. Woeniger

Influence of Calorimeter Calibration Errors on the Measurement of Deep Inelastic Scattering

DISSERTATION
zur Erlangung des Doktorgrades
des Fachbereiches Physik
der Universität Hamburg

vorgelegt von

Torsten Woeniger
aus Hamburg

Hamburg 1991

Abstract

The uranium scintillator calorimeter of the ZEUS detector is designed to achieve the best possible energy resolution for hadrons. Therefore the problems of calibration, stability, homogenity and other systematic effects are of special importance. An analysis of these problems, based on tests and measurements, is presented and an evaluation of the systematic errors is given. A calibration tool using muons has been developed. It uses a fit to the energy loss spectra with a Landau function and achieves a precision for the calibration with muons which corresponds to the precision with electrons.
Finally the influence of the limited energy resolution noise and calibration errors on the reconstruction of deep inelastic scattering parameters is investigated in a Monte Carlo study.

Zusammenfassung

Das Uran-Szintillator Kalorimeter des ZEUS-Detektors ist auf die beste mögliche Energieauflösung für Hadronen ausgelegt worden. Dadurch sind Probleme wie die Kalibration, Stabilität der Signale und Homogenität von besonderer Bedeutung. Diese Probleme sind mit Tests und Messungen untersucht worden. Im weiteren wurde eine Methode zur Kalibration mit Muonen entwickelt. Die Methode benutzt den Fit der Landau Funktion an das Energiespektrum von Muonen. Damit ist die Kalibration mit Muonen mit einer Genauigkeit möglich wie sie vorher mit Elektronen erzielt wurde.
Abschließend wird der Einfluß der limitierten Energieaufösung, von Rauschen und Kalibrationsfehlern auf die Rekonstruktion der Parameter der tiefinelastischen Streuung mit einer Monte Carlo Studie untersucht.

Contents

Abstract I

Zusammenfassung I

1 Introduction 1

2 The ZEUS - Detector 4
- 2.1 Requirements for HERA Detectors 4
- 2.2 Components of the ZEUS Detector 5
  - 2.2.1 Central Tracking System 5
  - 2.2.2 Hadron Electron Separator (HES) 8
  - 2.2.3 High Resolution Calorimeter 8
  - 2.2.4 Backing Calorimeter (BAC) 9
  - 2.2.5 Muon Chambers 9
  - 2.2.6 Leading Proton Spectrometer (LPS) 9
  - 2.2.7 Luminosity Monitor 10

3 Data Acquisition and Trigger System 11
- 3.1 Overview 11
- 3.2 First Level Trigger (FLT) 13
- 3.3 Second Level Trigger (SLT) 16
- 3.4 Eventbuilder (EVB) 16
  - 3.4.1 Concepts for a Transputer Based Eventbuilder 18
  - 3.4.2 Structure of the Eventbuilder 21
  - 3.4.3 Performance 22
- 3.5 Third Level Trigger (TLT) 22

4 Calorimetry 25
- 4.1 Electromagnetic Showers 27
- 4.2 Hadronic Showers 31
- 4.3 Energy Resolution of Sampling Calorimeters 33
  - 4.3.1 Energy Resolution for Electromagnetic Showers 33
  - 4.3.2 Energy Resolution for Hadronic Showers 33

5 The ZEUS Calorimeter 36
- 5.1 Principle 36
- 5.2 Layout of the ZEUS Calorimeter 36
  - 5.2.1 Overview 36
  - 5.2.2 Description of a (FCAL-)Module 37
  - 5.2.3 Readout 44
- 5.3 Digital Card 46
- 5.4 Calibration Constants 47

6 Calibration of the ZEUS Calorimeter 52
- 6.1 Beam Independent Calibration Methods 52
  - 6.1.1 Overview 52
  - 6.1.2 Random Triggers 52
  - 6.1.3 Light Pulser System 53
  - 6.1.4 Cobalt Source Calibration 53
  - 6.1.5 Uranium Signal (UNO) 54
  - 6.1.6 Complete Off Beam Calibration Procedure 56
- 6.2 Absolute Energy Calibration With Beam Particles 56
  - 6.2.1 Experimental Setup of the Beam Tests 56
  - 6.2.2 Calibration With Electrons 59
  - 6.2.3 Other Tests With Electrons 62
  - 6.2.4 Tests With Hadrons 64
  - 6.2.5 Calibration With Muons 65

7 A High Precision Calibration Procedure with Muons 66
- 7.1 Motivation 66
- 7.2 Energy Loss of Muons in Matter 67
- 7.3 Fitting the Energy Distribution 71
- 7.4 Estimation of the Mean Values 72
- 7.5 Results for the FCAL and RCAL Modules Calibrated at CERN 73

8 Influence of Mechanical Tolerances on the Calorimeter Response 76

9 Reconstruction of Deep Inelastic Scattering Parameters 81
- 9.1 Introduction 81
- 9.2 Determination of Structure Functions 81
  - 9.2.1 Elastic Electron Proton Scattering 81
- 9.3 Deep Inelastic Scattering Cross Sections 82
  - 9.3.1 Determination of Structure Functions 83
- 9.4 Reconstruction Methods for DIS Variables 84
  - 9.4.1 Topology of NC-Reactions 85
  - 9.4.2 Reconstruction Using the Electron and the Current Jet 85
  - 9.4.3 Reconstruction With the Method of Jacquet and Blondel 88
- 9.5 Influence of the Detector on the $x - y$ Reconstruction 88
  - 9.5.1 Introduction 88
  - 9.5.2 Results 90
  - 9.5.3 Summary 103
- 9.6 Effects of Calibration Errors and Noise 108
  - 9.6.1 Noise 109
  - 9.6.2 Calibration Uncertainties 111
- 9.7 Summary of Reconstruction Errors 118

10 Conclusion 119

A Software Environment for the Monte Carlo Studies 120
A.1 Software Structure 120
A.2 Cuts to Remove Corrupted Events due to Monte Carlo Errors 120

B Parameters Chosen for the LEPTO Event Generator 125

C Comparison of Chi-Square and Maximum Likelihood Fits 126

D Data for Noise and Calibration Uncertainties 126

E Acknowledgements 137

List of Figures

1 Accessible range of x and Q^2 of HERA 2
2 Isometric view of the ZEUS detector 3
3 Maximum possible jet energy due to the HERA kinematics versus the polar angle θ 3
4 Cross section of the ZEUS Detector along the beam 6
5 Tracking System of ZEUS (sideview) 7
6 Cut transverse to the beam through the CTD 7
7 The three drift chambers of the FTD 8
8 Overview of the ZEUS trigger and data acquisition system 12
9 Timing scheme of the ZEUS trigger system 13
10 Schematic logic in the GFLT-Box 14
11 ZEUS eventbuilder 17
12 Functional principle of an eventbuilder with a ring structure 19
13 A barrelshifter with four states 20
14 Third Level Trigger System 24
15 Energy loss due to ionization 26
16 Energy loss of electrons in lead (from [FAB87]). The unit L_{rad} corresponds to the radiation length X_0 defined in the text. 28
17 The absorption coefficient of lead in cm^2/g for γ-rays, as a function of energy (from [PER82]) 29
18 The longitudinal development of an electromagnetic shower started by 10 GeV electrons (from [Wig86]) 30
19 Development of the inter- and intranuclear cascade in a hadronic shower [BRU87]) 31
20 Energy deposition of a hadronic shower in a uranium scintillator calorimeter . 32
21 Dependence of the constant term of the intrinsic fluctuations on the e/h ratio 34
22 Solid angle coverage of the ZEUS calorimeter 37
23 Front view of the FCAL 38
24 Front view of the RCAL 39
25 An isometric view of the largest FCAL module type 40
26 C-frame 41
27 Schematic overview of the readout with WLS 42
28 Correction pattern for the scintillator 42
29 Cassette for the readout with WLS 43
30 Schematic view of the Analogue card 44
31 Charge as a function of particle momentum for the high and low gain 45
32 Scheme of a ZEUS digital card 46
33 Pulse shape with the 8 sampling points 49
34 Off beam calibration apparatus 53
35 Cobalt scan along an EMC section of the FCAL 54
36 Decay steps for U238 55
37 Setup of the trigger system at CERN 57
38 Trigger counter B3 to veto beam halo particles 57
39 Support frame for the calibration of the FCAL and RCAL modules 58

40 DAQ and control system for the FCAL and RCAL calibration 59
41 Energy distribution with high statistics, obtained by superimposing the events (15 GeV electrons) of all sections of one module 60
42 FCAL module deviations from linearity as a function of the electron energy . 61
43 Deviations from linearity for a RCAL module as a function of the electron energy 62
44 Uniformity scan along a FCAL module with 15 GeV electrons 63
45 Energy resolution for electrons of a FCAL module at different energies 63
46 Lateral distribution of 30 GeV/c hadron showers 64
47 Energy distribution of muons over all EMC sections of all 6 FCAL modules calibrated at CERN 66
48 Vailov function for $\beta^2 = 0.9$ and the Landau function L (from [SEL62]) . . . 68
49 Energy distribution of the muon signal in the FCAL, compared with a Landau distribution. Left: using the data of one HAC1 tower and right: using the data of all HAC1 towers. 69
50 Enery loss of muons in uranium (from [LOH85]) 70
51 Moyal fit to one HAC1 tower (left) and to all HAC1 towers (right) 71
52 Variation of the parameter W (left) and S (right) 72
53 Depth-dose curve determinated by dosimetric film exposure (from [ZEU87]) . 78
54 Event rates of Neutral and Charged Current Reactions at HERA 84
55 Definition of the variables for NC reaction 85
56 Energy versus polar angle for NC-events with $x = 0.2, y = 0.8$ 86
57 x,y reconstruction on event generator level using the current jet 87
58 x,y reconstruction on event generator level using the method of Jacquet Blondel 89
59 Accessible $x - Q^2$ plane of HERA 92
60 Jacquet Blondel on event generator data with theta cut corresponding to the beampipe 93
61 x,y reconstruction with electron of event generator data smeared with calorimeter resolution 95
62 x,y reconstruction with the method of Jacquet and Blondel of event generator data smeared with calorimeter resolution 96
63 x,y reconstruction from the electron of events produced with the ZEUS Monte Carlo without magnetic field and dead material 98
64 x,y reconstruction with the method of Jacquet and Blondel of events produced with the ZEUS Monte Carlo without magnetic field and dead material 99
65 x,y reconstruction with the electron of events produced with the ZEUS Monte Carlo with the magnetic field and no dead material 100
66 x,y reconstruction with the method of Jacquet and Blondel events produced with the ZEUS Monte Carlo with the magnetic field and no dead material . . 101
67 Dead material in front of the calorimeter versus the polar angle θ 103
68 x,y reconstruction with the electron from Monte Carlo data with the magnetic field and with dead material 104
69 x,y reconstruction with the method of Jacquet and Blondel from Monte Carlo data with the magnetic field and with dead material 105
70 x,y reconstruction with the electron from Monte Carlo data with the magnetic field and with dead material via Zephyr 106
71 Summary of the relative errors in x,y for the various simulations 107

72 Noise spectrum of a calorimeter cell 109
73 Noise in the calorimeter 110
74 Relative error on the x-y reconstruction for coherent noise 111
75 Relative error on the x-y reconstruction for incoherent calibration error . . . 114
76 Relative error on the x-y reconstruction due to a coherent calibration error. . 115
77 Relative error on the x-y reconstruction for coherent calibration error of the hadronic sections 116
78 Relative error on the x-y reconstruction for a coherent calibration error of the electromagnetic sections 117
79 Structure of the ZEUS offline software 121
80 Cuts applied to filter events with corrupted electron energy deposition 123
81 Cuts applied to remove events with wrong momentum perpendicular to the beampipe 124
82 Variation of the upper cut with the Chi-Square and the Maximum Likelihood Method 127

List of Tables

1 Event and trigger rates of ZEUS 15
2 Number of channels and amount of data produced by the different components of ZEUS 18
3 Values of the radiation length (X_0) and nuclear interaction length (λ_{int}) for some materials used in calorimeters. 29
4 Approximate size of an electromagnetic shower in some materials 30
5 Approximate size of a hadronic shower in some materials 32
6 List of calibration constants 51
7 The calibration cycle without beam particles performed every 8 hours 56
8 The test cycle with beam particles performed for each module 61
9 Energy loss of 100 GeV muons in the materials of the calorimeter 70
10 Average charge per module in EMC and HAC0 sections 74
11 Average charge per module in the HAC1 sections 74
12 Average charge per module in the HAC2 sections 75
13 Relative thickness variations for the three calorimeter materials for the EMC and the HAC 77
14 Material constants for the parametrization of equation 38 78
15 Normalized fluctuations of the calibration ratios 80
16 Parameters of the event samples at the three selected kinematic regions . . . 89
17 Deviations of mean values and the relative width of x and y with a beampipe cut 91
18 Deviations of the mean values of x and y calculated with a limited energy resolution 91
19 Mean deviations and spread of the reconstructed values of x and y from the generated values for data with no material in front of the calorimeter and the magnetic field switched off 97
20 Mean deviations and spread of the reconstructed values of x and y from the generated values for data with no material in front of the calorimeter and the magnetic field switched on 102
21 Mean deviation of the reconstructed values of x and y from the generated values for data with material in front of the calorimeter and the magnetic field switched on 102
22 Mean deviations and spread of the reconstructed values of x and y from the generated values for data with material in front of the calorimeter and the magnetic field switched on. A cluster algorithm has been used. 108
23 Spread of calibration ratios for all FCAL and RCAL modules calibrated with beam particles at CERN. 112
24 Cuts applied to remove events with Monte Carlo errors 122
25 Results of Mozart test runs with single particles 125
26 Relative errors of the x-y reconstruction due to the uncorrelated noise 128
27 Relative errors of the x-y reconstruction due to correlated noise 128
28 Relative error of the x-y reconstruction due to a random calibration error . . 129
29 Relative error of the x-y reconstruction due to a common calibration error . . 129

30 Relative error of the x-y reconstruction due to a wrong calibration of the hadronic sections 130
31 Relative error of the x-y reconstruction due to a wrong calibration of the electromagnetic sections 130

1 Introduction

HERA is the first high energy storage ring for electrons and protons. With a circumference of 6336 m HERA will provide *ep*-collisions with an electron energy of 30 GeV and a proton energy of 820 GeV.

Now completed, HERA will allow a new generation of scattering experiments, vastly improving the resolution with which the interior of the proton can be investigated. This is demonstrated in figure 1, which shows the large accessible kinematic range of HERA.

The top left corner of figure 1 from [FEL87] shows the area in $x - Q^2$ which has been investigated by present experiments.

The dashed area from the bottom left to the right top corner is the new area which will be accessible with HERA. The figure shows that HERA offers a kinematic region which is expanded by about two orders of magnitude in each of the variables.

The kinematical region where structure functions can be reconstructed with the required accurracy depends critically on the precision of the detector. The ZEUS detector at HERA has been designed with the aim to achieve the best possible energy measurement of electrons and jets in deep inelastic scattering events.

Therefore considerable effort has been invested to develop a calorimeter using uranium and szintillator as calorimeter materials. It has a relative energy resolution for hadrons of $\sigma/E \sim 35\%/\sqrt{E}$, where the energy E is measured in GeV. At an energy of 100 GeV one can therefore in principle measure jet energies with an accuracy of 3.5 %. However, one can only make use of this good energy resolution, if systematic errors and systematic effects arising from calibration errors, nonuniformities, aging effects etc. can be controlled and understood at a level of 1-2%.

Therefore a large effort was done to calibrate the calorimeter. A representative sample of the finished calorimeter modules has been calibrated with particle beams of electrons, hadrons and muons at energies between 10 - 110 GeV at CERN. Before the installation in ZEUS all modules have been checked in a cosmic-ray setup. The setup uses cosmic muons which are produced in the higher parts of the atmosphere. The tower to tower variations of the averaged signals give an indication of the quality of the calorimeter construction. Last not least several calibration methods, which can be done without particle beams, have been foreseen. These make use of the radioactivity of the uranium absorber, which is used as a stable reference signal; in addition radioactive sources and light and charge injection systems are used.

Another method, which in principle allows a continuous control of calorimeter performance and uniformity, uses muons as a source of well defined energy deposition. This method, together with a comparison and intercalibration with other methods will be investigated in this work. The aim is to derive best estimates of systematic errors in the calorimeter measurement, which remain after the various calibration methods have been applied. They can then be used to determine the influence which the remaining errors have on the ability to reconstruct the kinematical variables which describe deep inelastic scattering.

In the first part of the thesis the ZEUS detector will be shown. I did some work for the data acquisition system of this experiment. Therefore this part of the experiment is explained in the following part of the thesis. Then an introduction to calorimetry is given which leads to the calibration of the calorimeter. The calibration of the calorimeter is presented in detail. Finally the consequences of the calibration for the reconstruction of the kinematical parameters (x, Q^2) are investigated.

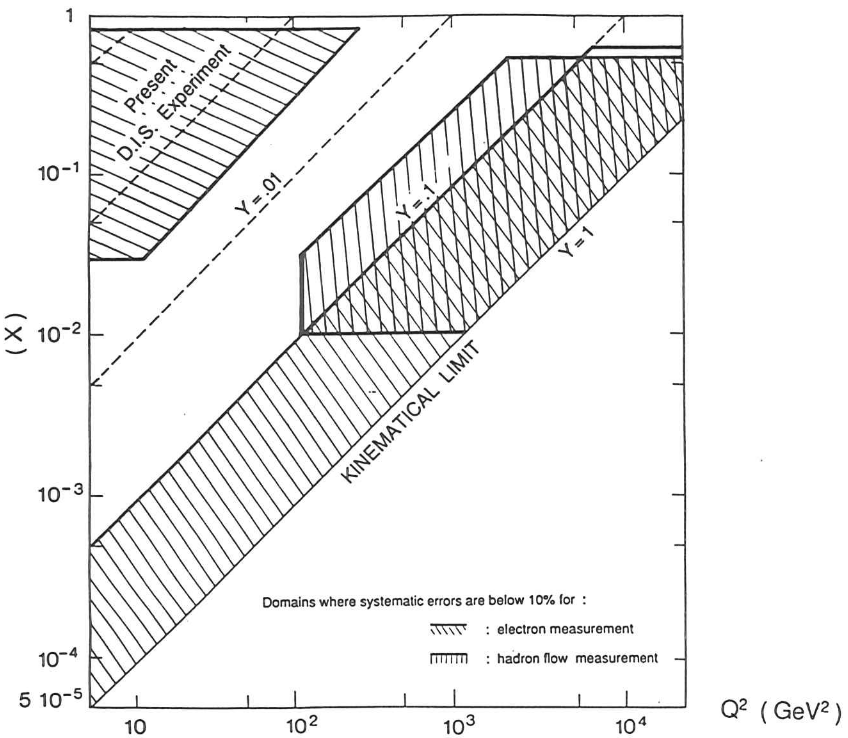

Figure 1: Accessible kinematical range of previous deep inelastic scattering experiments and of HERA, expressed by the kinematic variables x (Bjorken scaling variable) and Q^2 (momentum transfer squared) (from [FEL87])

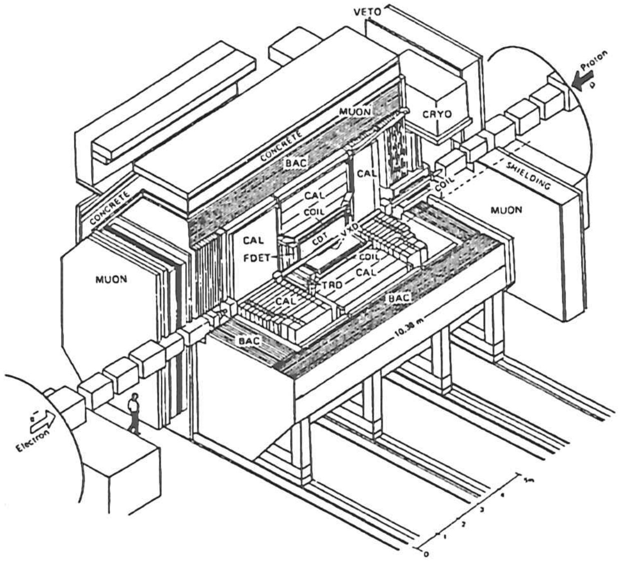

Figure 2: Isometric view of the ZEUS detector

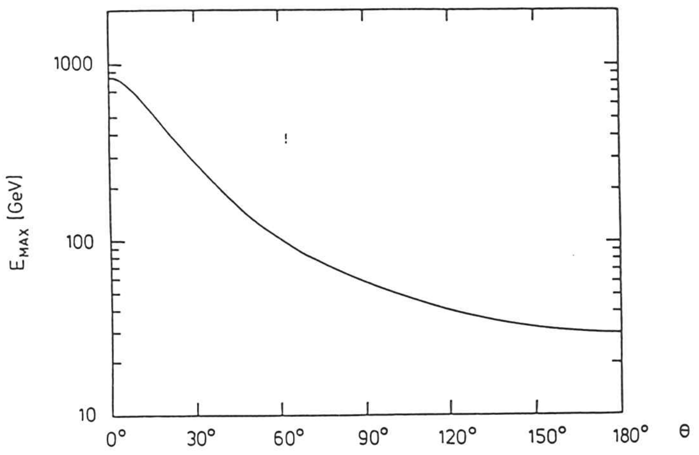

Figure 3: Maximum possible jet energy due to the kinematics of HERA versus the polar angle θ [WOL86]

2 The ZEUS - Detector

2.1 Requirements for HERA Detectors

ZEUS is one of the two general purpose detectors presently being completed. It is shown in figure 2. It consists of several subdetectors called components (CTD, CAL ...) which are specialized to measure certain parameters (position, energy) of the particles coming from the interaction point. From the physics point of view, the two main topics which impose requirements on the detector are

- the structure functions of the proton,
- detection of new particles.

Structure Functions of the Proton: HERA detectors will attempt high precision measurements of the proton structure functions to look for deviations from the predictions of the standard model.
For these investigations, an accurate measurement of the electron in case of Neutral Current events and of the current jet is needed. This requires an electromagnetic and hadronic calorimeter with complete solid angle coverage and with a uniform response for electrons and hadrons. Especially for CC reactions, where the leaving neutrino cannot be measured, an excellent hadron energy resolution is vital.

New Particles New particles may be detected in the mass range between 120 - 200 GeV, if they exist. Examples are

- new; maybe right handed vector bosons,
- excited leptons and quarks (e^*, q^*),
- leptoquarks, a composite of quarks and leptons.

If these particles exist in the given mass range, they will have a very characteristic signature. By tagging the scattered electron, the kinematics of the relevant subsystem is determined; this is a special handle provided for HERA experiments. Like the measurements of the structure functions, the search for new particles requires the measurement of the jet topology and jet energies, and of missing transverse momentum to high accuracy.
Many of the new particles decay into leptons, which therefore provide a signature for new processes. This requires the ability to measure isolated electrons and muons in jets.
As an aspect of all these requirements, figure 3 shows the maximum jet energy which is possible with the HERA kinematics. Jet energies as high as a few 100 GeV can occur. On the other hand jets with 30 GeV must also be measured well; in addition muons which lose only a few GeV must be recognized. Therefore one has extreme requirements for the stability, the accuracy and the dynamical range of the calorimeter, which has to measure these energies. Due to the large difference of proton and electron momentum the HERA events will have a large momentum imbalance and most of the particles go into a small cone around the proton direction; here the detectors have to cope with high particle densities.
Another difficulty is the short bunch crossing time of 96 ns which requires a sophisticated data acquisition and trigger system (section 3).

2.2 Components of the ZEUS Detector

This section gives an overview over the components of the ZEUS detector. They can be seen in the cross section through the detector along the beam (figure 4).

2.2.1 Central Tracking System

Figure 5 shows the tracking system of ZEUS. It consists of a number of drift-chambers, which cover the polar angle from 7.5^0 to 170^0. This is done

- from 7.5^0 to 28^0 by the forward tracking detector (FTD) ,
- from 15.0^0 to 164^0 by the central tracking detector (CTD) and
- from 159^0 to 170^0 by the rear tracking detector (RTD).

The vertex detector (VXD) provides precise tracking information close to the vertex. For the measurement of momenta, the central tracking detectors are surrounded by a superconducting coil which produces a field of 1.8 T.

Vertex Detector (VXD) It is a small time expansion chamber, which has an inside radius of 88 mm and an outside radius of 162 mm. Located directly at the beam pipe the VXD has to cope with high background rates and particle densities.
A spatial resolution of 30 μm allows to recognize short lived particles like D- and B- mesons.

Central Tracking Detector (CTD) Figure 6 shows a cut through the CTD. The CTD is a cylindrical drift chamber with nine super-layers. Each of the super-layers consists of eight planes of sense wires. The CTD provides a resolution of 100 μm in the $r - \phi$ plane. In the $z-$ direction along the axis the resolution is 1.0 to 1.4 mm.

Forward and Rear Tracking Detectors (FTD and RTD) Along the beam axis follow the Forward Tracking Detector (FTD) in the proton direction and the Rear Tracking Detector (RTD) in the electron direction. These are planar drift chambers, which extend the CTD's polar range. They have a resolution of 120 μm.
For the spatial reconstruction of the tracks three different stereo views of the track are provided (see figure 7).

Superconducting Coil A superconducting solenoid with an inside radius of 86 cm produces a magnetic field of 1.8. The coil has a thickness of only one radiation length (X_0) of alumium to minimize interactions of particles with the material of the coil.

Transition Radiation Detector (TRD) The TRD allows a separation between electrons and hadrons for energies of up to 30 GeV with a hadron misidentification of 10^{-2}.
Fibers made from polyethylene are used as a radiator. For the measurement of the signal, a planar drift chamber is used. The gas of the drift chamber, Xe with 10% admixture of carbon dioxide and iso-butane, is sensitive to the X-rays of the transition radiation. One

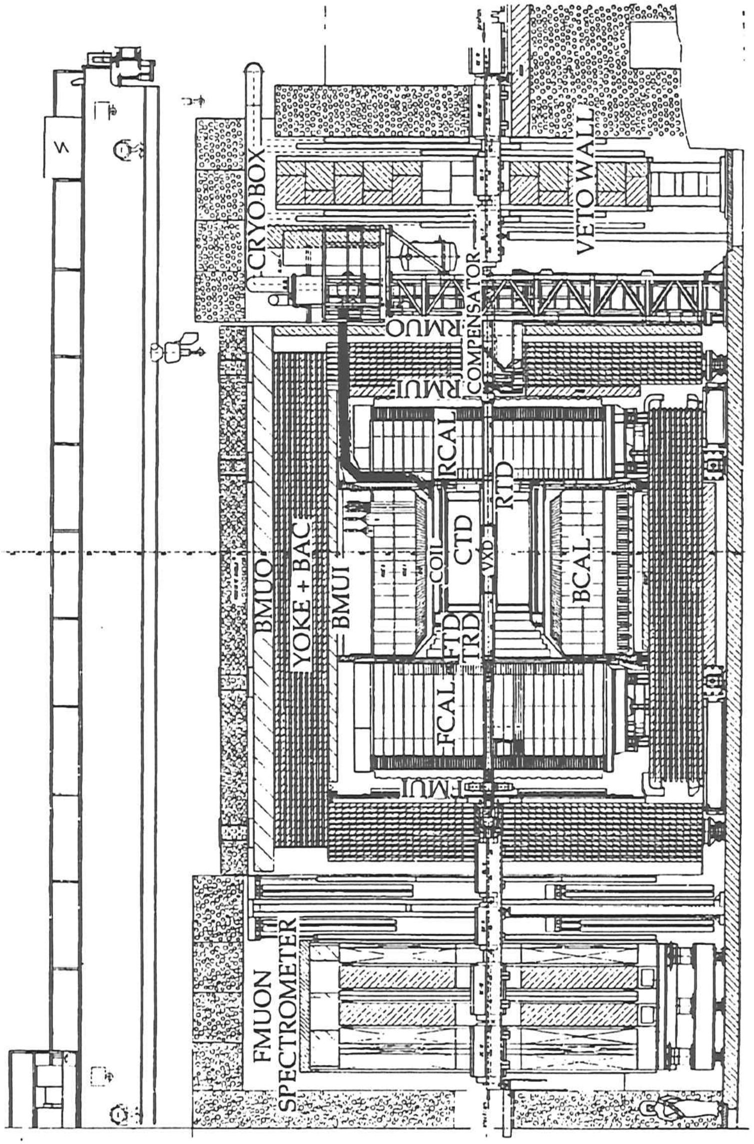

Figure 4: Cross section of the ZEUS Detector along the beam

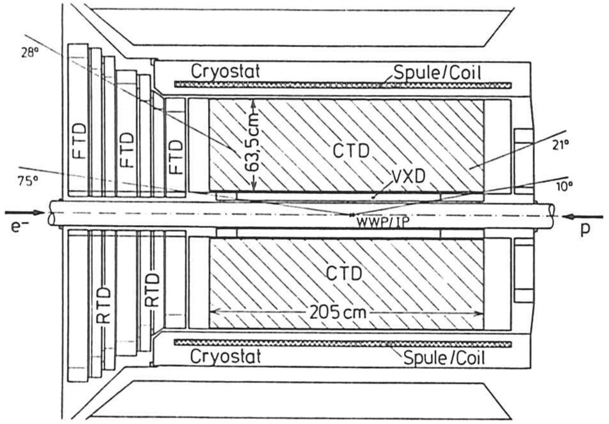

Figure 5: Tracking System of ZEUS (sideview)

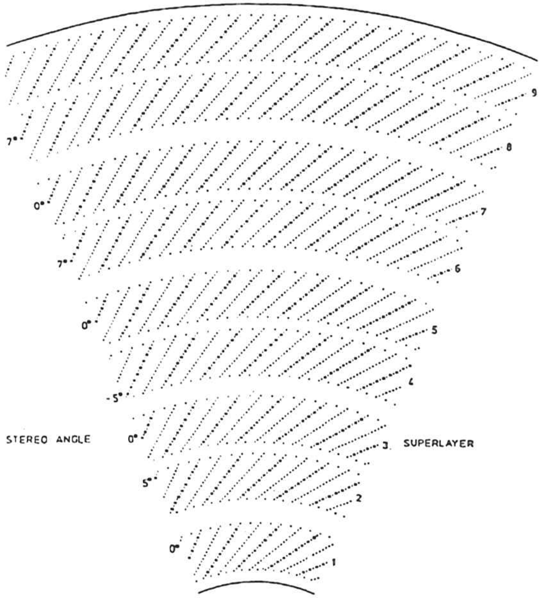

Figure 6: Cut transverse to the beam through the CTD

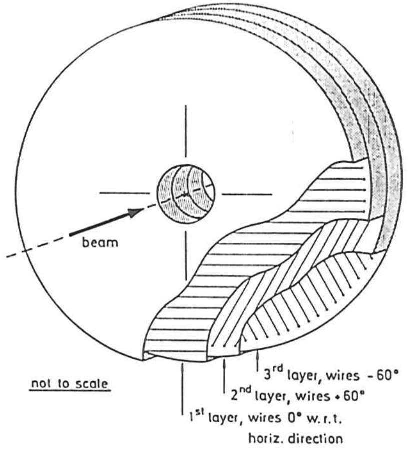

Figure 7: The three drift chambers of the FTD

TRD module consists of a radiator stack followed by a drift chamber.
Four of these modules are combined in two packages of two modules. The two packages are placed between the three chambers of the FTD.

2.2.2 Hadron Electron Separator (HES)

The HES consists of an array of silicon pads size $3 \times 3\ cm^2$ placed after 3 radiation lengths of the electromagnetic sections of the high resolution calorimeter. The HES uses the fact that in a high Z-absorber electromagnetic showers start after much shorter distances than hadronic showers. Thus electrons give a higher signal in the diodes of the HES. This method allows to recognize electrons in a large background of hadrons in a shower, with a hadron misidentification of 10^{-3} above 20 GeV.

2.2.3 High Resolution Calorimeter

A detailed description is given in section 5. Therefore only the main properties are listed here. It is a uranium scintillator sandwich calorimeter with equal response to electrons and hadrons, achieving an energy resolution σ_E of

$$\frac{\sigma_E}{E} = \frac{35\%}{\sqrt{E}} \quad \text{(E in GeV)}$$

for hadrons and hadron jets and

$$\frac{\sigma_E}{E} = \frac{18\%}{\sqrt{E}}$$

for electrons.
The calorimeter is divided into the forward (FCAL), the barrel (BCAL), and the rear calorimeter (RCAL) (see figure 4). Radially the calorimeter is segmented into an electromagnetic and one or two hadronic sections. The angular resolution of the calorimeter should be better than 10 mrad with good electron hadron separation for jets and single particles. Therefore, a transverse segmentation of $5 \times 20cm$ in the forward and barrel electromagnetic

calorimeter (FEMC and BEMC) and of $10 \times 20 cm$ in the RCAL has been chosen. To take advantage of the high intrinsic precision of the calorimeter an absolute calibration of the energy response as well as long term stability and uniformity is required. The aim of the calibration with the natural uranium radioactivity, radioactive sources and beam particles is to provide a long term calibration uncertainty of $\leq 1\%$. Section 6 covers this problem in detail. The depth of the calorimeter was chosen such that for 90 % of the single particles with the maximum energy kinematically allowed in any region of the calorimeter, the energy containment is 95 %.

The bunch crossing time of HERA is 96 ns. Accordingly, readout and signal processing have to cope with the bunch crossing rate of $\approx$ 10 MHz. Readout with plastic scintillators and photomultipliers achieves the required short pulses to avoid pile up effects.

2.2.4 Backing Calorimeter (BAC)

The backing calorimeter is placed in the iron yoke of the detector behind the high resolution calorimeter. Like the high resolution calorimeter, it uses the sandwich principle. Ten layers of iron, each 7.5 cm thick, act as the absorber material. For the readout, the iron is interleaved with proportional tubes. The backing calorimeter, with a depth from 4 to 6 nuclear interaction lengths, has an energy resolution for hadrons of $100\%/\sqrt{E}$. It measures the leakage of energy out of the high resolution calorimeter. It can be used as an offline veto for missing energy or to correct for the energy leaking out of the high resolution calorimeter.

2.2.5 Muon Chambers

The main task of the muon detectors is the identification and momentum measurement of muons.

The forward direction requires a special effort because of the high momentum of the muons and the need for a coverage down to small polar angles. Therefore a spectrometer of layers of toroidally magnetized iron (1.7 Tesla with conventional coils) interleaved with a set of drift chambers is placed there. Limited streamer tubes and time of flight counters provide a trigger. The drift chambers achieve a momentum resolution of

$$\frac{\sigma_p}{p} = 23\% \text{ at } 100 \text{ GeV},$$

with slightly better values at smaller energies.

The barrel and rear muon detectors cover the remaining part of the solid angle. These detectors identify tracks which penetrate the calorimeter and the iron. The measurement of the direction in front and behind the magnetized iron yoke allows the determination of the momentum. This gives a momentum resolution of

$$\frac{\sigma_p}{p} < 30\% \text{ at } 20 \text{ GeV}.$$

2.2.6 Leading Proton Spectrometer (LPS)

The LPS allows a reconstruction of high energy protons emitted in the forward direction inside the beam pipe. It consists of six hodoscopes made of silicon strip detectors, which are placed between 40 and 90 m away from the interaction point in the proton direction.

2.2.7 Luminosity Monitor

In order to measure the luminosity of the storage ring, one uses a reaction with a large and well known cross-section. A convenient reaction is the bremsstrahlung reaction $ep \rightarrow ep\gamma$. The electron is detected by a calorimeter 35 m away from the interaction point while the photon is recognized by a calorimeter close to the proton beampipe 108 m away from the interaction point. The coincidence of the two calorimeters with an energy sum equal to the incident energy of the electron indicates an event. The cross section of the process is well known and the acceptance of the luminosity monitor is close to 100 %.

3 Data Acquisition and Trigger System

3.1 Overview

Figure 8 gives an overview of the ZEUS trigger and data acquisition (DAQ) system. It shows the data flow from the sources, the detector components, to the destination. At the destination the data selected by the three trigger levels are stored on cartridges in the DESY computer center for further analysis.

With the bunch crossing time of 96 ns the data is read from each detector component, e.g. the sense wires of the tracking system or the photomultipliers of the calorimeter and stored in a pipeline for temporary storage, until a first level trigger decision is made. These pipelines have a depth of 5.5 μs. Within this time the first level trigger has to finish the calculation of a single event. As it can be seen in figure 8 the first level trigger (FLT) itself consists of subtriggers (Muon FLT, CTD FLT etc.) which are dedicated to the components and a global first level trigger box (GFLT). Each subtrigger performs a single event analysis and delivers its data to the GFLT. For example the FLT of the calorimeter does some simple cluster finding and forms various energy sums. The FLT of the tracking system does some simple track finding and delivers the resulting information like the number of tracks and the approximate direction to the GFLT. In the GFLT the data from the subtriggers are combined and the GFLT performs then via logical operations a trigger decision which is then distributed to the components. The rate of the first level trigger is expected to be 1000 Hz.

A further trigger processor, called Fast Clear, is foreseen for the calorimeter. It is essentially a cluster finding processor which has up to 15 μs/event to perform its calculations. If the fast clear comes to the decision that a further analysis of an event should not be done, it sends the fast clear command to the GFLT which then stops the readout of the components.

With the issue of the GFLT decision the data is read out from the pipelines and transported to the buffers of the second trigger level. Figure 9 shows that 60 μs after the beam crossing the full digitized information is available for the second level trigger which now can start its calculations. The second level trigger has a similar structure like the FLT. Subtriggers dedicated to the data acquisition system of the components perform local trigger calculations and send their results to the global trigger system. The global second level trigger (GSLT) combines the data sets for the whole detector and carries out the trigger decision. The GSLT decisions are similar to those of the FLT but on a more precise level including also timing information. 2 ms after the beam crossing the GSLT issues its decision. The trigger rate of the GSLT is foreseen to be around 100 Hz.

The GSLT decision is distributed via the eventbuilder to the DAQ systems of the components. These deliver their data to the eventbuilder which combines the data sets of the components to complete detector events. The eventbuilder delivers the data sets to the third level trigger (TLT). This is a microprocessor farm which works on complete detector events and makes further trigger decisions on the basis of a complete event reconstruction. The rate foreseen after the TLT is a few Hz. The data are then stored on magnetic cartridges for offline analysis and distributed to the participating institutes.

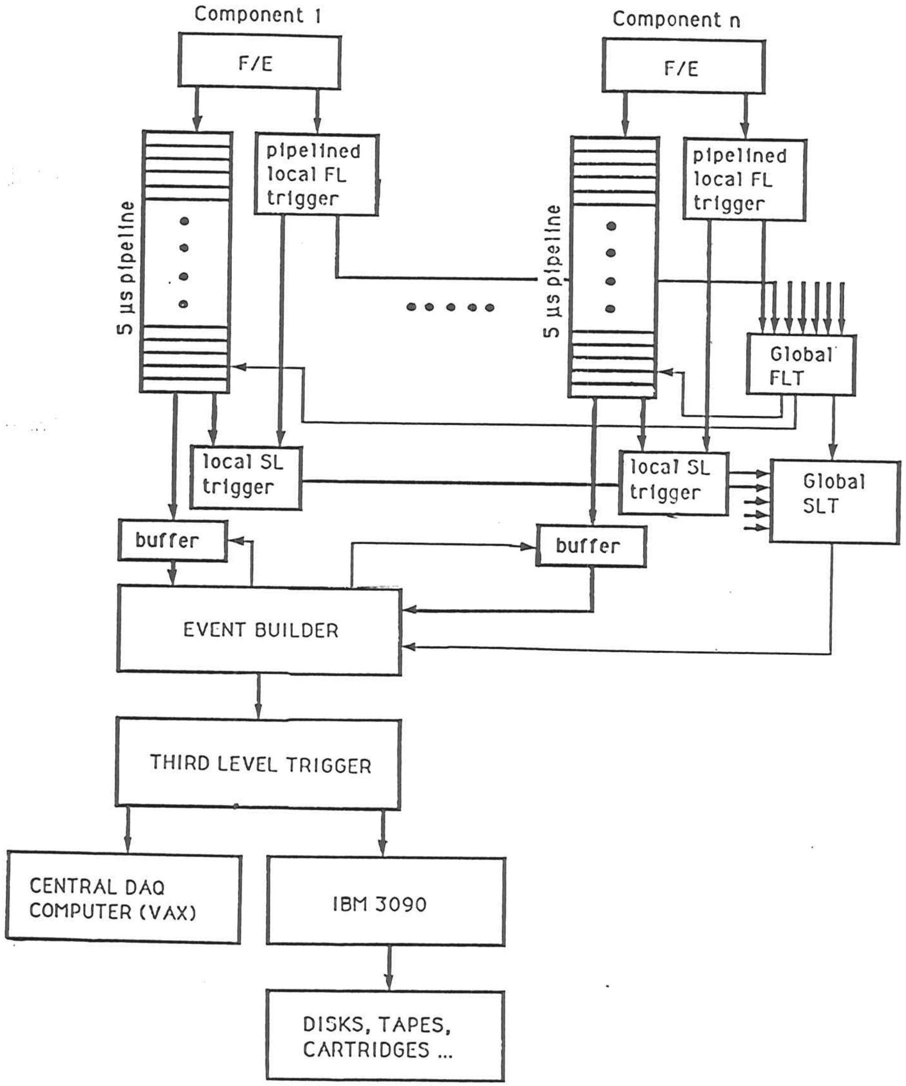

Figure 8: Overview of the ZEUS trigger and data acquisition system

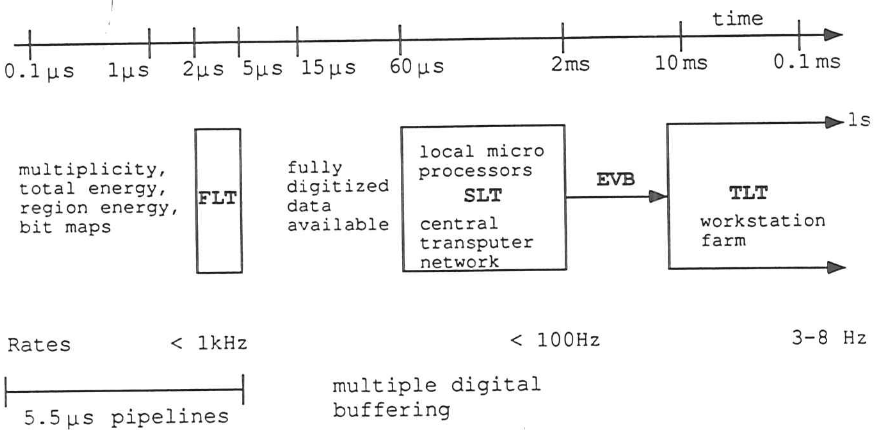

Figure 9: Timing scheme of the ZEUS trigger system

3.2 First Level Trigger (FLT)

The rate of 1 kHz envisaged for the FLT means that only about 0.01% of the beam crossings are accepted. Such a high rejection factor, combined with high efficiency cannot be achieved by a simple strategy.

The local first level triggers which are dedicated to the components have to provide their calculations after 26 beam crossings to the Global First Level Trigger (GFLT). In the GFLT the data passes three logical stages (figure 10). In the first stage, the data from the local FLTs are accepted. These words contain e.g. energy sums from the calorimeters and cluster and track information. The information of the different subdetectors is combined into 8 categories (e.g. Energy, Track, Low Q^2 ...). The information of these categories is correlated to Yes/No flags. For the whole detector there are about 150 flags which indicate, for example, a likely beam gas event or an event with large missing energy.

At the second stage the logical flags from the first stage are combined to logical subtriggers. The sub triggers contain already predictions of the event type like a subtrigger for a muon, a photoproduction event, or an isolated particle.

Finally, the subtriggers are combined via prescalers and a logical OR to the global first level trigger decision. Exactly 46 crossings, or 4.4 μs, after the beam crossing which caused this event, the trigger decision is distributed to the components. A positive decision forces the readout and reset of the pipelines. For components with analog pipelines, the data is digitized at this stage. 60 μs after the beam crossing (figure 9) the data is ready for analysis by the Second Level Trigger (SLT).

Here are some examples of component calculations of the FLT. For the selection of some interesting events their momentum and energy imbalance transverse to the direction of the

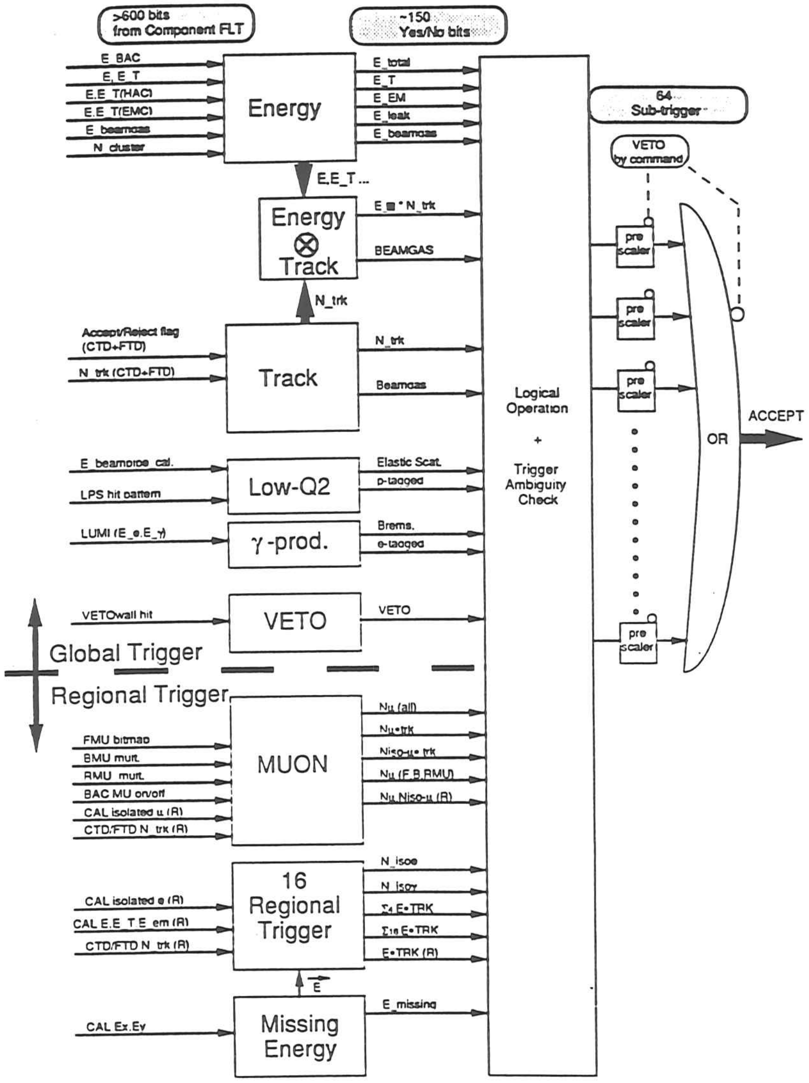

Figure 10: Schematic logic in the GFLT-Box [SMI90]

Event type	σ [nb]	Rate [Hz]		
		No trigger	After FLT	After SLT
VMD	13200.	264.	0.00	0.00
PGF $u\bar{u}$	3807.	76.1	1.40	1.40
PGF $d\bar{d}$	952.	19.0	0.343	0.339
PGF $s\bar{s}$	741.	14.8	0.270	0.267
PGF $c\bar{c}$	396.	7.92	0.760	0.749
PGF $b\bar{b}$	4.36	0.0872	0.0497	0.0490
QCD-Compton u	1546.	30.9	8.55	8.16
QCD-Compton $\bar{u}$	540.	10.8	3.35	3.27
QCD-Compton d	254.	5.08	1.44	1.38
QCD-Compton $\bar{d}$	135.	2.70	0.853	0.840
QCD-Compton s	51.2	1.02	0.263	0.258
QCD-Compton $\bar{s}$	51.2	1.02	0.303	0.296
QCD-Compton c	11.3	0.226	0.0664	0.0657
QCD-Compton $\bar{c}$	11.3	0.226	0.0711	0.0707
NC ($4 \leq Q^2 < 30$)	110.	2.2	0.25	0.24
NC ($30 \leq Q^2 < 100$)	15.	0.30	0.25	0.25
NC ($100 \leq Q^2 < 1000$)	5.1	0.10	0.10	0.10
NC ($Q^2 \geq 1000$)	0.22	0.0044	0.0044	0.0044
CC ($4 \leq Q^2 < 30$)	0.00093	0.000019	0.000004	0.000003
CC ($30 \leq Q^2 < 100$)	0.0028	0.000056	0.000044	0.000035
CC ($100 \leq Q^2 < 1000$)	0.023	0.00046	0.00046	0.00041
CC ($Q^2 \geq 1000$)	0.044	0.00088	0.00088	0.00087

Table 1: Rate of physics events after first and second level trigger cuts, assuming a luminosity of $2 \times 10^{-2} nb^{-1} s^{-1}$ from [BEN91]

beampipe can be used. A typical trigger condition for the FLT which takes this into account is:

$$\begin{array}{c} 0 \text{ FL CTD tracks and } |\vec{p_T}| \geq 5\ GeV/c \\ \text{or} \\ \geq 1 \text{ FL CTD track and either } |\vec{p_T}| \geq 5\ GeV/c \text{ or } E_T \geq 12\ GeV. \end{array} \qquad (1)$$

The influence of this cut on the trigger efficiency can be seen in table 1. The table lists cross sections and trigger rates for vector meson dominance (VMD) events, quark-antiquark production by photon gluon fusion (PGF) events, gluon bremsstrahlung of QCD-Compton events and deep inelastic scattering with neutral and charged current (NC- & CC-) events. To achieve a reduction of the first level trigger rate down to 1 kHz, a Fast Clear (FC) for the calorimeter has been implemented. The calorimeter information of each event accepted by the GFLT is processed by the Fast Clear processor. It can work for up to 20 μs on a more detailed analysis. If the Fast Clear comes to the decision to clear an event and the GFLT has passed this event, the abort command of the fast clear is sent via the GFLT to the components. The command forces then the components to stop the readout of this event.

3.3 Second Level Trigger (SLT)

The second level trigger uses the fully digitized component data. It is a subset of the same data which is used by the offline reconstruction.
Due to this more complete and precise data, tracking, vertex determination, muon, electron and jet finding can be done with more accuracy. Further on global timing information is available for the global second level trigger (GSLT) decision. This allows the rejection of background events which have the wrong timing.
The second level trigger conditions are generally similar to the first level trigger conditions, (condition 1) but they can be more strict due to the higher precision of the available data. For the CTD data of the example above the trigger condition is:

$$\begin{array}{c} \geq 1 \text{ SL CTD track with } p_T \geq 0.3\ GeV/c \\ \textbf{and} \\ |z_V| \leq 45 \text{ cm} \end{array} \qquad (2)$$

z_V is the best estimate of the z-position of the vertex which has been calculated by the SLT with the $z-$axis along the beampipe. Also here the trigger efficiency can be seen in table 1. It is planned that the SLT decision will reduce the trigger rate from 1 kHz down to 100 Hz. Similar to the FLT the SLT consists of two parts, the local second level trigger processors and the Global Second Level Trigger.
Hard- and software of the local SLT depends strongly on the architecture of the component subsystem. At the calorimeter, like at most of the other ZEUS components, the readout is done by a special microprocessor called a transputer (see [VOG90],[WOE90] or [WOE89]). The GSLT combines the results from the local SLTs. The information consists not only of single words but of entire data banks. The GSLT performs consistency checks and does some global calculations. Based on this information, the GSLT decision is calculated. One millisecond after the beam crossing, for which the trigger is issued, the GSLT gives the command to build the event.

3.4 Eventbuilder (EVB)

After the issue of a positive GSLT decision, the event data is transported by the component subsystem to the interface between the component and the eventbuilder. Until now, all the data for one physical event is still scattered over the local memories of several data acquisition systems. At this point the eventbuilder has to be involved; it combines component data into a single event for the analysis by the TLT.
Seventeen components deliver their data asynchronously to the eventbuilder. The data from each component (table 2) ranges in size from 0.01 to more than 30 kbytes, which results in a combined event size between 100 and 140 kbytes. All the data arrives with the trigger rate of the GSLT, i.e. 100 Hz. Using an average event length of 100 kbyte, this leads to a data rate of about 10 Mbyte/s.
To avoid any bottleneck, the performance of the eventbuilder has to be well above the requirements for this average data throughput. Thus, it has to have an overall band width of at least 20 Mbyte/s and be able to cope with trigger rates above 100 Hz.

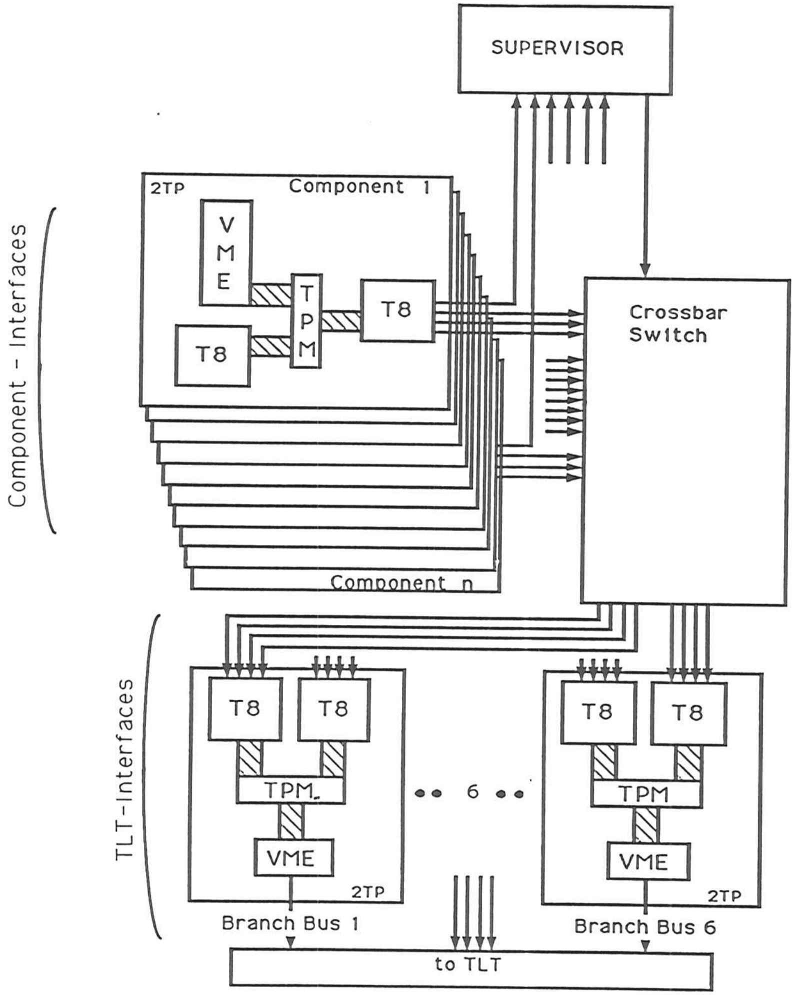

Figure 11: ZEUS eventbuilder

Detector Component		Channels	Event Length [kB]
Central Tracking Detector	(CTD)	4 608	10 - 30
Forward/Rear Tracking Detector	(FTD/RTD)	5 778	10 - 15
Barrel Calorimeter	(BCAL)	5 184	5 - 20
Forward Calorimeter	(FCAL)	4 344	5 - 20
Rear Calorimeter	(RCAL)	2 336	5 - 10
Transition Radiation Detector	(TRD)	2 472	5 - 10
Hadron Electron Separator	(HES)	37 304	5 - 10
Backing Calorimeter	(BAC)	40 000	2
Vertex Detector	(VXD)	832	2
Beamline			1
Barrel Muon Detector	(BMUON)	62 256	0.6
Forward Muon Detector	(FMUON)	18 948	0.5
Rear Muon Detector	(RMUON)	22 080	0.3
Leading Proton Spectrometer	(LPS)	52 000	0.2
Luminosity Monitor	(LUMI)		0.2
Vetowall			0.01
Global Second Level Trigger	(GSLT)		10 - 20
	Sum:	258 142	62 - 142

Table 2: Number of channels and amount of data produced by the different components of ZEUS

3.4.1 Concepts for a Transputer Based Eventbuilder

The task of the eventbuilder is: *to combine the data from the components to a complete detector event and transport it to the third level trigger.*
Several logical concepts are possible to accomplish this task. A straight forward approach would would use a common bus system which connects all data sources and sinks with each other. But a commercially available bus system with the required bandwidth would not be able to transport the data over a distance of more than a few m. Optical high speed connections which in principle would provide the required bandwidth over the needed distance exceed the alloted costs by at least one order of magnitude.
Taking all constraints into account like commercially available hardware, costs, reliability over longer distances most of the straightforward solutions turn out to be not possible. A further input for the design considerations is that most of the ZEUS data acquisition and trigger systems (tracking, calorimeter, ...) and the trigger (GSLT) are based on transputers which suggest a solution using transputers.
Transputers are powerful microprocessors with a flexible interprocessor communication facility. Each transputer has four bidirectional communication lines, the links. Processor networks, the basis of any up to date data acquisition system, can be built with transputers in a very smart way.
Compatibility considerations made is desirable to use transputers also in the eventbuilder. Transputers combine a high computing power with a fast interprocessor communication facility. A high performance of both is needed for the eventbuilder.
In an extensive study solutions for a transputer based eventbuilder have been investigated.

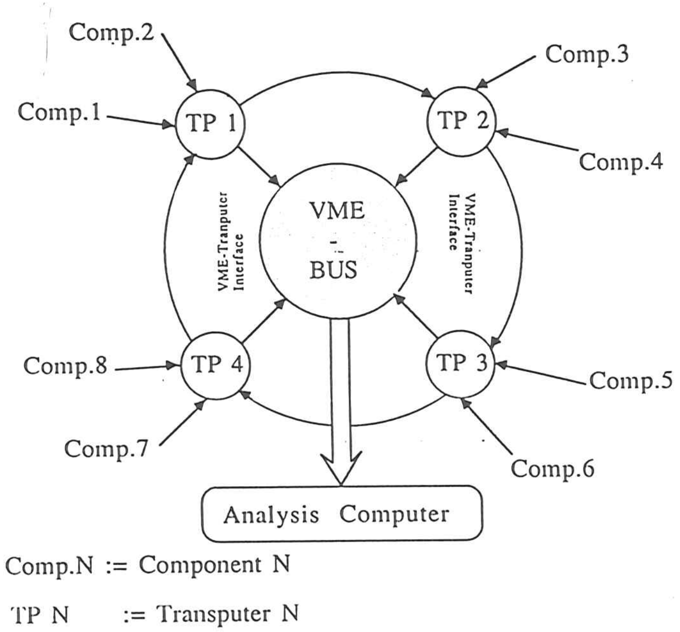

Figure 12: Functional principle of an eventbuilder with a ring structure

Three possible solutions have been studied in more detail. These are

- an eventbuilder with a ring structure,
- an eventbuilder with a barrelshifter and
- an eventbuilder with a crossbar switch.

Eventbuilder With a Ring Structure: The basic principle of an eventbuilder based on token ring architectures is shown in figure 12. The involved transputers are connected with one another in a ring. In the case of a standard transputer two links will be free for the incoming data of the components. The transputers are receiving permanently data from the detector components which have to be transported to the analysis computer. All transputers of the ring structure are connected to a common bus system via dual ported memories (DPMs). At ZEUS the VME-bus is used. The idea of this eventbuilder is the following. While the communication between the transputers is done by the ring, the data sets are written from the components into the DPMs. From the DPMs the data is read out by a DMA controller over the common bus system and transfered to the analysis computer. The solution requires a relatively small amount of hardware for data rates which can be handled with one common bus system. Three bottlenecks are in this concept: the message passing through the ring, the rate with which the DPMs can be read out via the VME bus and the data transport to the analysis computer. With the hardware used at ZEUS the readout speed of the DPMs via the VME-bus ($\approx 8Mb/s$) cause the limitation. The data of ZEUS would require more than one common bus. With the use of more than one common bus the concept loses the advantage of a relatively small hardware effort.

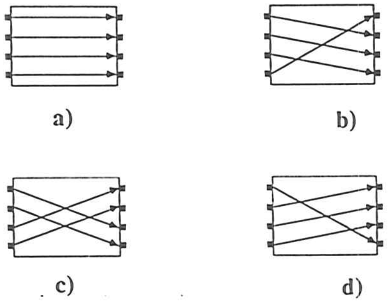
a) b) c) d)

Figure 13: A barrelshifter with four states

Eventbuilder With a Barrelshifter: The functional principle of a barrelshifter is shown in figure 13. In order to simplify the explanation assume that there are just four data sources and four data destinations. In our case the data sources are the components and the data destinations are the analysis computers (TLT-nodes).
The idea is that the data lines from the sources to the destinations have to be cyclically changed. After four of these changes the system is again in the initial state. During this full switch period each source was connected with each destination. This means that each destination was able to get the required data from each source. Such a switching network can be constructed with a transputer network.
A big advantage of this concept are the easily foreseeable states of the system. Due to this the switching can be done very fast using simple and fast hardware. But this leads only to a high data throughput if the data, which go into the eventbuilder have approximately the same size, because the switching only occurs when the last block of every component has passed this system. And even for normal running each front end needs buffers for as many events as there are front ends.

Eventbuilder With a Crossbar Switch: In this concept each of the components and each of the TLT nodes is connected to a crossbar switch. The crossbar switch is controlled by a central scheduler. The result of a study [WOE90] is that an eventbuilder with a crossbar is the preferred solution because it provides the following advantages:
As far as possible, it avoids bottlenecks in the data flow. The data is transported over several

links in parallel. This and the possibility to reconfigure the network during the operation offers a high redundancy against hardware errors. This is very important if one considers the central position of the eventbuilder in the ZEUS online system (see figure 8).
The modular structure (figure 11) with the front end, back end, supervisor and the crossbar switch offers the possibility to adopt the performance to changing requirements. For example it is possible to include an additional component into the system only by adding a new front end card for this component. The data transfer over the long distance between the crossbar and the TLT nodes (80 m) is done via optical cables. These are very insensitive against all kinds of noise, which is an important advantage if one considers the conditions in the rucksack with a large number of processors, fans and power supplies.

3.4.2 Structure of the Eventbuilder

Figure 11 shows an overview of the ZEUS eventbuilder. The eventbuilder consists of four modules

front end , which receives the data from the components,

supervisor , which gets the information which data packages are received by the front end and controls the

crossbar switch , which transports the data from the data sources (front end) to the data sinks the

back end , which delivers complete events to the TLT.

Front End The front end of the eventbuilder consists of the interfaces between the eventbuilder and the components. It is located in the back end of the DAQ system of the components and is the same for all DAQ systems. A unique interface is provided by the eventbuilder, and the data exchange is done by a triple ported memory (TPM) which can be accessed by both sides. In the case of a transputer based component the other transputer on the 2TP board belongs to the component which then writes the data into the TPM. If the DAQ system of the component is not based on transputer the access to the TPM is done via the VME-bus. In the EVB each of these interfaces is connected to the supervisor and the crossbar switch (CBS) (see figure 11). The EVB front end sends the data packages to the crossbar switch which then sends the data to the TLT. The status of the front end and information about the currently received component data, is sent to the supervisor. The front end receives from the supervisor the commands to send specified data packages over the CBS to the eventbuilder back end.

Supervisor The supervisor controls the whole eventbuilder system and is also the interface to the central data acquisition system and the GSLT. For the interface between the supervisor and the components, a transputer network with a tree-like structure is used. It provides the supervisor with the capability to communicate with up to 26 components. The high processing power of the tree is used to keep the number of messages to the scheduler down to an absolute minimum. Depending on the arriving data sets in the eventbuilder front end, the load on the data lines, and the TLT processors, the scheduler calculates an optimal switching strategy for the data transfer from the components to the TLT processor nodes.
To provide a short switching time for a heavyly loaded system, software with a pipelined message structure has been developed [HAG90]. If a higher data troughput is required, the scheduler can be sped up by the distribution of the decision pipeline over several transputers. In addition, the supervisor has to make performance measurements and to change the scheduling strategy in case of hardware errors e.g. a power failure in the interfaces.

Crossbar Switch (CBS) The crossbar switch is the essential element of the eventbuilder system. It can connect each of the links of the front end with each of the links of the back end.
Figure 11 shows that $17 \times 3 = 51$ links are used at the front end of the crossbar switch. Each of the 17 transputers of the eventbuilder front end needs one of its four links for the connection with the supervisor. The other transputer which is shown on the 2TP board belongs to the component. At the back end of the eventbuilder there are 6 connections to the TLT. Each of them has 2 transputers with four available links which results in $6 \times 8 = 48$ links that have to be served at the back end.
Unfortunately the standard crossbar switch for transputers[1] allows only the connection between 32 input and 32 output links. Therefore the eventbuilder uses 4 of these commercial crossbar switches and several OR gates for each direction plus one transputer for the control a fast bidirectional crossbar [HAG90]. With the software running on the transputer the system appears to the outside like one big crossbar switch. The concept allows the construction of crossbars in steps of 32 links (32×32, 64×64 etc.). A 64×64 crossbar which has been built offers the possibility to use more links in the future.

Back End The eventbuilder back end feeds complete detector events into the TLT. Before this is done the events are formated into the format for the offline programs (ZEBRA). The hardware consists of the same standard two transputer VME module (2TP) which is also used for the eventbuilder front end.

3.4.3 Performance

The requirements for the eventbuilder have been to assemble events with a size of 140 kbyte at a rate of 100 Hz which corresponds to a bandwidth of 14 Mbyte/s. Measurements show that the current eventbuilder is able to handle at least twice the bandwidth with a trigger rate between 150 and 200 Hz. The number of components can be increased without any hardware changes from 17 to 26. Due to the central position of the eventbuilder in the ZEUS online system it is quite important to provide adequate reserves in data handling power.

3.5 Third Level Trigger (TLT)

The TLT is a microprocessor farm which works on complete detector events with offline algorithms. Figure 14 shows an overview of the complete TLT system.

---

[1] C004 from INMOS

Hardware Architecture Data input is from the eventbuilder (see top of figure 14); they are distributed by the eventbuilder into 6 crates via two transputer modules (*2TP*) [BOT87]. These are the 6 back ends from the eventbuilder which have already been mentioned in the previous section. Each 2TP module transports the data from the eventbuilder to the Branchbus to VME Interface (*BVI*) via a VME-bus. The Branch Bus is a parallel bus system which has been developed at FERMILAB [NAS89]. Each of the six *BVIs* is connected via a Branch Bus and six VME Branch Bus Controller (*VBBC*) to six workstations from Silicon Graphics Incorporated (type *SGI 4D/35*). These are computers with RISC[2]-CPUs which have a high performance and use the operating system UNIX. Altogether there are 36 workstations in the TLT which provide a total computing power of 1050 Mips[3]. All these six Branch Bus lines are connected to a common Branch Bus Switch which is a crossbar for the Branch Bus. Via the Branch Bus Switch the data can be shipped via interfaces (*BVI, CES HVR 8217, DRB 32*) to a *VAX 8700* or controlled by a VME CPU (*MVME 147S*) to buffering disks. The buffering disks are connected to the VME bus with a Small Computer System Interface (*SCSI*). A VME High Speed Link (*VMEHL*) offers the possibility to ship the data to the IBM mainframe via an optical link. This system where the Branch Bus Switch connects the six branches, the central DAQ system of ZEUS and the interface to the computer center with each other provides a maximum of flexibility. An *Ethernet LAN* is used for the control of the system and it connects all the processors of the TLT with each other.

Algorithms Most of the TLT input rate of ≈ 100 Hz consists of beam gas and soft photoproduction events. After the selection of inelastic scattering and some other interesting events like heavy quark production and large p_T photoproduction a rate of ~ 3 Hz will be sent to the computer center and written on cartridges.
Obviously, no simple trigger conditions can be applied for this task. To reach the required high reduction rate on this level an event reconstruction has to be used. With the complete event reconstruction including particle identification and the calculation of kinematic parameters (Q^2, x and y), the TLT offers the power of offline data analysis with the timing and bandwidth capabilities of an online system.

---

[2] Reduced Instruction Set Computer

[3] Mega Instructions Per Second

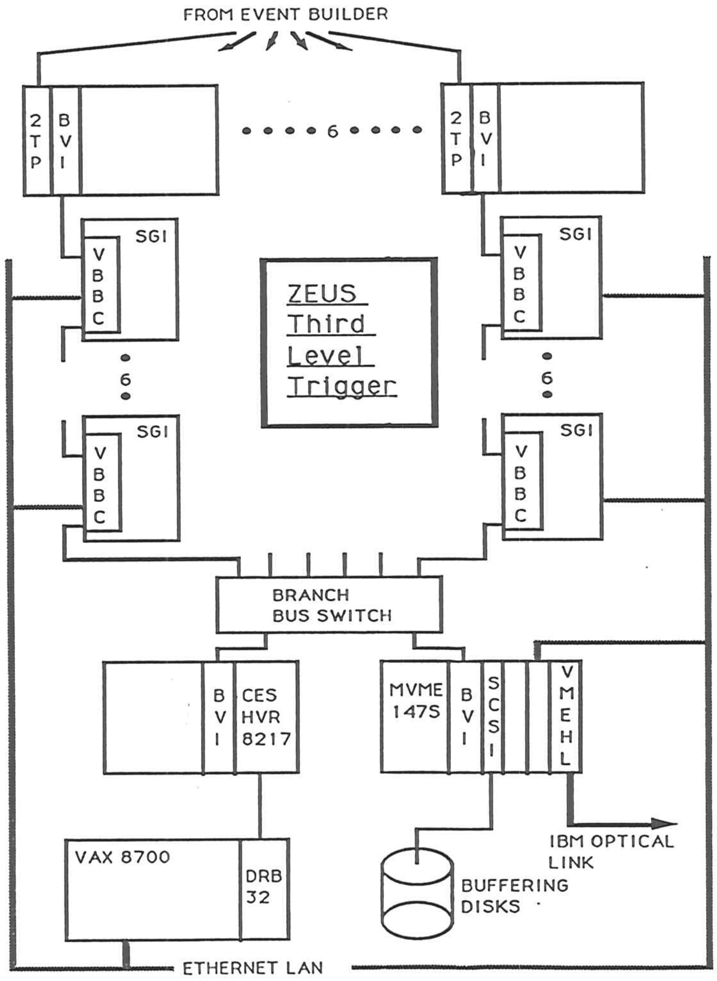

Figure 14: Third Level Trigger System (explanation see text)

4 Calorimetry

A calorimeter absorbs the energy of an incoming particle and delivers a signal which is proportional to the absorbed energy.
Calorimeters have the advantage that the relative energy resolution $\Delta E/E$ scales with $1/\sqrt{E}$ if the calorimeter is well built and the absence of systematical effects. For a precise measurement of individual events, the calorimeter has to have a sufficient size to stop all the particles. The average length required to stop a particle of a given energy is proportional to lnE. Optical readout can be faster than 100 ns and allows to cope with high particle rates. A segmentation of the calorimeter provides a position measurement. Segmentations longitudinal and transverse to the direction of the incoming particle allow a particle identification by the shower dimensions.
There are two types of calorimeters. If the absorber and the detector part of a calorimeter is built out of the same material it is called homogeneous. Examples are transparent materials like NaI, BGO ($Bi_4Ge_3O_{12}$), or lead glass. These calorimeters have a very high resolution for electromagnetic showers. But, it is difficult to produce crystals of the needed size and the materials are delicate to handle. With the increasing energy of current accelerators, homogeneous calorimetry for hadrons is becoming less viable. The problem can be solved with the use of two kinds of materials: a heavy material with a high Z (e.g. uranium or lead) as the absorber and another for readout of the signal from the deposited energy (liquid argon, plastic scintillator etc.). This is called a sampling calorimeter. In a sampling calorimeter the energy is deposited in the absorber and the detector material, but only the energy deposited in the detector material can be measured. The fraction of energy deposited in the active detector material is the sampling fraction:

$$R_j = \frac{E_{vis,j}}{E_{invis,j} + E_{vis,j}} = \frac{E_{vis,j}}{E_{abs,j}},$$

where

j	is the index for the particle type (e.g. e, μ, p),
$E_{vis,j}$	is the energy deposited in the active detector material,
$E_{invis,j}$	is the energy deposited in the passive absorber material,
$E_{abs,j}$	is the total absorbed energy in the calorimeter.

The sampling fractions (R_j) are different for each particle type. Usually, the values of the sampling fractions are normalized to the response of a minimal ionizing particle (mip).

Energy Loss of Charged Particles in Matter The mean energy loss of charged particles due to ionization is described by the Bethe-Bloch formula [ROS52]:

$$\frac{dE}{dx} = \alpha^2 2\pi N \lambda_e^2 \frac{Z m_e}{A\beta^2}\left(ln\frac{2m_e\beta^2\gamma^2 E'_m}{I^2(Z)} - 2\beta^2 + \frac{1}{4}\frac{E'^2_m}{E^2} - \delta\right), \tag{3}$$

where

α	(1/137.036) is the fine structure constant,

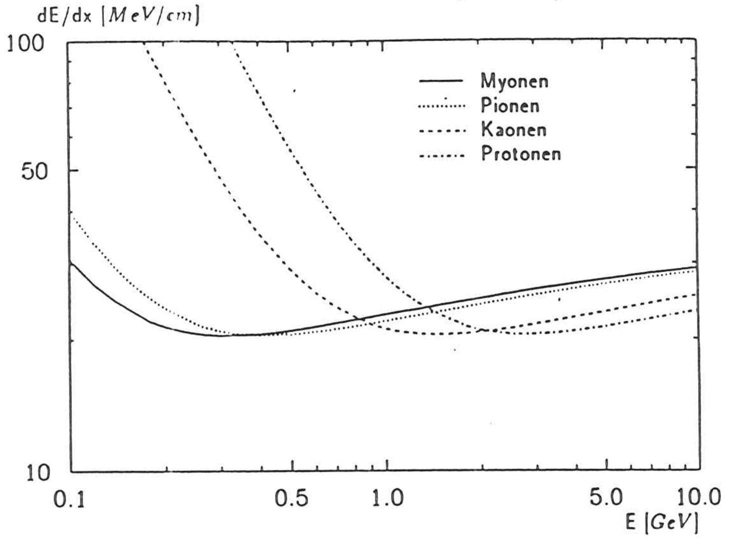

Figure 15: Energy loss due to ionization given by the Bethe Bloch formula in uranium [LOH85]

N	6.023 10^{23} is Avogadro's number,
Z, A	are the atomic number and the atomic weight of the traversed medium,
m_e, m_m	are the rest masses of the electron and the particle,
$\beta = p/E$	where p is the momentum and E the energy of the particle
$\gamma = E/m_m$,	
$\lambda_e = \hbar/m_e c$	(3.8616 $10^{-11} cm$) is the Compton wavelength of the electron,
$I(Z)$	is the mean ionization potential of the medium,
E'_m	is the maximum energy transferable to the electron and
δ	is the density correction.

The maximum energy which is transferable to an atomic electron (E'_m) is given by:

$$E'_m = \frac{2m_e p^2}{m_e^2 + m_m^2 + 2m_e\sqrt{p^2 + m_m^2}}. \tag{4}$$

The density correction ($\delta = \delta(X)$) mentioned above is a function of a parameter $X = \log\frac{p}{m_e c}$ and some material specific constants (see also [STE84]).
Figure 15 shows the Bethe-Bloch function. The minimum of this function is used to define a minimum ionizing particle (mip). Muons with 10 GeV lose most of their energy (H: 99.8%

, Fe: 98%, U: 95%) due to ionization. This means that muons in the GeV energy range traversing thin layers of material are particles which have an energy deposition similar to mips. At higher energies muons do not lose their energy by ionization alone but also due to other effects like bremsstrahlung and pair production. Therefore they deposit more energy than a mip.

The response of a mip is often used to normalize signals of real particles. The use of the energy deposition of a mip has the advantage that when normalizing to mips many dependencies (e.g. plate thickness) cancel in first approximation. Also it can be computed easily given the properties of the material. Thus, the mip normalized sampling fraction of electrons (e) is defined as:

$$\frac{e}{mip} = \frac{R_e}{R_{mip}}.$$

4.1 Electromagnetic Showers

The average energy loss of a high energy electron to Bremsstrahlung is

$$< \frac{dE}{dx} >= -\frac{E}{X_0},$$

where

x is the thickness of material,

E is the energy of the electron and

X_0 is the radiation length given by [PER82]

$$\frac{1}{X_0} = \frac{4Z(Z+1)r_e^2 N_0}{137A} \ln\left(\frac{183}{\sqrt[3]{Z}}\right),$$

where

Z is the atomic number,

r_e is the classical electron radius,

N_0 is Avogadro's constant and

A is the atomic mass number.

Use of X_0 allows a description which is in some approximation material and geometry independent. The values of X_0 for some materials are given in table 3. As a rough estimate [AMA81]

$$X_0 \left[\frac{g}{cm^2}\right] \approx 180 \frac{A}{Z^2}$$

can be used. An electromagnetic shower is caused by the interaction of electrons, positrons and photons with the calorimeter material. Figure 16 shows the main processes which cause electrons to lose energy in lead. At lower energies, most of the energy loss is due to ionization and at higher energies most of the energy is lost by bremsstrahlung. The energy at which the loss due to bremsstrahlung is equal to the loss due to ionization is called the critical energy (E_c). An estimate of the critical energy, with an error of 10% for values of Z between 13 and 92, is given by

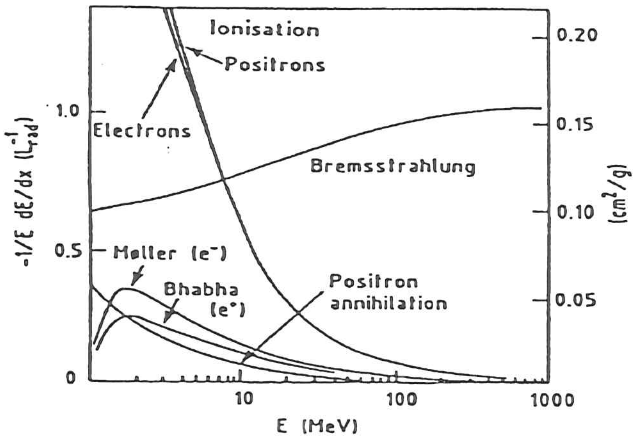

Figure 16: Energy loss of electrons in lead (from [FAB87]). The unit L_{rad} corresponds to the radiation length X_0 defined in the text.

$$E_c \approx \frac{550MeV}{Z}.$$

The absorption of photons (see figure 17) is due to 3 processes, photoeffect, Compton scattering and pair production. At energies above 10 MeV, pair production, with a cross section essentially independent of energy, is the dominant process.

An electromagnetic shower can be started by a high energetic electron or photon which enters a volume of matter. At high energies the processes driving the shower are bremsstrahlung and pair production. Therefore the shower size scales with X_0. Figure 18 shows the longitudinal development of electromagnetic showers induced by 10 GeV electrons in units of X_0. The difference in the shower development is due to the different critical energies (E_c) of the materials. The transverse size of the electromagnetic shower scales with the Molière radius (R_M). It is given by ([AMA81]):

$$R_M = 21[MeV]\frac{X_0}{E_c} \approx 7\frac{A}{Z}\left[\frac{g}{cm^2}\right]$$

This equation allows an estimate of the transverse size of an electromagnetic shower.

A rough estimate of calorimeter length in which 98% of the energy is contained is given by ([BER87B] and [FAB87])

$$< L_{98\%} > \simeq \underbrace{\frac{\ln\frac{E}{E_c}}{\ln 2}X_0}_{\text{maximum of the shower}} + \underbrace{4 \times (3.4 \pm 0.5)X_0}_{\text{exponential tail}}.$$

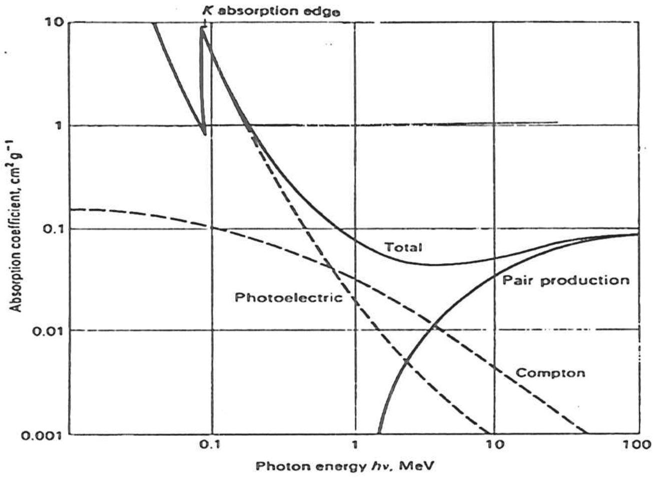

Figure 17: The absorption coefficient of lead in cm^2/g for γ-rays, as a function of energy (from [PER82])

Material	Z	ρ $[g/cm^3]$	X_0 $[g/cm^2]$	X_0 $[cm]$	λ_{int} $[g/cm^2]$	λ_{int} $[cm]$	R_M $[cm]$	λ_{int}/X_0
Polystyrene	(3.4)	1.060	43.8	41.3	82.0	77.4	14.7	1.87
NaI	(32)	3.667	9.5	2.59	152.0	41.5	3	16.0
BGO	(27.6)	7.100	8.5	1.20	164.0	23.1	1.2	19.3
Al	13	2.699	24.01	8.89	106.4	39.4	5.38	4.43
Fe	26	7.874	13.84	1.76	131.9	16.8	1.91	9.53
Pb	82	11.350	6.37	0.56	194.0	17.1	1.56	30.45
U	92	18.950	6.00	0.32	199.0	10.5	0.96	33.17

Table 3: Values of the radiation length (X_0) and nuclear interaction length (λ_{int}) for some materials used in calorimeters.

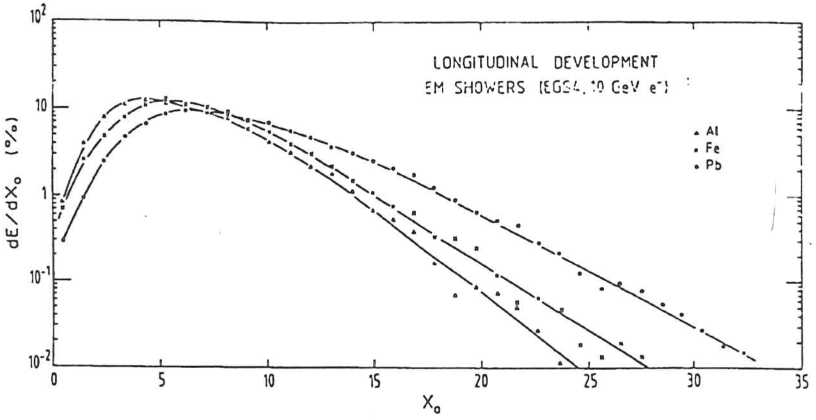

Figure 18: The longitudinal development of an electromagnetic shower started by 10 GeV electrons (from [Wig86])

E [GeV]	Length of $< L_{98\%} >$ in cm SCSN-38	Pb	U
10	800	13	8
100	950	15	9
$R_{95\%}$	30	3	2

Table 4: Approximate size of an electromagnetic shower in some materials

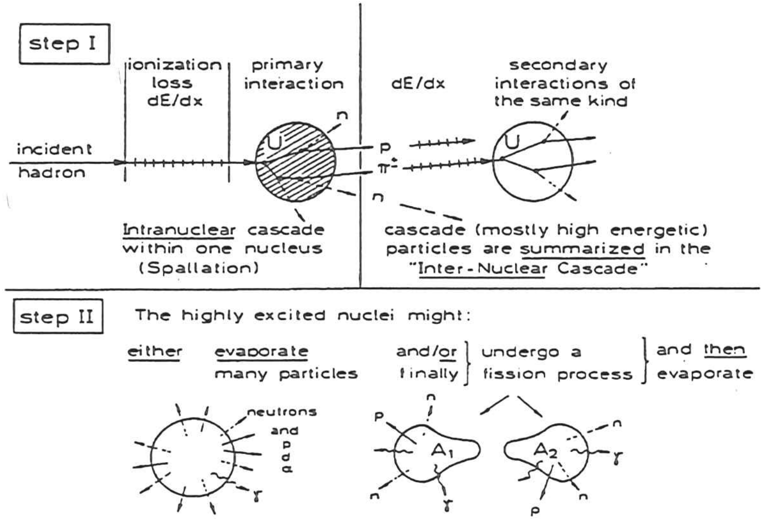

Figure 19: Development of the inter- and intranuclear cascade in a hadronic shower [BRU87])

The radius of the cylinder which contains 95% of the shower energy is given by

$$R_{95\%} \simeq 2R_M.$$

Table 4 lists some values for $R_{95\%}$ and $< L_{98\%} >$.

4.2 Hadronic Showers

Hadronic showers are more complicated than electromagnetic showers. The main reason is the large number of different reaction channels for hadrons. Figure 19 [BRU87] illustrates this point. An incoming hadron suffers energy loss by ionization if charged. If it hits a nucleus of the absorber material, the interaction leads to an intranuclear cascade which results in the production of various particles ($\pi^{\pm}$, π^0, n, p, α etc.). The particles from this primary interaction hit further nucleons and start the development of an internuclear cascade. In a second step, the excited nucleus evaporates further particles and may undergo fission or fragmentation. A quantity used to describe the longitudinal and transverse dimensions of the hadronic shower is the nuclear interaction length,

$$\lambda_{int} \approx 35 \frac{A^{\frac{1}{3}}}{\rho} [cm].$$

ρ = specific density $\left[\frac{g}{cm^3}\right]$

E [GeV]	Length of $< L_{95\%} >$ in cm		
	SCSN-38	Pb	U
1	250	55	34
10	350	77	48
100	480	105	65
$R_{95\%}$	77	17	11

Table 5: Approximate size of a hadronic shower in some materials

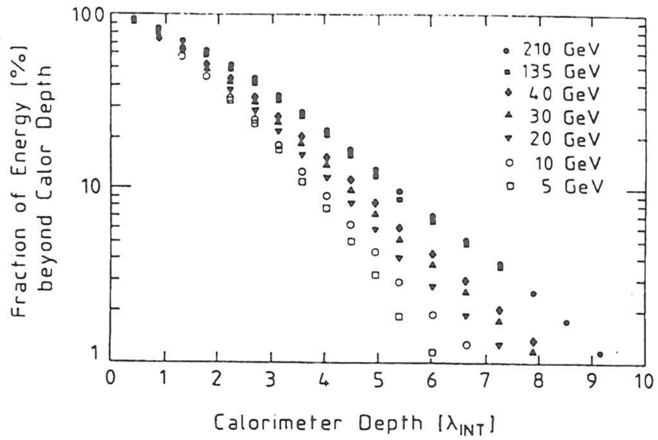

Figure 20: Energy deposition of a hadronic shower in a uranium scintillator calorimeter [Cat87]

Table 3 gives some values of λ_{int}, which is defined as the average distance which is traversed in the medium by the particle before it is absorbed. Figure 20 shows the fraction of the escaping energy beyond a specific calorimeter depth for various primary energies. For a realistic shower size, empirical formulas, derived by experiments and Monte Carlo simulations, have to be used. As shown in [FAB87], the depth which contains 95% of the shower energy is given by:

$$< L_{95\%} > \simeq 2.5E^{0.13} + 0.2\ln(E) + 0.7 \quad \text{(with E in GeV)}$$

in units of λ_{int}. The cylinder which contains 95% of the energy is given by:

$$R_{95\%} \simeq \lambda_{int}$$

The accuracy of these equations is around 10%. Table 5 list some values of $< L_{95\%} >$ and $R_{95\%}$.

4.3 Energy Resolution of Sampling Calorimeters

4.3.1 Energy Resolution for Electromagnetic Showers

It is limited by the following effects:

1. Sampling fluctuations, contribute a term $\sigma_{sampl}/\sqrt{E}$, which comes from the fact, that the shower development is only measured in the scintillator plates.
2. Statistical fluctuations in the readout process, mainly connected with fluctuations in the number of photoelectrons in the PMT, contributing a term $\sigma_{pe}/\sqrt{E}$.
3. Systematic effects, caused by mechanical tolerances, inhomogenities, calibration errors, noise etc. of the calorimeter, contribute a term σ_{calib}.

The total energy resolution is given by adding these in quadrature:

$$\frac{\sigma}{E} = \frac{\sigma_{sampl}}{\sqrt{E}} \oplus \frac{\sigma_{pe}}{\sqrt{E}} \oplus \sigma_{calib}$$

where $\oplus$ denotes the quadratic sum. The systematic effects do not scale with $1/\sqrt{E}$. Therefore σ_{calib} becomes the dominating term for higher energies.
For a test calorimeter with 3.2 mm depleted uranium and 3.0 mm scintillator [TIE89] the following values have been measured:

σ_{sampl}	The sampling fluctuations have been determined to $\sigma_{sampl} = (16.5 \pm 0.5)\%$.
σ_{pe}	The statistical fluctuations due to photostatistics have been determined to 6.5%.
σ_{calib}	The calibration error does not scale with energy. Therefore it has to be kept as low as possible or it will be the limiting part of the energy resolution for higher energies. A huge variety of calibration procedures have been developed which will be presented in section 6. The aim is to keep the calibration error down to 1%.

4.3.2 Energy Resolution for Hadronic Showers

In addition to the effects which limit the energy resolution of electromagnetic calorimeters there is a further effect for hadronic calorimeters called intrinsic fluctuations. These intrinsic fluctuations are mainly due to two effects.

1. Only a part of the energy from the hadrons is visible in the calorimeter. The other part of the energy cannot be measured. A part of the energy which cannnot be measured is used for the production of neutrinos. A further part of the shower consists of high energetic muons which leave the detector and therefore deposit only a part of their energy in the calorimeter. The energy used for the production of low energetic γ-particles and for breaking up the nuclear bindings cannot be measured due to their small range in the absorber material.
2. A hadronic shower has an electromagnetic component. Therefore a part of the energy of the hadronic shower is deposited by pure electromagnetic interaction. The statistical fluctuations between the electromagnetic and the hadronic component of the shower also load to intrinsic fluctuations.

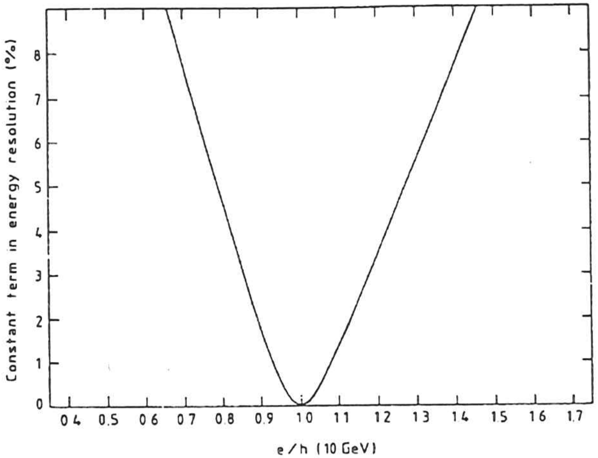

Figure 21: Dependence of the constant term $c(e/h)$ of equation 5 on the e/h ratio [Wig87a]

A parametrisation has been proposed in [Wig87a] for the intrinsic fluctuations:

$$\sigma_{intr} = \frac{b}{\sqrt{E}} + c(e/h) \text{ (see figure 21)} \qquad (5)$$

with $c = 0$ for compensating calorimeters ($e/h = 1$). A compensating calorimeter delivers the same signal for a hadronic or an electromagnetic shower of the same energy. The ratio of these signals e/h can be written as

$$\frac{e}{h} = \frac{e/mip}{E_{em}\frac{e}{mip} + E_{\pi}\frac{\pi}{mip} + E_{p}\frac{p}{mip} + E_{n}\frac{n}{mip} + E_{Nuc}\frac{Nuc}{mip}},$$

with the definitions from above. A method to tune the e/h ratio is to adjust the ratio of the thickness of the active material and the absorber. This can be understood in the following way:
The number and energy distribution of the neutrons depends mainly on the absorber material. Because neutrons lose their energy predominantly by elastic scattering processes with the protons of the hydrogen in the scintillator, the neutron signal is, approximately independent of the thickness of the scintillator plates. But since the signal from charged ionizing particles depends directly on the thickness of the scintillator plates a decrease of the scintillator thickness at a constant thickness of the uranium plates will approximately decrease the mip signal and keep the n-signal constant. In this way the e/h ratio can be adjusted.
Thus the total energy resolution is given by

$$\frac{\sigma}{E} = \frac{\sigma_{intr}}{\sqrt{E}} \oplus \frac{\sigma_{sampl}}{\sqrt{E}} \oplus \frac{\sigma_{pe}}{\sqrt{E}} \oplus \sigma_{calib}.$$

For a compensating uranium scintillator test calorimeter [TIE89] the following contributions to the hadronic energy resolution have been determined:

σ_{intr} The intrinsic fluctuations of the hadronic shower in the ZEUS uranium scintillator calorimeter have been measured to $(20.4 \pm 2.4)\%/\sqrt{E}$.

σ_{sampl} The sampling fluctuations have been measured to be $(31.1 \pm 0.9)\%/\sqrt{E}$ and, thus, limit the energy resolution. The reason why the sampling fluctuations of hadronic showers are nearly twice as big as the sampling fluctuations for electromagnetic showers is not understood.

$\sigma_{pe}, \sigma_{calib}$ These contributions to the energy resolution are the same as for electromagnetic showers.

5 The ZEUS Calorimeter

5.1 Principle

The layout of the entire calorimeter can be seen in figure 22 which shows a cut along the beampipe through the calorimeter and the central tracking system. It can be seen that the central tracking system and therefore the interaction point is nearly completely enclosed by the calorimeter. The calorimeter covers 99.8% of the forward hemisphere and 99.5% of the backward hemisphere. Mechanically, it is divided into 3 separate calorimeters:

- the forward calorimeter (FCAL) which covers the polar angle range from $\theta = 2.2^0$ to 39.9^0,
- the barrel calorimeter (BCAL) which covers the polar angle range from $\theta = 36.7^0$ to 129.2^0,
- the rear calorimeter (RCAL) which covers the polar angle range from $\theta = 128.1^0$ to 176.5^0.

It consists of alternating plates of depleted uranium, as absorber material, and plastic scintillator plates for readout. One of the advantages of such a uranium scintillator sandwich calorimeter is a permanent signal due to the radioactivity of the uranium. This Uranium NOise (UNO) signal can be used for calibration purposes. A further advantage of the ZEUS calorimeter is that it is compensating. As explained before in section 4.3.2, an equal energy response for hadrons and electrons (e/h = 1) has been achieved by properly choosing the ratio between the uranium and the scintillator thicknesses.

5.2 Layout of the ZEUS Calorimeter

5.2.1 Overview

Each calorimeter consists of independent mechanical modules. Stacking, testing , calibration and installation has been done module per module. The FCAL/RCAL modules have a width of 20 cm and heights between 2.2 and 4.6 m. Both FCAL and RCAL consist of 24 modules, including 2 special modules positioned above and below the beampipe. The BCAL consists of 32 identical modules, each covering an 11.25^0 wedge in azimuth angle. The inside radius of the sensitive volume of each BCAL module is 122 cm and the outer radius 229 cm with the corresponding widths of 24 cm and 45 cm.

For FCAL and RCAL each module is segmented in towers of 20 cm × 20 cm. Each tower consist of an electromagnetic section (EMC), the first hadronic section (HAC1), and for the FCAL in addition the second hadronic section (HAC2). Depending on the position in the calorimeter there can be one (called HAC0), two (EMC1 and EMC2) or four (EMC1,...,EMC4) electromagnetic sections. The readout of the scintillator of each section uses wavelength shifter and two photomultiplier per section. The EMC has a depth of 25 radiation lengths X_0, which is equivalent to one interaction length λ for hadronic interactions. Figures 23 and 24 show the front view of the FCAL and the RCAL. Due to the higher energies in the forward region, the FCAL has two hadronic sections (HAC1 and HAC2) with a total depth of 6 λ. The RCAL has only one hadronic section with a depth of 3 λ. The finer segmentation of the EMC parts,

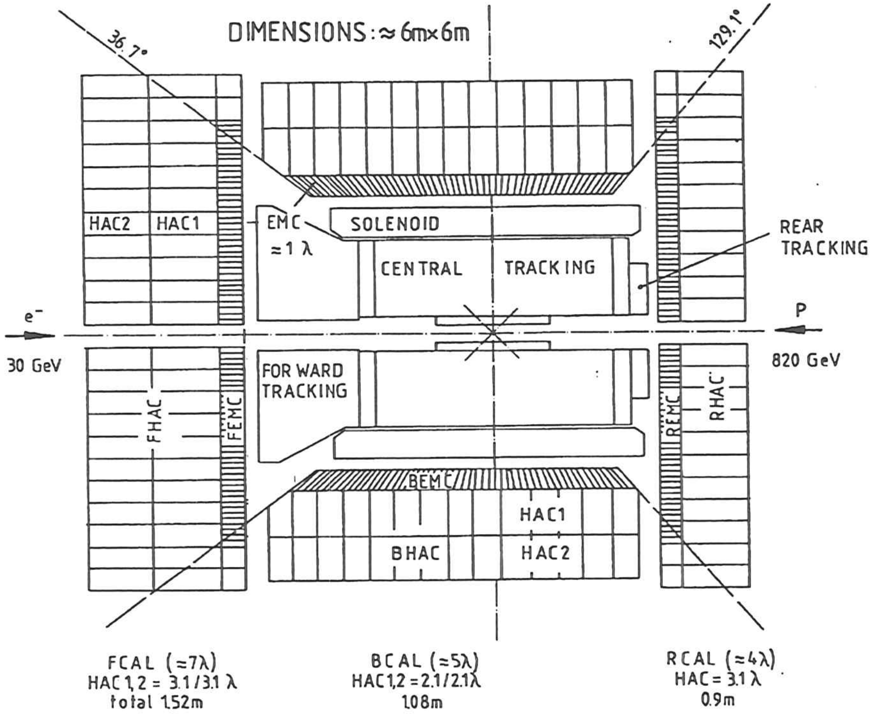

Figure 22: Solid angle coverage of the ZEUS calorimeter

four instead of one hadronic readout section in the FCAL and two instead of one hadronic readout section in the RCAL, can be seen clearly. The outer towers in the front sections do not have a finer segmentation because they are shadowed by the BCAL (see figure 22). These sections are named HAC0s instead of EMCs.

All towers from FCAL and RCAL are non projective when seen from the interaction point. The EMC sections of the BCAL are projective in both azimutal and polar angle while the HAC sections are projective in azimuthal angle only.

5.2.2 Description of a (FCAL-)Module

Figure 25 shows the isometric view of a full size FCAL module. The front side of the module which points to the interaction point is on top of the picture. In the ZEUS detector, the module is standing on the lower C-leg. From right to left the module is divided into 23 towers. Figure 25 also shows how the WLS of the EMC are arranged to transport the light from the electromagnetic section to the photomultiplier (see tower 14). After the finely segmented FEMC section, follow the FHAC1 and the FHAC2 sections. The arrangement of the WLS in these sections is shown in towers 15 and 16 of figure 25.

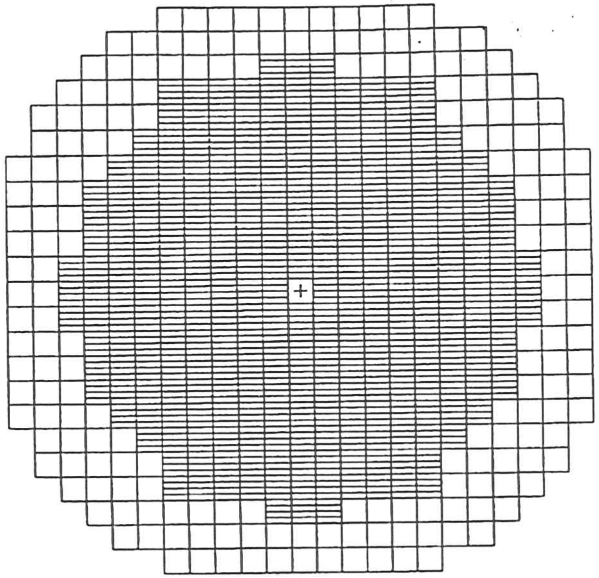

Figure 23: Front view of the FCAL

The mechanical back bone of the module is the C-frame (see fig. 26). The scintillator and depleted uranium plates are stacked on top of each other onto the C-frame. A stacking robot has been used to keep the radiation exposure for humans as low as possible. An important criterion during the module assembly was the uniformity of the height of the module to avoid mechanical stresses. To minimize the height deviations from the nominal value of the modules every 25 DU and SCI layers the stack was compressed and the height measured. The needed corrections for the next 25 plates were applied through the use of different spacer thicknesses. The spacers are small pieces ($5 \times 10\ mm^2$) of strong carbides (titanium carbide in the EMC and tungsten carbide in the HAC sections). They are placed at the corners of a tower in the cut-outs of the scintillator tiles, to avoid pressure onto the tiles. Spacers with thicknesses between 3.8 or 4.0 mm were used. Due to this correction the height of the sections throughout the module deviates by less than 1 mm from the nominal value.

The mechanical stability of the module is provided by the C-frame which surrounds the whole module on three sides. The uranium plates are clamped together and pulled towards the end beam by stainless steel straps 196 mm wide and 0.25 mm thick. With these straps the stacks are compressed with a force of 15 - 20 kN per tower leading to a compression of about 3 mm. The friction force between the spacers and the DU plates prevents the plates from moving. To balance the force between the two sides and to allow an easy slide of the steel

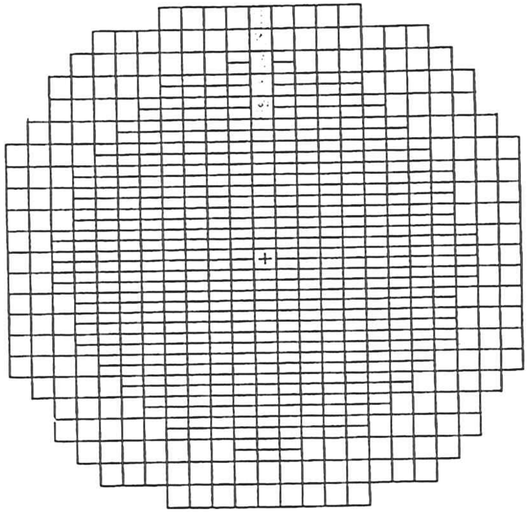

Figure 24: Front view of the RCAL

strap over the top, a top plate of 15 mm thick aluminum with round edges has been installed. The required tension force of the stainless steel straps and the overall mechanical stability has been extensively studied by finite element calculations [STR91]. The modules have been designed to stand a vertical acceleration of 4 g and a horizontal acceleration of up to 1 g during transport with the orientation shown in figure 25 when the module is standing on the end beam.

Overview About a Calorimeter Tower Figure 27 explains the optical readout scheme for one tower. An incoming particle produces a shower which is partially absorbed by the uranium plates. Particles traversing the scintillator produce a light pulse with a wavelength between 400 and 500 nm. The light is transported in the scintillator to the wavelength shifter (WLS). Here it is converted to a wavelengths between 500 and 550 nm. To improve the light yield and uniformity each wavelength shifter is surrounded by a back-and an end-reflector. From the wavelength shifter, the light is transported to the photomultiplier which transforms the light into an electrical pulse.

Absorber Plates: They consist of depleted uranium and contain 98.4 % U238, 0.2 % U235 and 1.4 % Nb. Nb improves the corrosion properties of the alloy. The uranium decay products have been extracted from the uranium. The bare DU-plates were rolled from billets by MSC in Oak Ridge (USA).
The DU plates have a thickness of 3.3 mm, wrapped with 0.2 mm of stainless steel for the electromagnetic part and 0.4 mm stainless steel for the hadronic sections, and the scintillator

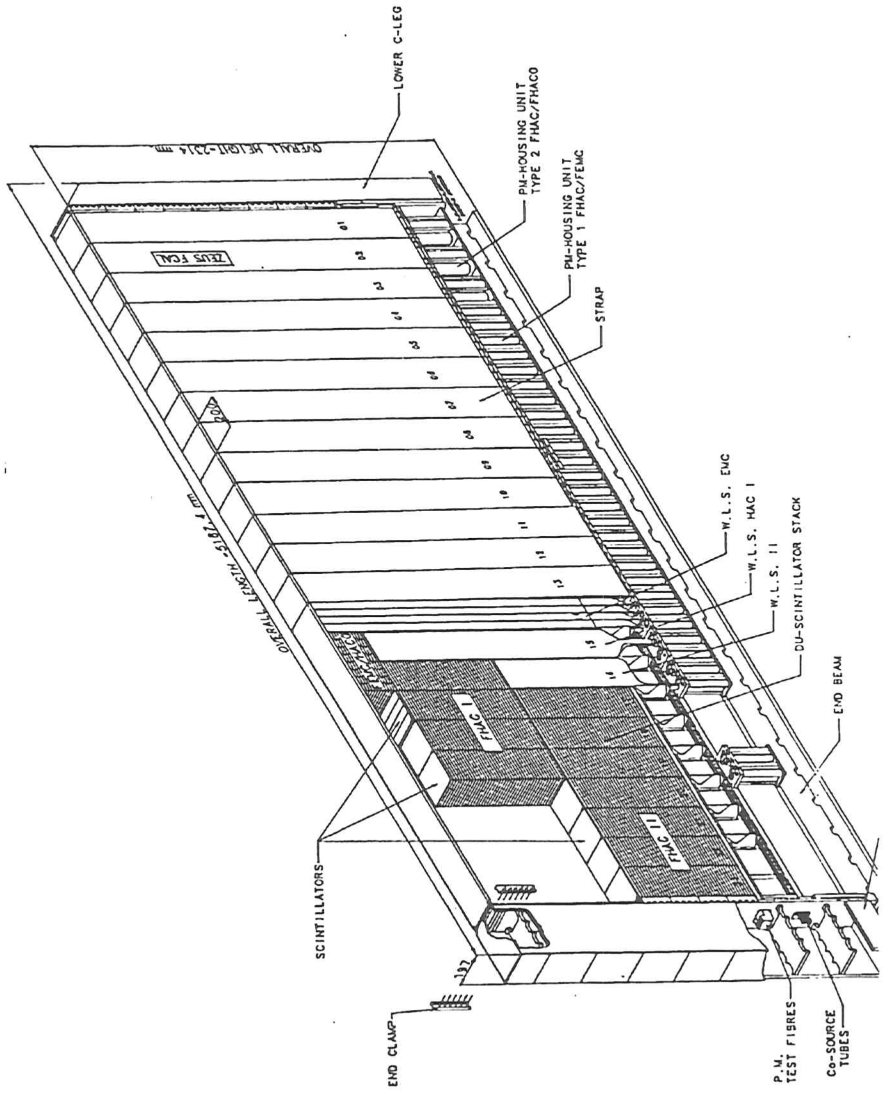

Figure 25: An isometric view of the largest FCAL module type

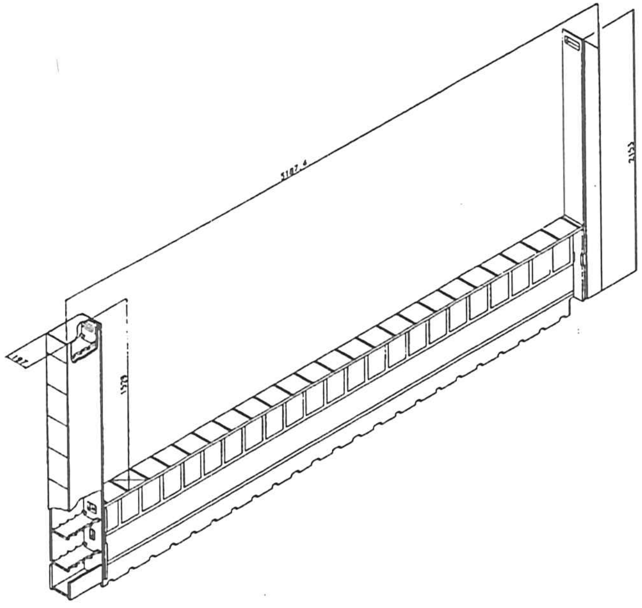

Figure 26: C-frame

plates have a thickness of 2.6 mm.

Scintillator SCSN-38[4] has been used for the scintillator plates. This is an aromatic cast scintillator with a cross linked polystyrene base which is doped with two wavelength shifter dies. An aromatic cast scintillator has been chosen because of its high light yield and its stability against aging and radiation. Furthermore, this material has a high light yield. It has been extensively tested and has been used also for the calorimeter prototype [BEH89]. The scintillator plates were cast to a thickness of 2.6 ± 0.2 mm. For an improvement of the light yield, the tiles have been wrapped into Tyvek paper. Tyvek paper is produced by compressing spun polyethylene and has the same UV reflectivity as aluminum foil. Electron scans with a Ru-source showed an variation in light yield over the scintillator of ±7%. It has been improved to the required ±2% with a black pattern (fig. 28) which has been printed onto the Tyvek paper.

Wavelength Shifter The material used is Y7 dissolved in PMMA (plexiglas), produced by Kuraray Co.Ltd. Tokyo (Japan). Its absorption spectrum matches the emission spectrum of the scintillator (SCSN-38) and produces an appropriate spectrum for the PMT photocathodes. Further advantages are the long attenuation length, hardness against aging and

---

[4] produced by KYOWA Gas Japan

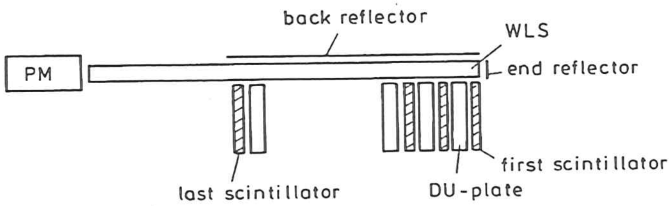

Figure 27: Schematic overview of the readout with WLS [AND91]

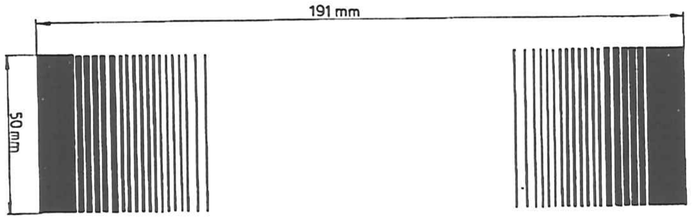

Figure 28: Correction pattern for the scintillator [AND91]

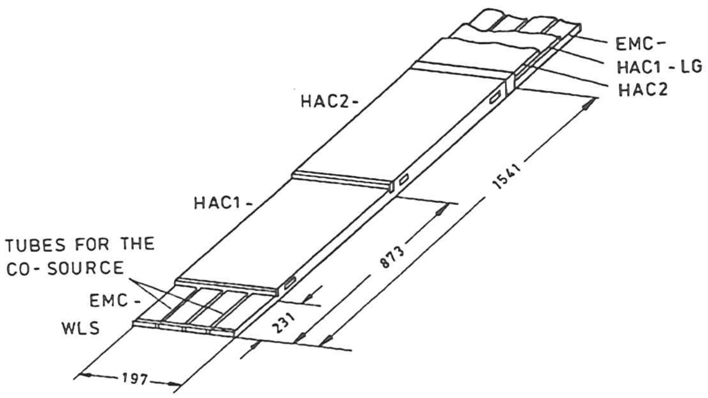

Figure 29: Cassette for the readout with WLS

radiation [AND91], as well as easy machining properties. WLS and Light Guide (LG) are produced from one piece to avoid light losses due to glue joints. Direct contact between the scintillator and the WLS is avoided by 0.3 mm thick transparent lines. For an improvement of the longitudinal uniformity, a pattern is printed onto the back reflector of the WLS. It improves the longitudinal non-uniformity from 12 % to 3%. An end reflector (fig. 27) also improves the absolute light yield and uniformity of each WLS-bar. The WLS for EMC, HAC1 and HAC2 which correspond to one side of a tower are mounted in stainless steel cassettes. Figure 29 shows a WLS steel cassette for an FCAL module. Brass tubes are placed between the 4 WLS strips. A ^{60}Co source connected to a steel wire can be pushed through these tubes. The radioactivity of the ^{60}Co induces a signal in the scintillator plates which can be used to measure the light yield of each scintillator and the uniformity of the wave-length shifter response.
The readout of the light from the two opposite sides of the scintillator plates offers several advantages. Firstly the sum of right and left signal gives a very uniform response. Secondly, the position of the particle perpendicular to the beam can be measured from the difference in pulse height. Finally the signals between the two PMTs can be compared for test purposes and provide redundancy.

Photomultiplier Tubes (PMT): Several criteria have to be satisfied by the PMTs. The tubes had to have a high quantum efficiency and a small dark current. Tubes were rejected which did not have the required high stability and linearity in response. The required linearity of response is to be within ±2% up to anode charges of 2000 pC. The selected tubes have a stability of response which is better than 1% up to 1s and better than 3% for up to 4 hours. After extensive tests, the XP1911 tube from Philips has been selected for the EMC section of the FCAL and the tube R580 from Hamamatsu Photonics for all other sections. Both are 10-stage head-on tubes with diameters of 19 (38) mm and bi-alkali photocathodes. The quantum efficiency of the tubes is at least 12% at a wavelength of 520 nm with a dark current

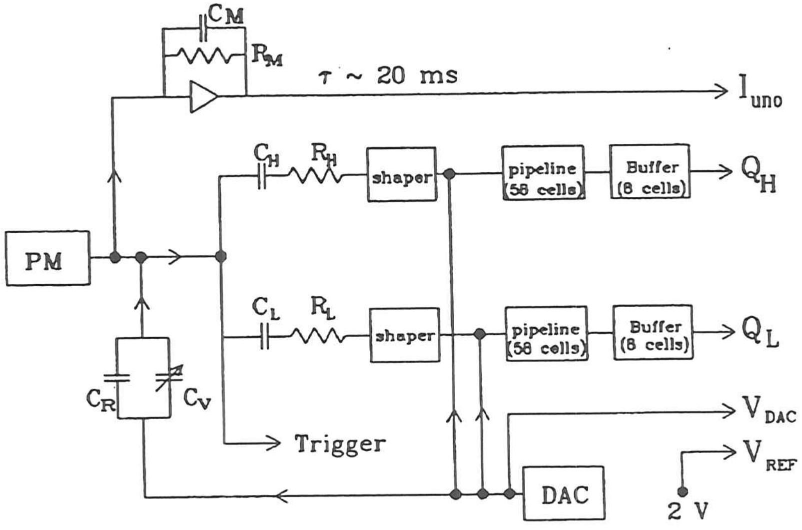

Figure 30: Schematic view of the Analogue card

which is smaller than 1 nA (3 nA) for the tube XP1911 (R580) at a gain of $5 \cdot 10^6$. The high voltage of the PMTs is produced by small Cockcroft Walton generators at the base of each individual tube. The Cockcroft Walton generators have three main advantages compared to the conventional resistive bases:

- the power consumption is reduced to 170 mW, which is one order of magnitude smaller than the power consumption of the conventional passive bases of 1-2 W,
- the maximum external voltage is only 24 V (compared to over 1600 V) which allows a simple and safe control system and eliminates the need for high voltage cables,
- a good voltage stability at changing anode currents and an inherent PMT protection due to the current limitation to 75 μA is given.

5.2.3 Readout

The readout of the charge from the PMT has to satisfy the following requirements:
The electronics has to cover the large dynamic range from the uranium signal with fluctuations in the order of 5-10 MeV equivalent energy, the signal of muons which deposits 300 MeV in an EMC section and a 400 GeV electron shower. This is equivalent to a dynamic range of 80 000 : 1 or 16.5 bits. Secondly the electronic system has to cope with the HERA bunch crossing rate of 10 MHz. In addition the signal from the uranium radioactivity (UNO) which has an average value of about 1.5 MeV/100ns has to be measured with 0.1% accuracy. Figure

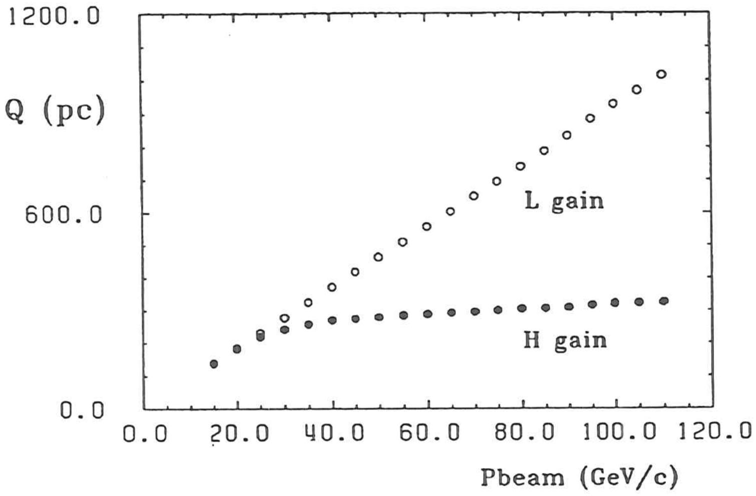

Figure 31: Charge as a function of particle momentum for the high and low gain

30 shows the analog part of the readout electronics designed to satisfy these requirements. The signal of the PMT is processed in three ways for the readout. The path which uses an integrator with a time constant of 20 ms reads the UNO signal. For the measurement of the particles from HERA interactions two readout lines are implemented. These two lines (high and low) are identical except for the gain which is a factor 22.22 higher for the high gain than for the low gain line. While the high gain covers the energy range from 0 to 20 GeV, the low gain saturates at 450 GeV (fig. 31). The different gains are realized by the capacitor ($C_{H/L}$) and the resistor ($R_{H/L}$). At the PMT output the pulse has a full width of 20 ns. The shaper carries out a four fold integration with 33 ns which results in a pulse with a full width of 100 ns.

The shaped pulses are sampled in 96 ns intervals by a switched capacitor delayline, which is 58 cells long. On the issue of a first level trigger, which occurs 5 μs after the interaction, the eight samples in the vicinity of the PMT pulse are transfered to an 8-cell switched capacitor analog buffer within 12 μs, and the delay line is again ready for further data taking. Now the eight samples of 12 readout channels (6 high-gain and 6 low gain) are sent via a multiplexer and a 60 m long cable to the 1 MHz 12 bit ADC's housed in the counting house outside of the detector. The 4 × 58 cell pipeline and the 12 × 8 cell buffer-multiplexer are CMOS-chips specifically developed for the ZEUS Calorimeter. For an assumed maximum first level trigger rate the dead time of the calorimeter rate is about 3%.

Figure 30 also shows a Digital Analog Converter (DAC), which is used for the electronics calibration of the readout through charge injection (Q_{inj}). Each digital card allows the readout of 12 channels (EMC1, ... EMC4, HAC1 and HAC2) for high and low gain. This is just the number of channels for one FCAL tower.

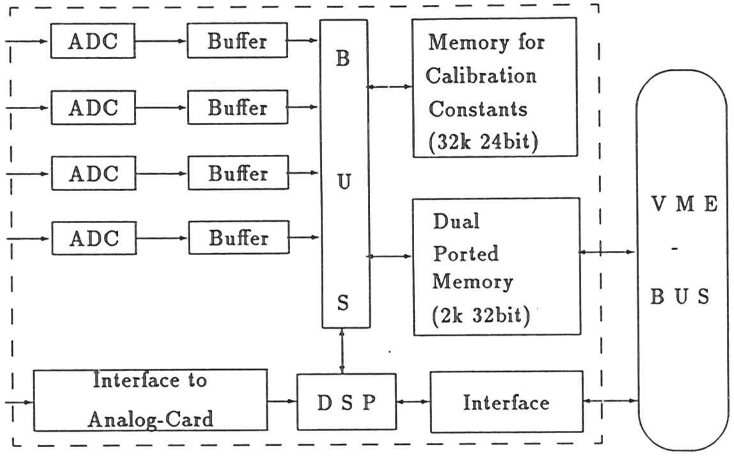

Figure 32: Scheme of a ZEUS digital card

5.3 Digital Card

The digital card is a VME card which is placed, together with all the electronics of the data acquisition system, in the above mentioned counting house. Differential drivers over woven twisted pair cables send the data over the 60 m from the analog cards to the digital card. The task of the digital card is to digitize the analog samples, to calibrate them and deliver them to the DAQ system. Figure 32 shows a simplified block diagram of the digital card. The analog samples are received via the woven twisted pair cables by the analog to digital converters (ADCs). Four of them are placed on each card. Each of the ADCs can digitize a value within 1 μs and has a precision of 12 bit. After the digitization the 12 bit values are buffered in memories.

The central part of the card is the Digital Signal Processor[5] (DSP) a microprocessor with special capabilities for signal processing. It reads the digitized values from the buffer. With some control information from the interface of the control unit of the analog card it determines the pipeline cell number of the first sample. From the on-board memory the DSP reads the corresponding calibration constants. After performing these corrections it writes the values of the calibrated charges into the dual ported memory (DPM) which is connected to the VME-bus. From this DPM the data is read out by the DAQ system.

In addition to the charge the digital card delivers the signal time for the individual channels. It also decides whether to use the high or the low gain to avoid saturation effects. For the processing of the SLT it delivers right, left, EMC and HAC energy sums. As far as possible

---

[5] Motorola 56001

it checks the quality of the data, e.g. it looks for pile up effects and delivers some control information like the trigger and the cell number.

5.4 Calibration Constants

This section is based on the corresponding parts of the work from L.Hervas [HER91]. Each part of the readout chain from the PMT to the ADC is described by an individual calibration constant (see table 6) to achieve the required precision of 1% over the required large dynamical range.

For the conversion from an ADC count to a voltage value the value (K) is used. Additionally it has to be taken into account that the analog card and the digital card have two different ground levels. The different ground levels and possibly existing pedestals are described by a constant A_g. To determine the digitized ground value A_g a signal of 0 Volt is digitized by the ADC. In the next step a signal with the high precision voltage V_{prec} is connected directly over the buffer chips to the corresponding ADC. The ADC count to volt scale is then given by

$$K = \frac{A_{prec} - A_g}{V_{prec}} \tag{6}$$

with A_{prec} as the number of ADC counts corresponding to the voltage V_{prec}. K includes the gains of the cable driver.

In the next step the cable pileup is determined. The long cables cause a long settling time in the cable due to capacitive load and reflections. One can write the relation between the corrected sample S_i^{cor}, the measured sample S_i^{mea} and the previous sample which has been sent over the line S_{i-1}^{mea} as:

$$S_i^{cor} = S_i^{mea} - f S_{i-1}^{mea} \tag{7}$$

By sending pulses of different magnitude and assuming a linear relation the constant f can be determined.

On the analog card are the pipeline (i=1...58) and the buffer cells (j=1..8) which each in principle have their gain (c^p, c^b) and offset voltage (V^p, V^b). A problem is that the pipeline and the buffer cells cannot be measured separately. Each charge which arrives at the ADC has been stored in a pipeline and a buffer cell. Instead of the input voltage V_{input} the voltage

$$V_{i,j}^{output} = (V_{input} c_i^p + V_i^p) c_j^b + V_j^b \tag{8}$$

is measured after the buffer. Without any simplification this would require for each pipeline buffer pair 58 times 8 times 2 (gain and offset) calibration constants. A drastic reduction of the number of these constants can be achieved if one uses the effect that the gains of the cells of a buffer chip are very similar. In fact they are the same within 0.25 %. The error is 0.1 mV which corresponds for the buffer cell capacity of 2 pC (pipeline cell capacity of 1 pC) to a difference in the charge of 0.1 fC (0.2 fC). Under this assumption one can write equation 8 as

$$V_{output}^{i,j} = V_{input} c_i^p c_j^b + (c^b V_i^p + V_j^b) \tag{9}$$

This has the advantage that for $V_{input} = 0$ the offsets V_i^p, V_j^b can be measured without the gains. In a calibration cycle all relevant combinations of pipeline cells (1...8, 2...9, ... , 58...7) are read out via the eight buffer cells. Thus one has $58 \cdot 8 = 464$ offset values. Denoting by

h_{ij} the measured offset for $V_{input} = 0$ and the pipeline cell i and the buffer cell j. One of the h_{ij} is used as a reference (here h_{11}). Instead of the $58 \cdot 8$ offset values only

$$\begin{aligned} \delta^0 &= h_{11} \\ \delta_i^p &= h_{i1} - h_{11} \quad \text{(i=1...58)} \\ \delta_j^b &= h_{1j} - h_{11} \quad \text{(i=1...8)} \end{aligned} \tag{10}$$

which are $1 + 58 + 8 = 67$ instead of 464 quantities have to be stored. For the charge reconstruction the offset can be retrieved as

$$h_{ij} = \delta^0 + \delta_i^p + \delta_j^b. \tag{11}$$

The same principle can be used for the determination of the gain of the cells. To do this a reference voltage of -2V is applied to the input of the pipelines. The outputs are corrected by the pedestals and divided by the inputs relative to the ground

$$gain_{ij} = \frac{h_{ij}^{-2Vinput} - h_{ij}^{0Vinput}}{A_{ref(-2V)} - A_g}. \tag{12}$$

Like in the case for the offsets this is done for all 58 groups of 8 pipeline pipeline cells. The quantities which are kept here are

$$\begin{aligned} g^0 &= g_{11} \\ g_i^p &= g^0 / g_{i1} \quad \text{(i=1...58)} \\ g_j^b &= g^0 / g_{1j} \quad \text{(j=1...8)} \end{aligned} \tag{13}$$

which allow a reconstruction of the gain as

$$gain_{ij} = \frac{g_i^p g_j^b}{g^0}. \tag{14}$$

The relation between the measured and the corrected sample h_{ij} for gain and pedestal is then:

$$h_{corr}^{ij} = \frac{[h_{meas}^{ij}(\delta^0 + \delta_i^p + \delta_j^b)]g^0}{g_i^p \cdot g_j^b} \tag{15}$$

Thus two tables of $1 + 58 + 8 = 67$ constants are necessary for each combination of pipeline and buffer.

The pipeline chips get their input from the shaper. The gain of the shaper a_i is determined in the way that 2 different charge values are injected and the outcoming pulses are compared with the injected one. By the variation of the delay of the pulse signal relative to the clock the rising and falling slope of the pulse are determined. In table 6 these are the constants m^u and m^d.

For the correction of the UNO signal an offset I_{Offset} is needed. To determine this offset the UNO signal is read out with the high voltage turned down to 400 V.

Up to here all calibration constants of table 6 except those of the PMTs have been described.

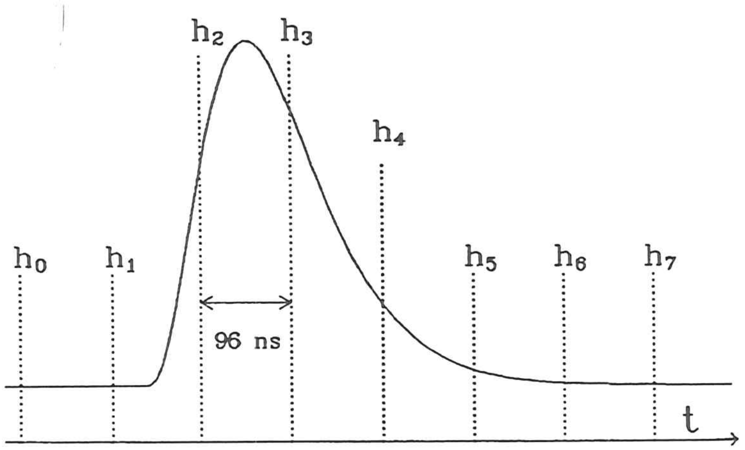

Figure 33: Pulse shape with the 8 sampling points [AND91]

Each photomultiplier has a characteristic gain and noise. The noise produced without any light at the photocathode is called dark current. The parameters of a tube are described by the equation:

$$\log G = \log B + C \times \log V$$

Where G is the gain and V the applied voltage. B and C are calibration constants for each tube. The values of B and C had been determined with a separate test stand before the installation in the calorimeter modules.

As the next step the charge can be reconstructed from the samples. Figure 33 from [AND91] shows the shape of the PMT pulse after the shaper. All pulse shapes are in good approximation identical for all events and channels due to the fact that the PMT pulse is much shorter than the shaping time constant. Using the same notation as in [AND91] the charge q (in $[pC]$) is obtained from the samples H_i by the equation

$$q = q_{norm}[(H_2 - H_0) + R_q(H_3 - H_0)] \tag{16}$$

with

$$R_q = -(dH/dt)_2/(dH/dt)_3 \tag{17}$$

denoting the ratio between the slopes between the samples H_2 and H_3 at the time where $H_2 = H_3$. The value $R_q = 1.8$ was used for all channels while the factor q_{norm} includes various ADC to pC conversion factors and a global channel gain correction. The factor q_{norm} has been determined by the injection of known test charges into each channel. In a further step the charge q is corrected by the ratio (R_I) between the measured and the nominal UNO signal and the global channel pedestal ΔP which has been determined by random triggers:

$$Q = \frac{q}{R_I - \Delta P} \tag{18}$$

This charge Q needs an additional correction due to the shift of the pulse relative to the sampling clock:

$$Q_{corr} = Q/(1 + \sum_{i=1}^{4} a_i T_c^i) \tag{19}$$

with

$$T_c = T_0 + \Delta T \tag{20}$$

T_0 is the overall time of the event as determined by the trigger pipeline clock difference and ΔT is the shift of individual channels due to different transit times in the PMT and the pipeline. The polynominal coefficients a_i can be determined once for all channels.

The time of each channel can be reconstructed in a similar way like the charge:

$$T = \frac{H_2 - H_3}{S_Q \cdot Q} \tag{21}$$

with

$$S_Q = [(dH/dt)_2 - (dH/dt)_3]/Q \tag{22}$$

For the time T in ns the constant S_Q has the value 0.81 for all channels. Similar to the charge Q the time T needs a correction for asynchronous events.

$$T_{corr} = -\Delta T - \sum_{i=1}^{4} b_i T^i \tag{23}$$

Again the polynominal coefficients b_i are used for all channels. The UNO current I_{UNO} as used above is determined as

$$I_{UNO} = \frac{(V_{UNO} - V_G)}{R_M} - I_0 \,. \tag{24}$$

V_{UNO} is the UNO signal and V_G is the reference ground value. $R_M = 3.48 M\Omega$ is the value of the integrator resistor for the analog front end cards of the FCAL. I_0 finally is the pedestal of the UNO current measured with the high voltage of the PMTs set to 400 V.

All together there are 279 calibration constants per channel and 37 additional constants which are common for all channels.

Symbol	Description	Number/PMT	Number/FCAL-Tower
$log(B), C$	describe PMT gain vs. Voltage	2	24
a_i	PMT+shaper gain,nonlinearity map	2	24
m^u, m^d	shaper pulse slopes	4	48
δ_i^p	pipeline relative pedestals	116	1392
δ_i^b	buffer relative pedestals	16	192
δ^0	pedestal reference	2	24
g_i^p	pipeline relative gains	116	1392
g_i^b	buffer relative gains	16	192
g^0	gain reference	2	24
V_G	digitized ground value	1/6	2
k	ADC counts to volt scale	1/6	2
f	cable pileup correction	1/6	2
I_0	DU current offset	1	12

Table 6: List of calibration constants

6 Calibration of the ZEUS Calorimeter

This chapter describes the calibration of the calorimeter [AND91] i.e. the relation between output signal of the PMT to deposited energy. Several unknown and not necessarily stable constants contribute to the value of the PMT signal. These constants cancel in the ratio (particle signal / UNO signal). If the ratio for every cell is known then the measurement of the UNO signal is be sufficient to calibrate the cell. In the following it is described how the ratio (particle/UNO) is obtained.
The calibration procedures, which have been developed for the ZEUS calorimeter are:

- A set of beam independent (so called beam off) calibration procedures has been developed. One of these procedures is the charge injection (Q_{inj}) for the calibration of the analog part of the readout which has been already described. The overall noise of the readout electronic is determined with randomly triggered events. A light injection system (LED/LASER System) allows the check of the readout system from the PMT up to the digital card. Finally the whole signal chain starting with the scintillator can be checked with cobalt sources and with the uranium signal. This set of measurements allows the determination of the calorimeter parameters at every moment during the experiment.
- A selected sample of all the modules has been calibrated extensively with various particles at different energies to investigate the calorimeter response and the accuracy of the calibration. For the FCAL/RCAL modules, the beam of the CERN SPS has been used.
- All of the calorimeter modules have been checked with cosmic muons. For the FCAL/RCAL modules this was done just prior to the installation of the modules in ZEUS.

6.1 Beam Independent Calibration Methods

6.1.1 Overview

Figure 34 shows an overview of the beam off calibration methods. The electronics read out system is calibrated via charge injections into the signal lines as described in the previous chapter. Events read out by the issue of random triggers allow the determination of the noise of the channels. Light pulses illuminating the wavelength shifter directly in front of the photomultiplier allow the monitoring of the photomultiplier tubes. The small but very stable signal from the uranium radioactivity is always available for every channel and is used as a reference of the energy scale. ^{60}Co sources which can be pushed along the modules allow the check the light yield and attenuation length of every scintillator tile as well as the uniformity of the wavelength shifter.

6.1.2 Random Triggers

Events generated by a random trigger are used to determine the noise of the channels. The RMS of the charge of these events has values between 0.08 pC (8 MeV equivalent energy) for FEMC channels and 0.14 pC (13 MeV) in the channels of the HAC sections. The dominating

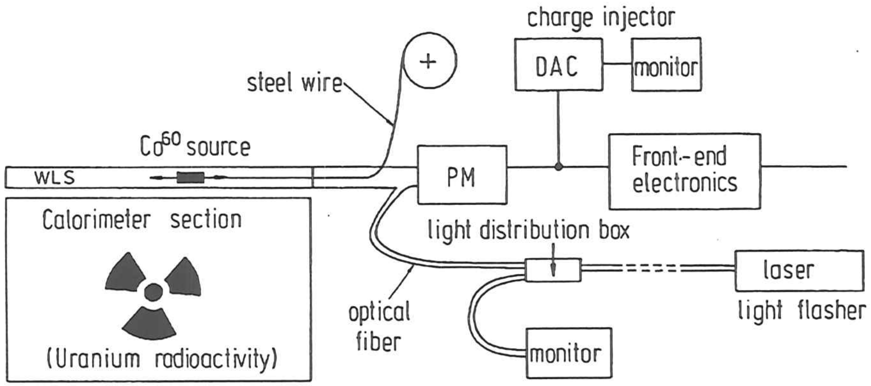

Figure 34: Off beam calibration apparatus [AND91]

part of the noise is due to the radioactivity of the uranium. By reducing the high voltage of each the photomultipliers to 400 V (compared to more than 1000 V for the usual operation) the electronic component of the noise has been determined to 0.04 pC.
Measured pedestals are subtracted from the data before the analysis. The influence of the noise on the reconstruction is described in section 9.6.

6.1.3 Light Pulser System

Figure 34 from [AND91] shows the principle of this system. A light guide is connect to the WLS in front of the PMT (figure 34) for coupling light pulses into the wavelength shifter. A laser sends its light over a fiber to a distribution box. At the distribution box optical fibers transport the light to the WLS and to a monitor. The monitor measures the pulse to pulse fluctuations of the laser. The light distribution box spreads the light of the incoming fiber to $\approx$ 100 further fibers. Each of these 100 fibers leads to a further distribution box to reach all at all 13 000 WLS. Because of its high intensities the laser system can be used for linearity measurements of the low gain channel and for the cross calibration between the high and the low gain. Filters allow the change of the light intensities over of several factors of 10. The number of photoelectrons per measured charge (n_{PE}/Q) have been determined with the laser. Long term stability checks also can be done with LED pulsers which are part of the system. The LED pulsers offer the advantage of a very high reliability but have the disadvantage of longer pulse length than the pulses of the beam particles and the laser.

6.1.4 Cobalt Source Calibration

This calibration method [AND91] tests the optical system of the scintillator and the WLS. For this purposes ^{60}Co sources of 1 mm length and 0.7 mm diameter are moved by a steel wire through brass tubes which are placed between the WLS of the EMCs transverse to the

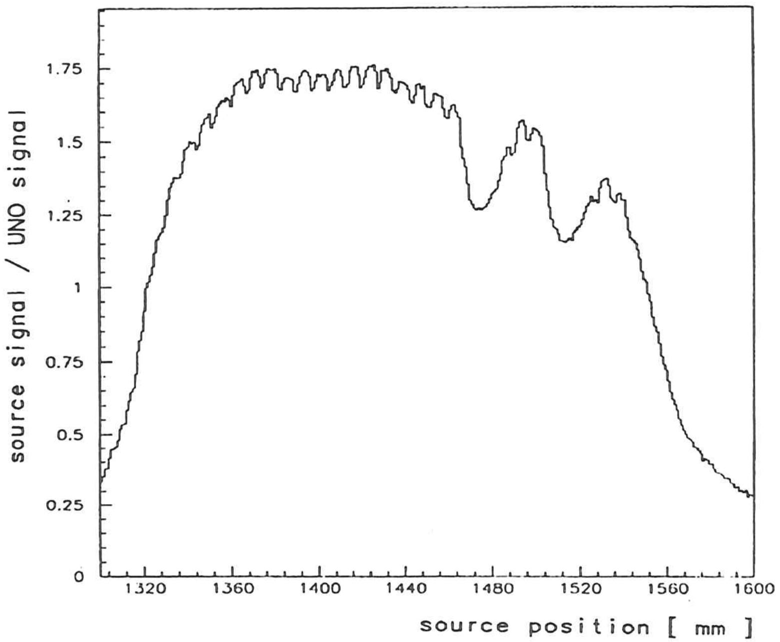

Figure 35: Cobalt scan along an EMC section of the FCAL [AND91]

scintillator (see also figure 29). This method allows to monitor the light yield of each of the scintillator plates. Figure 35 shows a typical scan along the EMC section of a FCAL module. Each dip in the line corresponds to a uranium plate and each peak to a scintillator tile. Also the two gaps for the Hadron Electron Separator (HES) can be seen clearly. Several mechanical assembly faults of the modules could be found and repaired before the module installation in ZEUS. During the experiment this method will be used to determine aging effects of the scintillators and the WLS.

6.1.5 Uranium Signal (UNO)

The possibility of a calibration with the uranium signal (UNO) is one of the major advantages of the calorimeter type chosen. The decay chain of $^{238}_{92}U$ is shown in figure 36 (from [AND91]). The decay chain has several steps and ends at the uranium isotope $^{234}_{92}U$ which has such a long lifetime that the decay into $^{206}_{82}Pb$ over 11 further steps does not contribute to the UNO signal. Most of the energy ($\approx$ 80%) is carried by the α particles. Because of their small range (7 μm in uranium), the α-particles are stopped either in the DU plate or in the stainless steel cladding. 20 % of the energy is carried by β particles and 1 % by γ particles. The signal from the uranium radioactivity is sensitive to thickness of the cladding of the uranium plates.

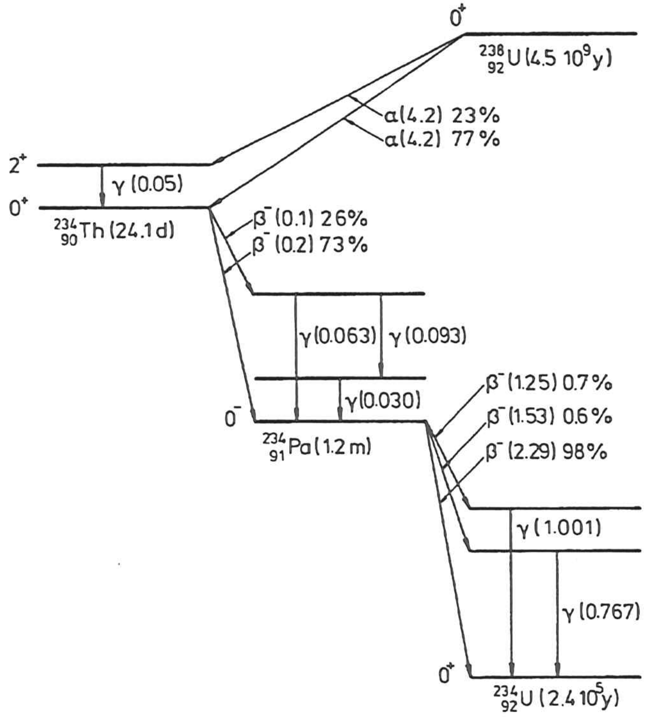

Figure 36: Decay steps for U238 [AND91]

Dose measurements show that the signal reduction for 0.2 mm iron will the 70 % and 90 % for 0.4 mm iron. This effect will be discussed quantitatively in section 8. Because of the long lifetime of uranium of 4.5 10^9 years the uranium noise signal is extremely stable.

The module to module intercalibration with the UNO signal is done in the following way. The only parameter which can be varied to modify the ADC counts for a specified light dose in the scintillator is the high voltage of the PMTs. Thus the UNO is used to adjust the high voltage of the PMTs. For this procedure the high voltage of each individual PMT is set such that its current from the integrated UNO signal reaches the nominal values within an accuracy of 1 %. These nominal values are:

- 100 nA for FEMC channels,
- 200 nA for REMC channels
- 400 nA for FHAC0 and RHAC0 channels
- 500 nA for FHAC1 and FHAC2 and RHAC1 channels

scan number	run type	events per run	comment
1	UNO	1000	I_{UNO} measurement
2	$Q_{inj}(10pC)$	1000	gains for Q_{inj}
3	$Q_{inj}(80pC)$	1000	gains for Q_{inj}
4	Random	1000	pedestals for beam
5	LED(AC)	1000	PM monitoring
6	LED(DC)	1000	PM monitoring
7	laser	1000	PM monitoring

Table 7: The calibration cycle without beam particles performed every 8 hours

The ratio between these nominal values is determined by the ratio between the areas of the scintillator tiles of the different sections (FEMC, REMC etc.) and by a factor which takes the different cladding thickness into account.

Due to the adjustment of the high voltages according to the nominal UNO currents all measured calorimeter signals are normalized to the UNO current.

6.1.6 Complete Off Beam Calibration Procedure

Table 7 shows the complete beam independent calibration cycle. During the calibration of the calorimeter modules at CERN this calibration cycle has been carried out every 8 hours. Measurements on the stability of the uranium signal [BEH89] had shown that this time is sufficient to keep time variations below 0.3%.

6.2 Absolute Energy Calibration With Beam Particles

Only beams of particles with known energy allow a determination of the absolute energy scale relative to the UNO signal.

In addition two types of particle sources have been used for the calorimeter calibration. Momentum selected beam particles and cosmic ray muons. 10 modules have been extensively tested at a test beam of CERN. Before the installation at ZEUS a final quality control and calibration has been done for all modules with cosmic rays.

In addition beam particles have been used to study other performance parameters like energy and position resolution, response uniformity, line shape of the muon signal etc.

6.2.1 Experimental Setup of the Beam Tests

Test Beam The calibration of calorimeter modules with beam particles was done between August 1989 and July 1990 in the X5 beam of the CERN SPS [6]. This is a tertiary beam which is generated by 120 GeV/c pions (π^-) interaction in Be, Cu or Pb targets. The interaction between the pions and the targets delivers acceptable rates of negative charged particles from 10-110 GeV. A beam spectrometer, consisting of magnets and wire chambers

---

[6] Super Proton Synchrotron

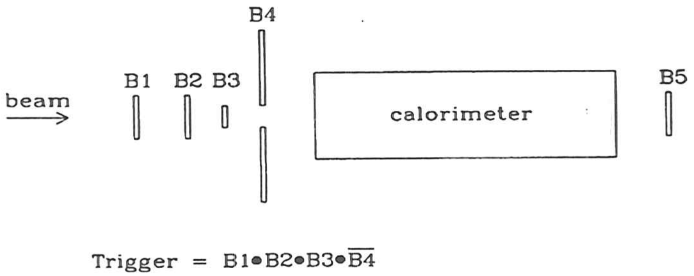

Figure 37: Setup of the trigger system at CERN [AND91]

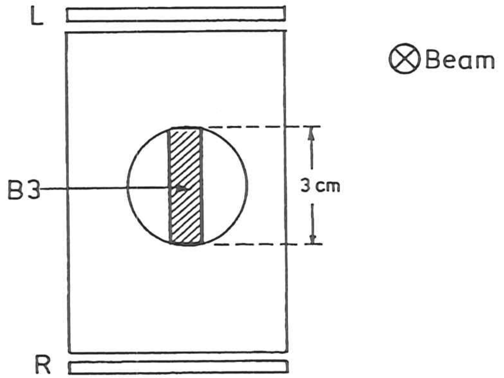

Figure 38: Trigger counter B3 to veto beam halo particles [AND91]

allows a precise measurement of the beam momentum of each individual particle. Due to chamber inefficiencies a momentum reconstruction for 85 - 95% of the events was possible. The uncertainty in the absolute momentum scale is estimated to 0.8%. It is given by alignment uncertainties of the wire chambers and the knowledge of the field integral of the bending magnet between them.

Trigger Setup Figure 37 shows the trigger set up. A trigger was defined as the coincidence of signals in the three scintillation counters (B1, B2 and B3) and no signal in the veto counter B4. Trigger counter B5 was read out to tag muons.
The trigger counter B3 (see figure 38) which has a width of 6 mm was used to define the incident beam position. It is followed by the trigger counter B4 (see also figure 38), which has a hole with a diameter of 3 cm to veto beam halo particles. While beam particles have been selected by the choice of the target and insertion of Pb-absorbers (to remove electrons)

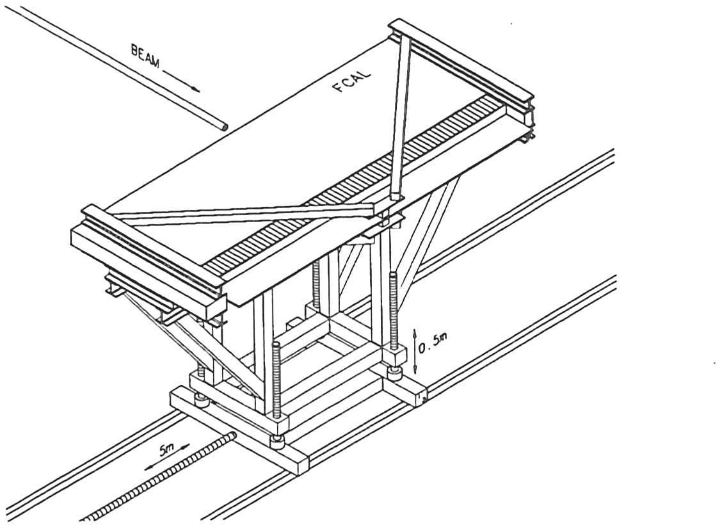

Figure 39: Support frame for the calibration of the FCAL and RCAL modules [AND91]

no further event selection has been done on the online trigger level. The calorimeter itself has been used for the final beam particle identification in this energy range which was done offline.

Mechanical Setup On the basis of the measurement of 10 modules,

- 6 of the 24 FCAL modules and
- 4 of the 24 RCAL modules,

it has been concluded that it is not necessary to test all modules in the beam. All these modules were of the maximum size with 23 towers of 20cm*20cm each and an overall length of 4.6 m. All modules have been calibrated in horizontal position bolted to a support frame (figure 39). The modules were positioned relative to the beam to about 1mm; the reproducibility of the motion has been 0.5 mm for the vertical position and 1 mm for the horizontal position. This is sufficient for the required purpose because the beam had a extension of 3 to 4 mm. The movement of the support frame was controlled by the slow control setup of the DAQ-system for CERN (figure 40). The setting of the high voltages has been done also by the slow control system. The readout of the PMTs via the front end cards was done with a transputer based VME system. The overall control and the data storage to tape was performed by a μVAX.
For the calibration of the EMC sections electrons and for the calibration of the HAC sections

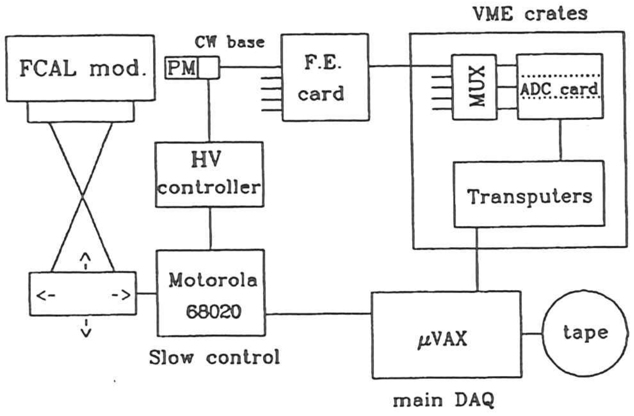

Figure 40: DAQ and control system for the FCAL and RCAL calibration [AND91]

have been used. The calibration of both EMC and HAC sections have been done with muons and hadrons.

6.2.2 Calibration With Electrons

Electrons of 15 and 100 GeV have been used for the calibration. The electrons have been produced by the interactions of 120 GeV pions in a lead target. For 15 GeV the particle beam consisted to nearly 100% of electrons. To select a pure electrons sample the following cuts have been applied. At first it has been required that the signal in the EMC sections has to be between 110 and 180 pC. This corresponds to a 5 sigma cut for the Gaussian shaped energy distribution of the electrons. Electrons deposit all their energy in the EMC section. Muons and hadrons loose their also in the hadronic sections of the calorimeter. Therefore all events have been rejected where in the HAC1 section a PMT charge of more than 15 pC have been measured. Figure 41 shows the resulting energy distribution which is to a very good approximation Gaussian shaped. This plot has been obtained by superimposing the events from all sections of one module.
The strategy and the exact values of these cuts have been determined during extensive investigations which have been started during the tests at the FCAL prototype tests [BEH89]. The cuts for the FCAL and RCAL calibration which are presented here for electrons, muons and hadrons are listed in the publication [AND91].
At 100 GeV the beam consisted to 50% of electron and to 50% of muons and hadrons. The same technique has been applied for their selection as for 15 GeV electrons but at a different

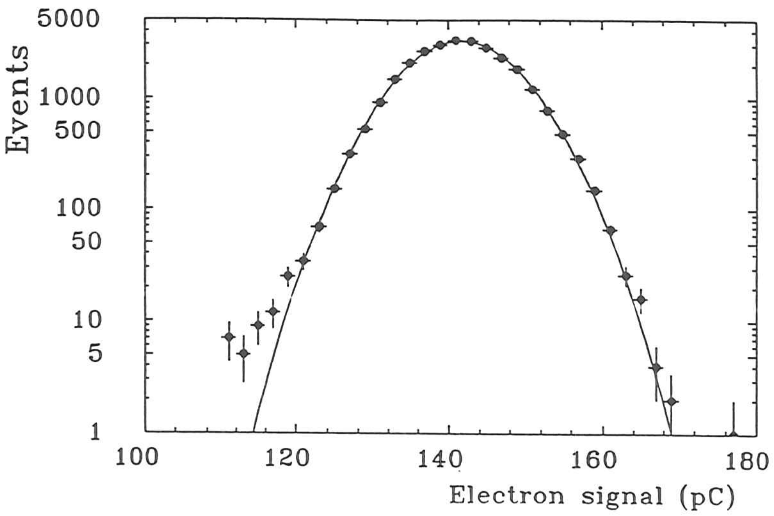

Figure 41: Energy distribution with high statistics, obtained by superimposing the events (15 GeV electrons) of all sections of one module [AND91]

energy scale. It has been required that the signal in the EMC sections has to be between 800 and 1100 pC. The signal in the HAC1 sections has to be less than 100 pC. When the electron beam has been directed into the center of a 5 × 20 cm^2 section of a FCAL, the leakage to neighbouring strips is 4 %. Table 8 shows the beam tests which had been done with every module. To check the reproducibility of the beam calibration a scan with 15 GeV electrons has been done at the beginning and at the end of each calibration cycle. The comparison between the two calibration runs shows a reproducibility between the runs of the e/UNO signal within the statistical errors of 0.3 to 0.4 %. This shows that the normalization of the particle signals provides the required precision. Only these events have been accepted which appeared within $\pm 15 ns$ of the trigger signal therefore only 500 events per cell were available for these calculation. The time cut has been applied to do the charge reconstruction from the eight charge samples without any timing corrections.
To test the stability of the calibration procedure, one module (FCD1) has been calibrated twice: in December 1989 and March 1991. The test results agreed within 0.4% . This shows that the calibration is also stable in the long term.

Linearity An energy scan with electrons in the momentum range from 15 to 110 GeV with one FCAL and one RCAL module has been done. Figure 42 shows the results for the FCAL module and figure 43 for the RCAL module. The deviation from linearity shown in the figure has been defined as:

$$\delta = \frac{Q/p}{Q_0/p_0} - 1 ,$$

scan number	particles	E (GeV)	events per run	runs F12(11)	runs R12(11)	sensitive sections
1	electrons	15	2000	74(80)	40(42)	EMC(H/L)
2	electrons	100	2000	74(80)	40(42)	EMC(L)
	+ muons		2000			EMC(H)
3	hadrons	100	5000	23	23	HAC(L)
	+ muons		10000			HAC(H)
4	electrons	15	2000	74(80)	40(42)	EMC(H/L)

Table 8: The test cycle with beam particles performed for each module. The column sensitive sections lists these sections and gains (high/low) where a precise signal from the beam particles can be read out.

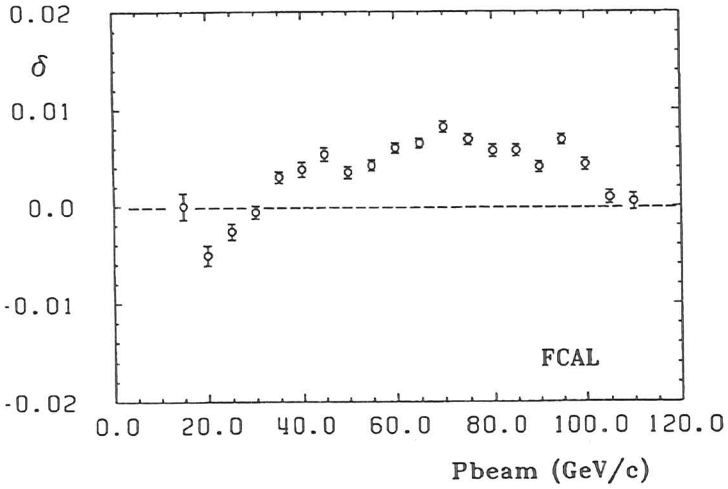

Figure 42: FCAL module deviations from linearity as a function of the electron energy [AND91]

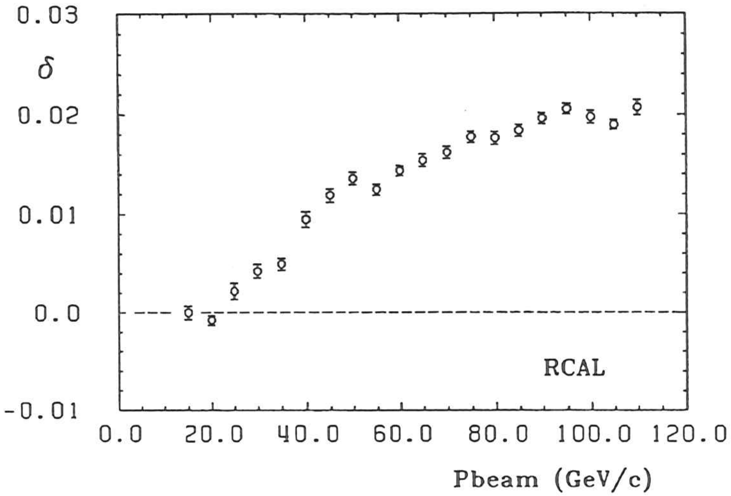

Figure 43: Deviations from linearity for a RCAL module as a function of the electron energy [AND91]

where Q_0 is the charge and p_0 is the momentum at 15 GeV. While the linearity of the FCAL module is well within 1.0%, for the RCAL the nonlinearity is 2.2% . This is in agreement with the results which have been derived from the comparisons between the 15 GeV and the 100 GeV scans done on all modules. Therefore the effect can be corrected offline.

6.2.3 Other Tests With Electrons

Uniformity Along a Module Figure 44 shows a uniformity scan along an FCAL module perpendicular to the beam with 15 GeV electrons. The dips which occur every 5 cm are due to the ~ $0.5mm$ scintillator gaps between the EMC sections. Between these sections the signal drops 4%. All dips look the same which indicates the good uniformity between the towers. Between the towers (not shown) the signal drops by about 7%. For the RCAL modules the uniformity is generally worse. For this test the beam size has been defined with the finger counter B3 (see figure 38).

Energy Resolution The energy resolution for 15 GeV/c electrons is $17.6\%/\sqrt{E}$ for the FCAL modules and $17.4\%/\sqrt{E}$ for the RCAL modules. Figure 45 shows the energy resolution as a function of the electron energy for a FCAL module. Even at very high energies the resolution is only slightly worse than $17.4\%/\sqrt{E}$. Monte Carlo simulations predict an energy resolution of $16\%/\sqrt{E}$ due to sampling fluctuations. The remaining part of the energy resolution is due to photostatistics.

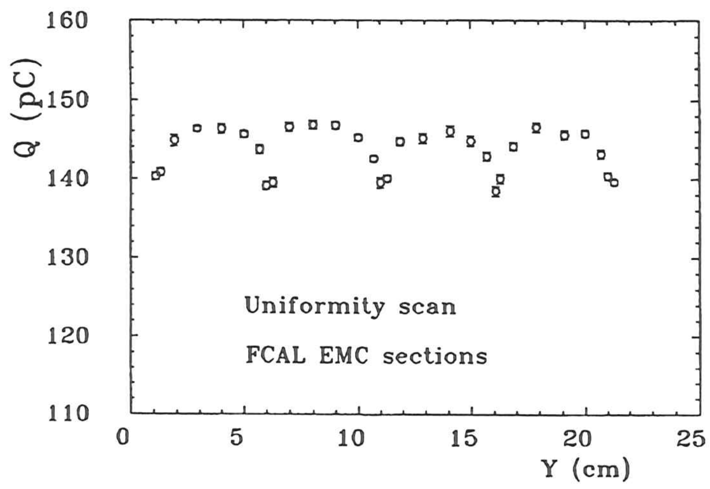

Figure 44: Measured charge of the PMTs in the EMC sections versus the incident beam position along the front side of a FCAL module [AND91]

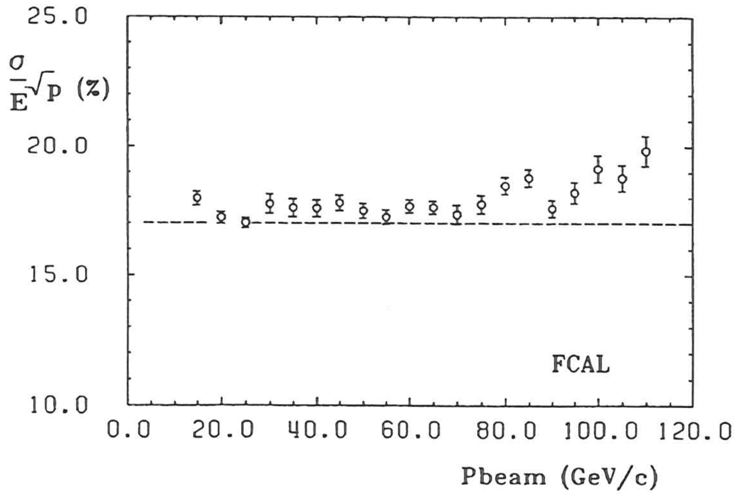

Figure 45: Energy resolution for electrons of a FCAL module at different energies [AND91]

0.01	0.02	0.07	0.04	0.07	0.02	0.01
0.02	0.09	0.25	0.30	0.25	0.09	0.02
0.07	0.25	1.3	3.7	1.3	0.25	0.07
0.04	0.30	3.7	75.5	3.7	0.30	0.04
0.07	0.25	1.3	3.7	1.3	0.25	0.07
0.02	0.09	0.25	0.30	0.25	0.09	0.02
0.01	0.02	0.07	0.04	0.07	0.02	0.01

Figure 46: Lateral distribution of 30 GeV/c hadron showers. Each cell represents a 20 × 20 cm^2 calorimeter tower of the calorimeter prototype. The beam is incident in the middle of the central tower and the sum of all cells (EMC+HAC1+HAC2) is normalized to 100. [BEH89]

Energy Scale The measurement of the beam momentum with the beam spectrometer allowed a determination of the absolute calibration scale of the calorimeter. With the data taken at the CERN test this has been determined to

$$1GeV \sim 9.51pC \ .$$

6.2.4 Tests With Hadrons

Hadrons with 100 GeV/c have been used for the calibration. The hadrons were selected by demanding a signal in $EMC + HAC1$ sections between 400 and 1000 pC, but smaller than 850 pC in the EMC section (from [AND91]). The first cut removes muons, the second cut rejects electrons which deposit nearly all of there energy in the EMC section.
Like the other particle signals the hadron signals have been normalized by the UNO signal. The module to module variations of these h/UNO signals are on the 1% level if the total energy of the towers is considered. This justifies the assumption that the UNO calibration provides an accuracy of 1% for the HAC sections, too.
A single module does not provide full containment for a hadron shower (see figure 46). Thus the studies of the e/h ratio and the energy resolution for hadrons and the intercalibration between the EMC and the HAC sections cannot be done with setup. They have already been measured with a prototype calorimeter of similar construction [BEH89].

6.2.5 Calibration With Muons

The dominant mechanism for muon energy loss in matter at low energies is ionization. This results in an asymmetric distribution function of the energy loss in a section. Muons offer several advantages for the calibration. The transverse ionization processes are limited to a radius of one millimeter [KRA90]. Thus, well defined muon trajectories allow precise investigations of the homogenity of scintillators. Muons have the same energy deposition in all calorimeter regions and offer, therefore, a tool for the intercalibration of the EMC and HAC sections. The low energy deposition of muons, about 300 MeV in the EMC sections, allows together with electrons linearity tests in the low energy region.
Despite the fact that muons offer a good calibration tool, the analysis of their energy distribution is not simple. The long tail in this function results in a large spread which introduce large errors if one simply uses the arithmetic mean. A more accurate result is determined if the proportional response function is fitted to the data.

Beam Muons Muons from the decay of mesons are present in unseparated particle beams. For example, the 100 GeV/c hadron beam produced by the interaction of 120 GeV/c pions on a copper target consisted of 30% hadrons and 70% muons. Thus, a large flux of high energy muons was available. While the muon energy is not of prime importance, it has to be well above 2 GeV. Muons below this energy are stopped in the FCAL modules.
The selection of muons from hadrons could easily be done with cuts which use the difference in the energy deposition of hadron showers compared to muons. The cuts demand a signal between 1 and 40 pC in the EMC section which was exposed to the beam but smaller than 120 pC in the total calorimeter. For the HAC sections the cuts require a signal between 3 and 80 pC in the corresponding HAC section and smaller than 120 pC in the whole calorimeter [AND91]. Additionally it has been required that the difference between the two PMTs which read out a calorimeter cell is less than 3 pC. This cut rejects events where a scattered muon leaves the center of the cell and traverses a WLS of a cell [TSU91]. Each data set consists of approximately 2000 events for the electromagnetic sections and of about 5000 events per tower for the hadronic sections.

Cosmic Muons Before the installation of FCAL and RCAL in ZEUS every calorimeter module has been extensively checked in a cosmic ray setup. At sea-level the flux of muons is $9.4 \pm 0.05 * 10^{-3}$ muons $cm^{-2}sterad^{-1}s^{-1}$ [ALL75]. With the cosmic ray muons the whole chain from the scintillator over the wavelength shifter to the PMTs and the electronics has been checked. For the triggering of the muons scintillation counters [STR89] have been placed on top of the module in front of the EMC section and below the modules under the end beam. The measurements with this setup lasted from September 1990 to April 1991. To obtain a sufficient statistical accuracy a number of 2000 events per tower $\sim$ 4 days of data taking were needed.
Further cosmic ray tests have been done after the installation of the modules in ZEUS and during periods without beam. These tests will provide a tool for cross checks during the whole lifetime of the experiment.

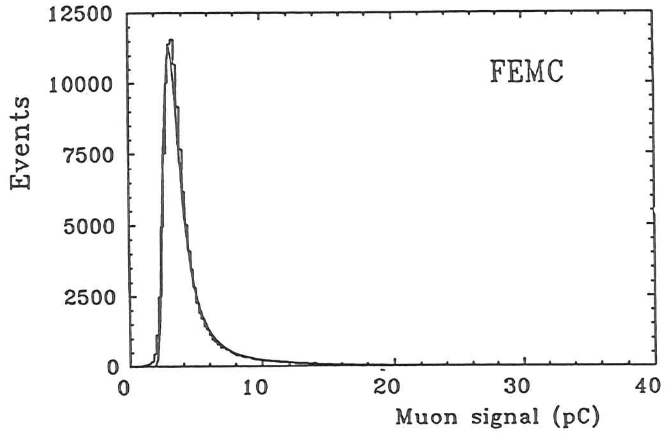

Figure 47: Energy distribution of muons over all EMC sections of all 6 FCAL modules calibrated at CERN (from [AND91])

7 A High Precision Calibration Procedure with Muons

7.1 Motivation

As already mentioned, muons provide a means to calibrate the calorimeter, because, at not too high energies, they deposit energy in the calorimeter mainly by their ionization loss. This energy loss as measured by the signals in the calorimeter depends on the details of the calorimeter and the readout and only weakly on the muon energy. Muons are therefore a useful tool for intercalibration studies. A number of tests with ZEUS calorimeter modules were made with muons from the CERN test beams. As an example Figure 47 shows the distribution of the energy loss of muons in the EMC sections of the ZEUS calorimeter. It deviates from a Gaussian shaped distribution and has a long tail towards higher energies. The aim of the calibration is to use the mean energy loss of muons to find the relation between the signal and the deposited energy for the different sections of the calorimeter.
The straight forward method is to calculate the mean value and the rms of the distribution directly from the data. This is a good method if the data is normally distributed. Therefore this method has been successfully used for the energy loss distribution of electrons in the EMC sections. If the same is done for the energy distributions of the muons, big errors of the mean values result because of the long tail towards higher energies. A better method is to fit the energy loss function to the data.
At first the energy loss of muons in matter will be explained. Then the fit with a Landau

function will be shown as well as the calculation of the mean value by means of a truncated Landau function. Finally the results of this method for the calibration of the ZEUS FCAL and RCAL modules will be given.

7.2 Energy Loss of Muons in Matter

The following transport equation describes the energy loss of heavy charged particles, which penetrate a thin layer of material [SEL62]:

$$\frac{\partial f(x,\Delta)}{\partial x} = \int_0^b \omega(\epsilon) f(x,\Delta-\epsilon)d\epsilon - f(x,\Delta)\int_0^{\epsilon_{max}} \omega(\epsilon)d\epsilon \tag{25}$$

$$b = \Delta \text{ for } \Delta < \epsilon_{max} \text{ and } b = \epsilon_{max} \text{ for } \Delta > \epsilon_{max}$$

$f(x,\Delta)$ is the unknown distribution function. It is the probability that a particle with some defined initial energy E_0 traversing a layer of thickness x will lose an amount of energy between Δ and $\Delta + d\Delta$. $\omega(\epsilon) = \omega(E,\epsilon)$ is the single scattering collision-loss law which is the probability (per unit length of the path) of an energy loss ϵ for a particle of the energy E. Furthermore it is assumed that the energy loss ϵ is small compared to the initial energy of the particle E_0. ϵ_{max} is the maximum energy which can be transfered during one collision. This equation has been solved by Landau [LAN44] and Vavilov [VAV57]. The difference between their calculations arises from the maximum energy (ϵ_{max}) which can be transfered at a single collision. Landau made the assumption that the energy transfer is unlimited. Vavilov corrected this assumption and introduced an upper limit for this energy . This more accurate assumption results in a more complicated solution for the transport equation [SEL62]:

$$f(x,\Delta)\, d\Delta = \frac{1}{\xi}\phi_V(\lambda_V,\kappa,\beta^2)\, d\lambda_V, \tag{26}$$

where

$$\begin{aligned}
\phi_V(\lambda_V,\kappa,\beta^2) &= \frac{\kappa}{\pi}e^{\kappa(1+\beta^2\gamma)}\int_0^\infty e^{\kappa f_1}\cos(y\lambda_V+\kappa f_2)dy \\
\lambda_V &= \frac{\Delta-\bar{\Delta}}{\epsilon_{max}} - \kappa(1+\beta^2-\gamma) \\
\gamma &= 0.577216\ldots \quad \text{(Euler's constant)} \\
f_1(y) &= \beta^2[\log y + Ci(y)] - \cos y - ySi(y) \\
f_2(y) &= y[\log y + Ci(y)] - \sin y + \beta^2 Si(y) \\
Si(y) &= \int_0^y \frac{\sin u}{u}du \quad \text{(sine integral)} \\
Ci(y) &= \int_{-\infty}^y \frac{\cos u}{u}du \quad \text{(cosine integral)} \\
\beta &= \frac{v}{c} \\
\kappa &= \frac{\xi}{\epsilon_{max}}
\end{aligned}$$

While the Landau function does not depend on any parameter, the Vavilov function ϕ_V depends on two parameters (β and κ). β is the velocity of the incoming particle. ξ is the average energy deposited in the length x. Three cases of the Vavilov-Function according to three regions of κ can be distinguished:

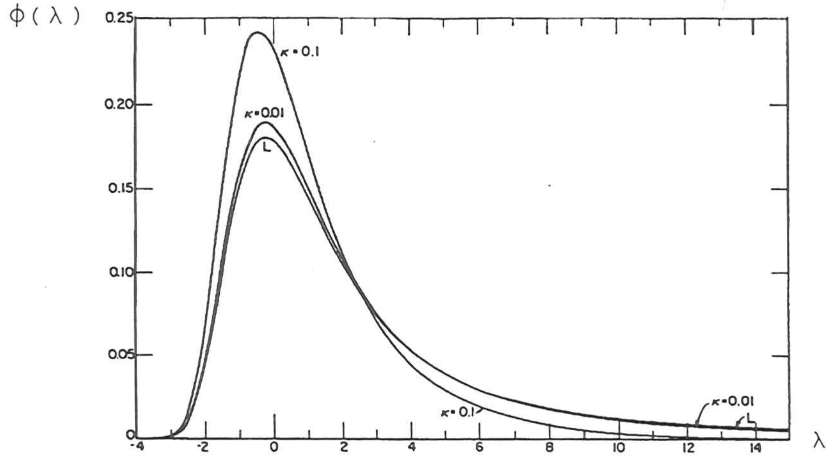

Figure 48: Vailov function for $\beta^2 = 0.9$ and the Landau function L (from [SEL62])

$\kappa \geq 1.0$	There are many collisions per energy loss interval. Thus there are smaller statistical fluctuations and the resulting distribution approaches a Gaussian.
$0.01 \leq \kappa \leq 1.0$	The Vavilov-function is in between the Landau-function and a Gaussian.
$\kappa \leq 0.01$	Only few collisions per energy loss interval occur in this region. This results in a Poisson distribution with large statistical fluctuations per energy loss interval. The distribution is the Landau distribution with its long tail to high energies.

Landau solved the transport equation via an inverse Laplace transformation. He discovered that the solution of the distribution function $f(x,\Delta)$ can be written as a product with a factor containing all the physical constants and a universal function $\phi(\lambda)$ of the dimensionless variable λ. $\phi(\lambda)$ is the so called Landau density.

$$f(x,\Delta) = \frac{1}{\xi}\phi(\lambda) \tag{27}$$

Figure 48 shows the Vavilov function for some values of κ (and $\beta^2 = 0.9$) as a function of the variable λ. λ is related to the energy via a linear transformation namely

$$\lambda = \frac{\Delta - a}{b}\ ,$$

where a, b are adjustable parameters or, if the energy loss Δ is expressed by the total charge Q measured by the PMT's we have

$$\lambda = \frac{Q - S}{W}\ ,$$

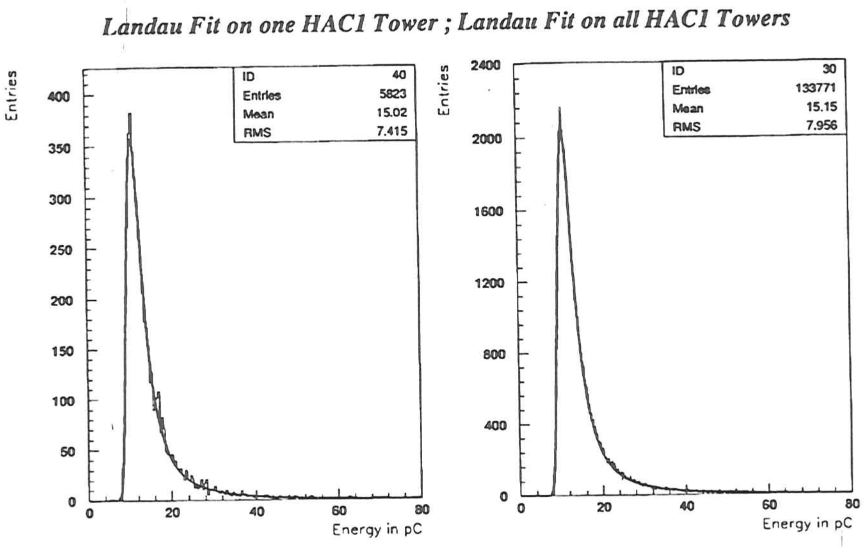

Figure 49: Energy distribution of the muon signal in the FCAL, compared with a Landau distribution. Left: using the data of one HAC1 tower and right: using the data of all HAC1 towers.

when S, W are parameters which depend on the maximum value of λ, λ_{max}. The Landau distribution is denoted by L.

Program packages exist for both functions. Since the Landau function is only a special case of the Vavilov function the package of B.Schorr [SCH74] may be used for both functions. The package for the Landau function only [KOE84] has a better accuracy in the long tail and a faster computing time. For the investigations 100 GeV muons have been used. The measured muon signal is already normalized using the UNO signal. Figure 49 shows a fit of the Landau function to the energy distribution of muons in the HAC1 sections. The used module FNL4 has 23 towers and therefore 23 HAC1 sections. Approximately 5800 muons have been shot at the center of each tower. The left plot in figure 49 shows the energy distribution for a single tower. For the plot on the right side all the measured muon energies of the 23 HAC1 sections have been filled into one histogram to get a high statistics distribution. A Vavilov function with a very small $\kappa \ll 0.01$ describes the data best. But the Landau function also provides a good fit as the deviations between the Landau function and the Vavilov function are very small. The χ^2/NDF which gives an indication that the quality of a fit is acceptable. Because of the good agreement of the Landau function ([KOE84]) with the data and its fast computing time this package has been used for the fitting.

It should however be noted, that part of this good agreement may be fortuitous, because for 100 GeV muons the mechanism of energy loss is a bit more complicated: The table 9 shows that in uranium muons with 100 GeV lose only 54% of their energy due to ionization and

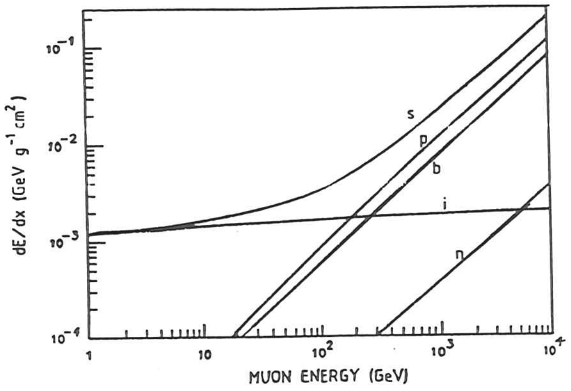

Figure 50: Enery loss of muons in uranium (from [LOH85])

Material	dE/dx [$GeV cm^2/g$]	Ionization	Brems-strahlung	Pair production	Nuclear interaction
Hydrogen	5.381×10^{-3}	97.28 %	0.8527 %	1.001 %	0.8636 %
Iron	2.741×10^{-3}	78.86 %	8.156 %	1.158 %	1.405 %
Uranium	3.232×10^{-3}	54.24 %	17.95 %	26.75 %	1.055 %

Table 9: Energy loss of 100 GeV muons in the materials of the calorimeter

the remaining energy goes into bremsstrahlung and pair production. The data of table 9 is based on investigations [LOH85] on the energy loss of muons over a wide range of energies for several materials. As an example figure 50 shows the contributions to the energy loss in uranium for ionization (i), bremsstrahlung (b), pair production (p), nuclear interactions (n) and their sum (s) in the energy range between 1 and 10000 GeV.

Thus the good description of the data by the Landau function is fortuitous, as it is expected to describe only the ionization part of the energy loss. Sometimes the so called Moyal function which can be written analytically is used to describe energy loss distributions:

$$f_M(\lambda) = \frac{1}{\sqrt{2\pi}} \exp(-\frac{1}{2}(\lambda + \exp(-\lambda)))$$

Moyal himself ([MOY54]) calls his function an *'explicit expression for Landau's distribution'*. The two functions are different as can be seen in figure 51 The Moyal function in figure 51 does not fit the data of a single subtower. The convolution with a Gaussian function improves the fit only slightly. The disagreement of the function and the data in the long tail of the latter is not solved by a convolution.

Therefore the Landau function has been used to fit the data.

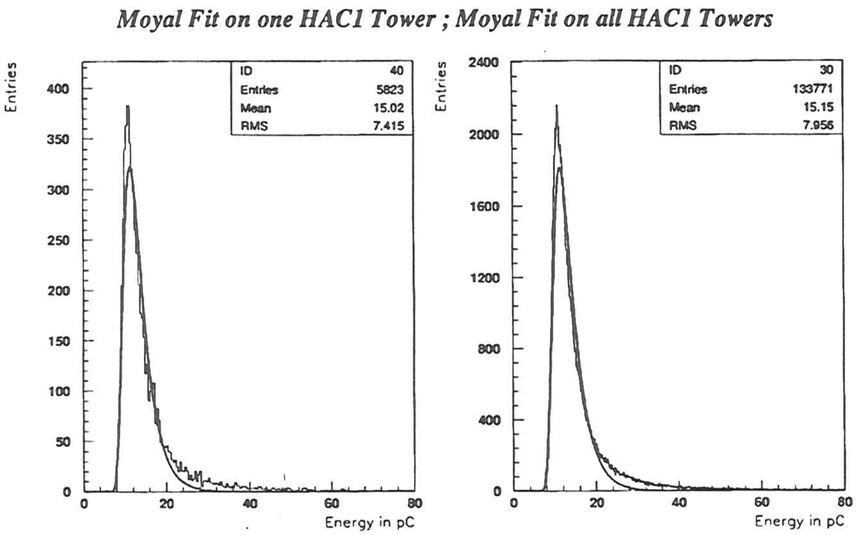

Figure 51: Moyal fit to one HAC1 tower (left) and to all HAC1 towers (right)

7.3 Fitting the Energy Distribution

The function

$$f(Q,\lambda_{max}) = N \cdot \phi\underbrace{\left(\frac{Q - S(\lambda_{max})}{W(\lambda_{max})}\right)}_{\lambda} \tag{28}$$

has been used for the fit with S and W as free parameters. $\phi(\lambda)$ is the Landau density function and Q is the measured charge.
N is known from the number of entries. λ_{max} is the value at which the Landau distribution has been truncated:

$$\lambda_{max} = \frac{Q_{max} - S}{W}\ . \tag{29}$$

As mentioned above in section 6.2.5 a cut at the upper energy has been applied on the muon data to avoid contamination with hadrons. This number has been chosen for Q_{max}

$W = W(\lambda_{max})$	W is proportional to the width of the function. This can be seen in the left plot in figure 52 which shows the function ϕ versus the energy in pC. The figure shows the Landau function with five different values of the parameter W. The values are from the outside to the inside 0.5, 0.75, 1.0, 1.25 and 1.5 (with $N = 10$, $S = 10$).
$S = S(\lambda_{max})$	The variation of this parameter can be seen on the right side of figure 52. The chosen values of S are (from left to right) 5, 7.5, 10, 12.5 and 15 (with $N = 10$, $W = 10$).

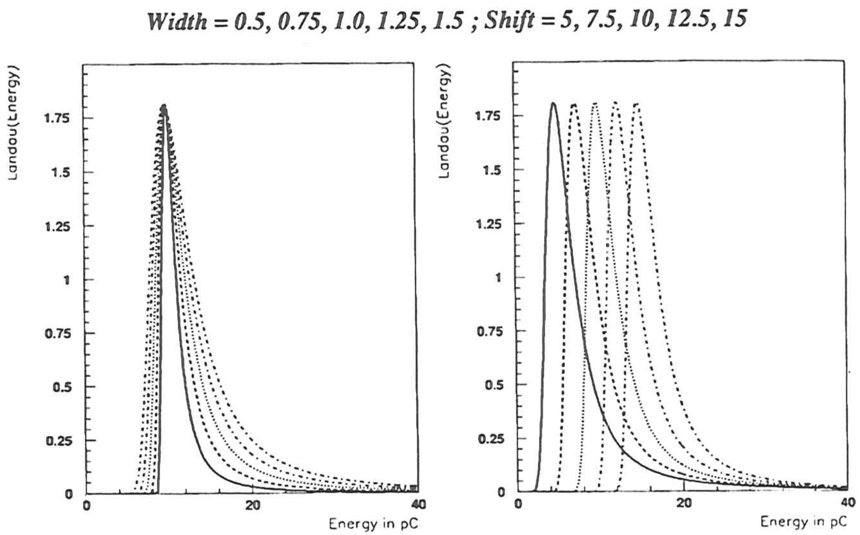

Figure 52: Variation of the parameter W (left) and S (right)

7.4 Estimation of the Mean Values

The first and the second moment of the Landau function are infinite. But the fit of the measured pulse height distribution of Q has been done with a Landau distribution truncated at a value λ_{max} according to equation 29 leading to fitted values W and S. An 'effective mean value' can be derived by the first and the second moment of the Landau function truncated at $\lambda = \lambda_{max}$.

$$\Phi_1(\lambda_{max}) = \frac{1}{\Phi(\lambda_{max})}\int_{-\infty}^{\lambda_{max}} \lambda\phi(\lambda)d\lambda \tag{30}$$

$$\Phi_2(\lambda_{max}) = \frac{1}{\Phi(\lambda_{max})}\int_{-\infty}^{\lambda_{max}} \lambda^2\phi(\lambda)d\lambda \tag{31}$$

with the normalization:

$$\Phi(\lambda_{max}) = \int_{-\infty}^{\lambda_{max}} \phi(\lambda)d\lambda \tag{32}$$

With the use of these definitions the 'effective' mean value $< Q_{\lambda_{max}} >$ and the variance $\sigma^2_{\lambda_{max}}$ of $Q_{\lambda_{max}}$ are given by [KOE84]

$$< Q_{\lambda_{max}} >= W(\lambda_{max})\Phi_1(\lambda_{max}) + S(\lambda_{max}) \tag{33}$$

$$\sigma^2_{\lambda_{max}} = W^2_{\lambda_{max}}\left(\Phi_2(\lambda_{max}) - \Phi_1^2(\lambda_{max})\right) \tag{34}$$

These effective mean and sigma values have been used for the present analysis. They have the advantage over the simple arithmetic mean and sigma of a smaller statistical error and less sensitivity to a hadron contamination of the muon samples and the upper limit.

7.5 Results for the FCAL and RCAL Modules Calibrated at CERN

Tables 10 to 12 show the results of the analysis of the muon data for the six FCAL and the four RCAL modules which have been calibrated at the CERN X5 beam.
The values of $< Q_{\lambda_{max}} >$ have been calculated with Maximum-Likelihood fits (see appendix C) of truncated Landau distributions using equation 33. The values in brackets are the simple arithmetic mean values calculated directly on the data without a fit.
The following quantities appear in the tables in addition to the mean value: σ_M, $< \sigma_S >$ and σ_{IN}. They are defined in the following way:
Denoting by E_i the mean value of the energy deposited in the cell i by M muons calculated either directly on the data or by a fit using equation 33, then $\bar{E}$ is the mean value over all N sections, e.g. at table 11 over all HAC1 sections of a module. With these definitions σ_M is defined as

$$\sigma_M = \sqrt{\frac{\Sigma(E_i - \bar{E})^2}{N-1}} \tag{35}$$

If $\sigma_{LA,i}$ is the variance of the Landau distribution of sections i with M muons given by the fit, then the corresponding statistical error of the mean value is defined as

$$\sigma_{S,i} = \frac{\sigma_{LA,i}}{\sqrt{M}}$$

and the quantity $< \sigma_S >$ is defined as the average value of $\sigma_{S,i}$ for all N sections of a module. The last used quantity σ_{in} is defined by:

$$\sigma_{in}^2 = \sigma_M^2 - < \sigma_S >^2 \tag{36}$$

which is the 'intrinsic error' of the mean value. In other words σ_{in} is the relative cell to cell calibration error which is already corrected by the statistical error of the measurement. A clear improvement of a factor ≈ 2 in σ_M and a factor ≈ 3 in σ_S has been achieved compared to the method without a fit. The Maximum-Likelihood fits with a truncated Landau function for the calibration with beam muons results in similar precision as the electron calibration. The relative cell to cell deviations (σ_{in}) which had been determined after the calibration with the UNO values are in the order of 1%. This value can be compared with the relative cell to cell calibrations for electrons and hadrons which are on the same level as for the muons (shown in table 23 on page 112).

EMC/HAC0 module	100 GeV/c $\bar{E}$ [pC]	$\sigma_M/\bar{E}$ [%]	$< \sigma_S > /\bar{E}$ [%]	$\sigma_{in}/\bar{E}$ [%]
FNL1	4.73 (4.48)	1.3% (2.3%)	0.4% (1.6%)	1.2% (1.6%)
FNL3	4.75 (4.40)	1.4% (1.8%)	0.4% (1.5%)	1.4% (0.9%)
FCD1	4.77 (4.61)	0.9% (2.0%)	0.5% (1.8%)	0.8% (1.1%)
FNL2	4.73 (4.55)	0.8% (2.0%)	0.5% (1.8%)	0.7% (0.8%)
FCD2	4.75 (4.55)	1.1% (2.7%)	0.5% (1.8%)	1.0% (1.8%)
FNL4	4.73 (4.55)	1.1% (2.4%)	0.8% (1.9%)	0.8% (1.5%)
average	4.74 (4.52)	1.1% (2.2%)	0.5% (1.7%)	1.0% (1.3%)
RNL2	4.62 (4.43)	1.1% (2.5%)	0.6% (1.8%)	0.9% (1.7%)
RCD1	4.66 (4.42)	0.8% (1.7%)	0.4% (1.5%)	0.7% (0.8%)
RNL3	4.64 (4.45)	0.9% (1.8%)	0.4% (1.4%)	0.8% (1.1%)
RCD2	4.63 (4.45)	0.9% (1.6%)	0.5% (1.5%)	0.7% (0.6%)
average	4.64 (4.44)	0.9% (1.9%)	0.5% (1.6%)	0.8% (1.0%)

Table 10: Average charge per module in EMC and HAC0 sections calculated by a fit with a truncated Landau function. The values in brackets are the arithmetic mean values.

HAC1 module	100 GeV/c $\bar{E}$ [pC]	$\sigma_M/\bar{E}$ [%]	$< \sigma_S > /\bar{E}$ [%]	$\sigma_{in}/\bar{E}$ [%]
FNL1	15.53 (15.40)	0.4% (1.0%)	0.3% (0.8%)	0.3% (0.4%)
FNL3	15.77 (15.47)	0.5% (0.9%)	0.3% (1.0%)	0.4% (- %)
FCD1	15.57 (15.48)	0.5% (0.9%)	0.2% (0.7%)	0.4% (0.6%)
FNL2	15.44 (15.31)	0.5% (0.8%)	0.2% (0.7%)	0.4% (- %)
FCD2	15.57 (15.46)	0.5% (0.9%)	0.2% (0.7%)	0.5% (0.6%)
FNL4	15.46 (15.33)	0.7% (1.0%)	0.3% (0.7%)	0.6% (0.7%)
average	15.56 (15.41)	0.5% (0.9%)	0.3% (0.8%)	0.4% (0.4%)
RNL2	15.60 (15.77)	0.6% (0.9%)	0.2% (0.6%)	0.6% (0.7%)
RCD1	15.64 (15.76)	0.6% (0.8%)	0.2% (0.7%)	0.6% (0.4%)
RNL3	15.53 (15.66)	0.5% (1.0%)	0.2% (0.6%)	0.4% (0.8%)
RCD2	15.71 (15.87)	0.6% (1.1%)	0.2% (0.9%)	0.6% (0.6%)
average	15.62 (15.77)	0.6% (1.0%)	0.2% (0.7%)	0.6% (0.6%)

Table 11: Average charge per module in the HAC1 sections calculated by a fit with a truncated Landau function. The values in brackets are the arithmetic mean values.

HAC2 module	100 GeV/c $\bar{E}$ [pC]	$\sigma_M/\bar{E}$ [%]	$<\sigma_S>/\bar{E}$ [%]	$\sigma_{in}/\bar{E}$ [%]
FNL1	15.79 (15.72)	0.5% (1.1%)	0.3% (0.8%)	0.4% (0.7%)
FNL3	15.90 (15.64)	0.7% (1.5%)	0.3% (1.0%)	0.6% (1.1%)
FCD1	15.54 (15.44)	0.6% (1.0%)	0.2% (0.7%)	0.6% (0.7%)
FNL2	15.53 (15.43)	0.5% (0.9%)	0.2% (0.7%)	0.4% (0.7%)
FCD2	15.50 (15.36)	0.6% (1.0%)	0.2% (0.7%)	0.5% (0.6%)
FNL4	15.58 (15.52)	0.8% (1.2%)	0.3% (0.7%)	0.8% (0.9%)
average	15.64 (15.52)	0.6% (1.1%)	0.3% (0.8%)	0.6% (0.8%)

Table 12: Average charge per module in the HAC2 sections calculated by a fit with a truncated Landau function. The values in brackets are the arithmetic mean values.

8 Influence of Mechanical Tolerances on the Calorimeter Response

Mechanical tolerances in the construction of the calorimeter introduce differences between the various modules and also result in a non uniform response inside a single module. These effects contribute to the systematic error in the energy measurement and limit the accuracy with which the modules can be calibrated. It is therefore important to understand them and investigations on these tolerances have been done [AND91].

Thickness Fluctuations of the DU-plates ($\Delta(DU)$): The nominal thickness of the DU-plates is 3.3 mm with tolerances of ± 0.15 mm for EMC ±0.20 mm for HAC1 and ±0.25 mm for HAC2. The average thickness of the DU-plates within the tower of a module has been obtained from the measurement of the stackheight and the known spacer thickness.

Thickness Fluctuations of the Scintillator Tiles ($\Delta(SCI)$): The nominal thickness of the scintillator is 2.6 mm. The tolerances of the thickness have been measured to ± 0.1 mm for the EMC sections, ± 0.15 mm for the HAC1 and ± 0.15 mm for the HAC2 section. To minimize the local variations the scintillators have been sorted according to the thickness. As an example a thin scintillator is followed by a thick one.

Thickness Fluctuations of the Cladding Sheets ($\Delta(Fe)$): The nominal thickness of the cladding is 0.2 mm for the EMC sections and 0.4 mm for the HAC sections. A sheet 0.2 mm thick has a thickness tolerance of 10 μm and an uniformity of 0.2 μm. Charts of the measurements are available, but the correlation between a chart and a specific DU-plate cannot be traced anymore.
The influence of these thickness fluctuations on the calorimeter response to the different particles (electrons, hadrons and UNO) can be estimated in the following way [AND91]:
To calculate $\Delta e/e$, the influence of the mechanical tolerances on the electron response, we first express the sampling function e for electrons as function of the response ratio of electrons to minimum ionizing particles.

$$e = \left(\frac{e}{mip}\right) \frac{\epsilon_s s}{\epsilon_s s + \epsilon_u u + \epsilon_c c} \tag{37}$$

where

$\frac{e}{mip}$	is the signal ratio between an electron and a minimal ionizing particle which is approximately independent on the material thicknesses,
$c = 2 \times 0.2mm$	is the nominal thickness of the cladding sheet,
$s = 2.6mm$	is the thickness of a scintillator tile,
$u = 3.3mm$	is the thickness of a DU-plate,
$\epsilon_s = 2.6MeV/cm$	
$\epsilon_u = 20.7MeV/cm$	

relative thickness variation	EMC	HAC
$\Delta s/s$	1.1%	2.4%
$\Delta u/u$	1.9%	2.1%
$\Delta c/c$	1.8%	1.3%

Table 13: Relative thickness variations for the three calorimeter materials for the EMC and the HAC (data from [AND91])

$\epsilon_c = 11.7 MeV/cm$ are the values of the specific energy loss dE/dx by ionization in the scintillator, uranium and the cladding respectively.

The effect of a thickness variation Δs, Δu, Δc in the thickness of the scintillator, uranium and cladding on the electron sampling fraction is then

$$\frac{\Delta e}{e} = f_s^e \frac{\Delta s}{s} + f_u^e \frac{\Delta u}{u} + f_c^e \frac{\Delta c}{c}$$

$$f_s^e = \frac{\delta e}{\delta s} = 0.93$$

$$f_u^e = \frac{\delta e}{\delta u} = -0.87$$

$$f_c^e = \frac{\delta e}{\delta c} = -0.06$$

With many layers and assuming no correlation between the layers the overall error is:

$$\frac{\Delta e}{e} = \sqrt{\left(F_s^e \frac{\Delta s}{s}\right)^2 + \left(F_u^e \frac{\Delta u}{u}\right)^2 + \left(F_c^e \frac{\Delta c}{c}\right)^2}$$

with

$$F_s^e = \sqrt{\sum_i (f_s^e \epsilon_e)^2} \quad \text{etc.}$$

With ϵ_e denoting the fraction of energy deposited by an electron in one layer. The sum is running over all layers of the section (e.g. 26 in the case of an EMC). Table 13 shows the relative values for the thickness variations.

Next we estimate the variation of the response of the calorimeter due to thickness variations for the uranium signal. Therefore a special investigation is required by the UNO signal. Figure 53 shows the dose D from an uranium plate as a function of the thickness of a $CuSn_6$ and a *Lucite* absorber plate. The fit shown in figure 53 uses the parametrization:

$$\frac{dD}{dx} = A * \exp\left(\frac{-x}{a}\right) + B * \exp\left(\frac{-x}{b}\right) \qquad (38)$$

The values of the constants A, B, a, b are given in table 14. To extrapolate the values of $CuSn_6$ to Fe the assumption that a and b scale linearly in dE/dx has been used. The first term of equation 38 describes the short range part due to the β-component and the second term the photon component with a longer range. Integrating equ. 38 over the scintillator

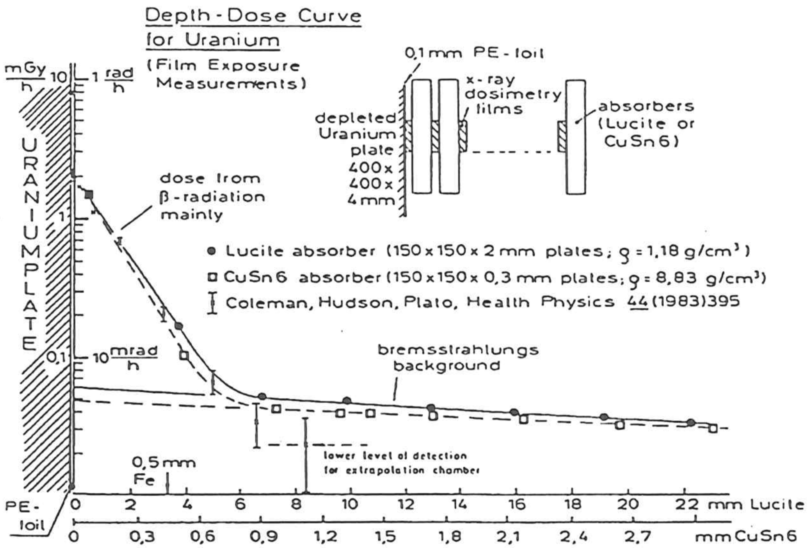

Figure 53: Depth-dose curve determinated by dosimetric film exposure (from [ZEU87])

Absorber	A $[\frac{mGy}{h}]$	B $[\frac{mGy}{h}]$	a [mm]	b [mm]
Lucite	1.94	0.06	1.24	36
$CuSn_6$	1.95	0.05	0.15	5.9
Fe	1.95	0.05	0.17	6.5

Table 14: Material constants for the parametrization of equation 38

thickness s the energy absorbed by the scintillator can be calculated. Thus one gets for the variation ΔUNO of the UNO signal:

$$\frac{\Delta UNO}{UNO} = f_s^{UNO}\frac{\Delta s}{s} + f_c^{UNO}\frac{\Delta c}{c} + f_u^{UNO}\frac{\Delta u}{u}$$

for the EMC sections. Where

$$f_s^{UNO} = \frac{\delta UNO}{\delta s} = 0.4$$

$$f_u^{UNO} = \frac{\delta UNO}{\delta u} = -0.99$$

$$f_c^{UNO} = \frac{\delta UNO}{\delta c} = -0.05$$

Again with many layers assuming no correlation between the layers the overall error is :

$$\frac{\Delta UNO}{UNO} = \sqrt{\left(F_s^{UNO}\frac{\Delta s}{s}\right)^2 + \left(F_c^{UNO}\frac{\Delta c}{c}\right)^2 + \left(F_u^{UNO}\frac{\Delta u}{u}\right)^2}$$

$$F_s^{UNO} = \sqrt{\sum_i (f_s^{UNO}\epsilon_i)^2}$$

The symbol Δ stands for the standard deviation. Thus $\Delta(e/UNO)$ means the standard deviation of the electron signal which has been already normalized by the UNO signal. For the signal ratio e/UNO, again making the assumption that there is no correlation between the layers:

$$\frac{\Delta(e/UNO)}{(e/UNO)} = \sqrt{\left(F_s\frac{\Delta s}{s}\right)^2 + \left(F_c\frac{\Delta c}{c}\right)^2 + \left(F_u\frac{\Delta u}{u}\right)^2}$$

with

$$F_s = \sqrt{\sum_i (f_s^e\epsilon_i - f_s^{UNO}\epsilon_{UNO})^2} \ .$$

The calculations which have been shown for electrons can be done in a similar way for muons and hadrons. Table 15 shows the results for the different signal ratios.

All systematic errors of table 15 are a factor 2-3 below the spread of calibration ratios which have determined during the CERN test for muons (table 10 to 12 on page 74), electrons and hadrons (table 23 page 112). Therefore the systematic effects due to mechanical tolerances do not limit the resolution of the calibration.

In principle it is possible to use the available information of the thickness deviations to correct the calorimeter signals. This has been tried for the thickness of the DU plates in the EMC sections in the FCAL and the RCAL [FAW91]. A correlation between the the DU thickness and the e/UNO ratio had been found. But the deviation of the DU thickness from nominal is only one contribution to the calorimeter signals. Therefore the applied correction reduces the tower to tower spread of the signals e/UNO by only 8%.

Ratio	Section	s	u	c	total
$\Delta(e/UNO)/(e/UNO)$	EMC	0.2%	0.5%	0.3%	0.6%
$\Delta(h/UNO)/(h/UNO)$	EMC	0.1%	0.3%	0.3%	0.4%
	HAC	0.1%	0.2%	0.2%	0.3%
$\Delta(\mu/UNO)/(\mu/UNO)$	EMC	0.1%	0.0%	0.3%	0.3%
	HAC	0.1%	0.0%	0.2%	0.2%

Table 15: Normalized fluctuations of the calibration ratios, $\Delta(e/UNO)$ denoting the standard deviation of the calibration ratios (here for the electron signal)

9 Reconstruction of Deep Inelastic Scattering Parameters

9.1 Introduction

The aim of this chapter is to study the influence of the energy calibration on the reconstruction of the kinematic variables in ep-scattering. First, the definition of the structure functions and the kinematic variables are given. Then different methods to determine the kinematic variables are determined from the measured energies and angles are shown. Next the influence of limited energy resolution, bending of charged particles in the magnetic field and material in front of of the calorimeter will be investigated. This determines the precision with which the DIS variables describing deep inelastic scattering can be reconstructed for a perfectly calibrated detector. Finally the influence of the uncertainty of the energy calibration will be studied.

9.2 Determination of Structure Functions

9.2.1 Elastic Electron Proton Scattering

With elastic ep-scattering the size of the proton has been determined. The cross-section of a spin 1/2 particle in the Coulomb field of a massive spinless target is given by the Mott cross-section. For the scattering of an extended spin 1/2 proton the cross-section is modified by introducing the form factors G_E and G_M, which depend only on the squared momentum transfer q^2 [LOH81]:

$$\left.\frac{d\sigma}{d\Omega}\right|_{Rosenbluth} = \left.\frac{d\sigma}{d\Omega}\right|_{p} \cdot \left[\frac{G_E^2(q^2) + \tau G_M^2(q^2)}{1+\tau} + 2 \cdot \tau \cdot G_M^2(q^2) tan^2\frac{\theta_e}{2}\right] \tag{39}$$

$$\left.\frac{d\sigma}{d\Omega}\right|_{p} = \frac{r_e^2 \cdot m_e^2}{4E_e'^2} \cdot \frac{cos^2\theta_e/2}{sin^4\theta_e/2} \cdot \frac{1}{1 + \frac{2E_e'}{M_p} \cdot sin^2\theta/2}$$

$$\tau = \frac{|q^2|}{4M_p^2} \quad q^2 = -\frac{4E_e'^2 \cdot sin^2\theta_e/2}{1 + \frac{2E_e'}{M_p} \cdot sin^2\theta_e/2}$$

with

E_e', θ_e = energy and angle of the scattered electron

$d\sigma/d\Omega|_p$ = cross-section of a spin 1/2 particle in the Coulomb field of a spinless target

M_p, m_e = mass of proton and electron

The electromagnetic form factor G_E is determined by the charge distribution inside the proton and G_M, the magnetic form factor, is related to the magnetic moment of the nucleon. From the Fourier analysis of the form factor G_E one obtains a value for the mean square radius of the proton.

$$< r^2 >= 6 \left(\frac{dG_E(q^2)}{dq^2}\right)_{q^2=0} = \left(0.81 \cdot 10^{-13} cm\right)^2 \tag{40}$$

These two form factors G_E and G_M, can be expressed in terms of two structure functions F_1 and F_2 which play a key role in deep inelastic scattering:

$$G_E = F_1 + \kappa q^2/4M_p^2 * F_2 \quad and \quad G_M = F_1 + \kappa * F_2$$

κ is the anomalous magnetic moment of the proton.

9.3 Deep Inelastic Scattering Cross Sections

In the Quark Parton Model (QPM) e-p scattering is described as the incoherent sum of elastic scattering off the quarks. The structure function F_2 has a simple interpretation:

$$F_2 = x \sum_i e_i^2 * q_i(x) ,$$

where e_i is the quark charge and $q_i(x)$ is the probability distribution of the quark of flavour i carrying the fractional momentum x of the proton. Depending on the outgoing lepton one distinguish

$$\text{neutral current (NC)} : e\ p \to e'\ X$$

and

$$\text{charged current (CC)} : e\ p \to \nu\ X$$

inelastic scattering. Where e is the incoming electron, p the incoming proton, e' the outgoing electron, ν the outgoing neutrino and X the system of the hadronic final state particles. In a NC reaction a photon or a boson (Z^0) is exchanged between the electron and the proton. With the known momenta of the incoming particles, the kinematics of the reaction is described by two independent variables.
In the laboratory system it is convenient to use the energy and the angle of the outgoing lepton. In the ZEUS detector the neutrino of the CC reactions cannot be measured. NC reactions where the outgoing lepton is an electron (E_e', θ_e) will be described first. P_e and P_p denote the four momentum vectors of the incoming electron and proton and P_e' is the momentum of the scattered electron. The four momentum transfer Q^2 is given by:

$$Q^2 \equiv -q^2 = -(P_e - P_e')^2 \simeq 2E_e E_e'(1 + \cos\theta_e)$$

The angle measured relative to the direction of the incoming proton. E_e and E_e' are the energies of the incoming and scattered electron. The sign $\simeq$ is used here to indicate that lepton masses are neglected. In this notation the center of mass energy squared is given by

$$s \equiv (P_e + P_p)^2 \simeq 4E_e E_p.$$

with E_p as the energy of the incoming proton. For the energy transfer the variable

$$\nu = \frac{P_p q}{M_p}$$

is used. In the rest frame of the target proton ν is the energy of the lepton transfered to the target:

$$\nu = E_e - E_e'$$

Commonly the kinematics is described by the dimensionless Bjorken scaling variables x and y [BJO69].

$$x \equiv \frac{Q^2}{2P_pq} = \frac{Q^2}{2M_p\nu} \simeq \frac{E_e^{'} \cos^2 \frac{\theta_e}{2}}{E_p(1 - \left(\frac{E_e^{'}}{E_e}\right) \sin^2 \frac{\theta_e}{2})}$$

$$y \equiv \frac{P_pq}{P_pp_e} = \frac{2P_pq}{s} = \frac{\nu}{\nu_{max}} \simeq 1 - \left(\frac{E_e^{'}}{E_e}\right) \sin^2 \frac{\theta_e}{2}$$

Thus y is the normalized energy loss of the scattered lepton in the laboratory sytem because ν_{max} is the energy of the incident electron. With the assumption that each quark carries a certain fraction ξ of the 4-momentum of the proton, the initial and the final momentum of the quark can be written as

$$p_i = \xi P_p \text{ and } p_f = \xi P_p + q$$

With the assumption of massless quarks

$$p_i^2 = 0 \text{ and } p_f^2 = 0$$

one obtains

$$\begin{aligned} p_f^2 &= (p_i + q)^2 \\ &= p_i^2 + 2p_iq + q^2 \\ &= 2P\xi q - Q^2 \\ &\Rightarrow \\ \xi &= \frac{Q^2}{2Pq} \equiv x = \frac{Q^2}{ys} \end{aligned}$$

Thus in the frame work of the QPM x can be interpreted as the momentum fraction of the proton carried by the struck quark.

9.3.1 Determination of Structure Functions

The cross section for unpolarized electrons/positrons of the neutral current reaction is given by [ING87]

$$\frac{d^2\sigma_{NC}(e^{\mp})}{dxdQ^2} = \frac{4\pi\alpha^2}{xQ^4}\left[y^2xF_1(x,Q^2) + (1-y)F_2(x,Q^2) \pm \left(y - \frac{y^2}{2}\right)xF_3(x,Q^2)\right] \tag{41}$$

F_1 and F_2 are the structure functions for the electromagnetic interaction as discussed above and α the fine structure constant. F_3 contains the parity violation part of the cross-section in case of a Z^0- exchange. In the QPM the structure functions are linear combinations of the quark momentum distribution functions. The Callan-Gross relation,

$$2xF_1 = F_2, \tag{42}$$

is approximately satisfied except for very low x. Measuring the cross-sections as a function of x and Q^2 allows a determination of the structure functions. From the structure function the momentum distribution of individual quark flavors can be extracted by an unfolding procedure using the QPM (e.g. [ING89b]).

The cross section for the charged current reaction is given in the QPM by:

$$\frac{d^2\sigma_{CC}(e^-p)}{dxdQ^2} = \frac{(1-\lambda)\pi\alpha^2}{4\sin^4\theta_W(Q^2+M_W^2)^2}\sum_{i,j}\left[\left|V_{u_i,d_j}\right|^2 u_i(x,Q^2) + (1-y)^2\left|V_{u_j,d_i}\right|^2 \bar{d}_i(x,Q^2)\right] \tag{43}$$

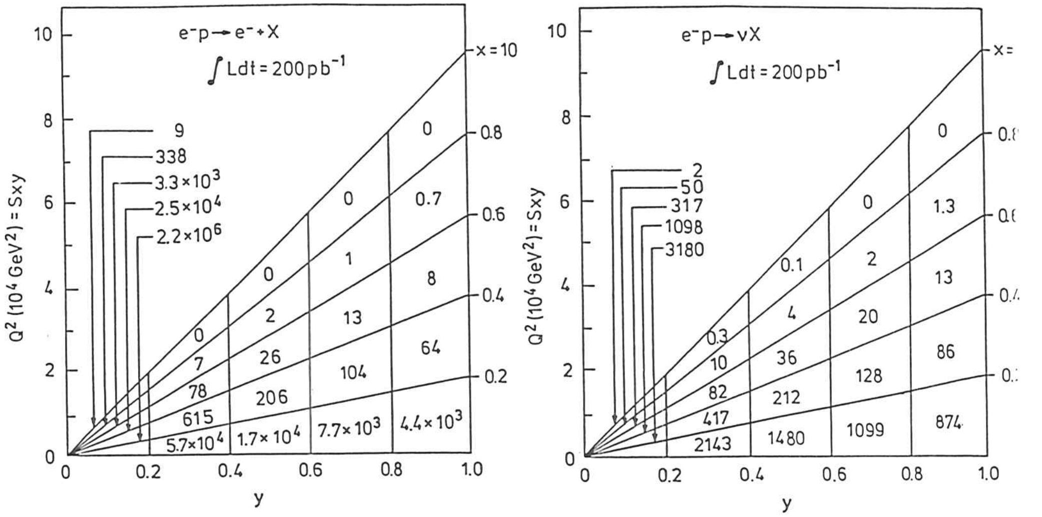

Figure 54: Event rates of Neutral and Charged Current Reactions at HERA

with

λ : $e^{\pm}$ beam polarization (±1 for right/left handed state)

θ_W : Weinberg angle

M_W : mass of the W boson

$u_i(x, Q^2)$: up quark density with the family index i

$\bar{d}_i$: corresponding anti-down quark

V_{u_i,d_j} : element of the Kobayashi-Maskawa matrix

Compared to NC reactions, the cross section of the CC reactions is smaller (see figure 54). The propagator for NC reactions with γ exchange is $1/Q^2$ whereas it is $1/(Q^2 + M_W^2)$ for CC reactions. The two cross-sections become comparable when the momentum transfer reaches the mass of the W-boson ($Q^2 \sim M_W^2$).

9.4 Reconstruction Methods for DIS Variables

Reconstruction methods for the DIS variables (x, y and Q^2) will here be presented for NC reactions.

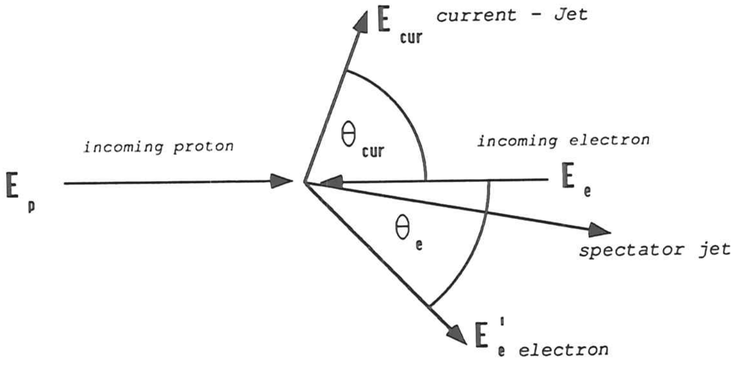

Figure 55: Definition of the variables for NC reaction

9.4.1 Topology of NC-Reactions

Figure 55 defines the energy and angle variables. Figure 56 shows the energy of the current jet, the spectator jet and the electron for 1000 events generated with the Bjorken variables $x = 0.2$ and $y = 0.8$. The angle θ is measured versus the direction of the incoming proton. No radiative corrections have been introduced.
The events have been produced with the Lund event generator LEPTO V5.2 [ING89a] with 1st order QCD and the standard set of parameters (see appendix B). For these values of x and y the angle of the electron is $\theta_e = 24.14^O$. Particles with $\theta < \theta_e$ have been grouped to the spectator jet and particles with $\theta > \theta_e$ have been grouped to the current jet. Energies and angles have been calculated using equation 44 of the next section where an angle weighted by the energy is calculated. Thus each event corresponds to three entries in the plot of figure 56, one for the spectator jet, one for the current jet and one for the scattered electron. The calorimeter covers polar angles $\theta > 4^0$. Therefore all particles which leave the interaction point with $\theta < 4^0$ are lost in the beampipe or are at least not properly detected. Figure 56 shows that this is the case for the spectator jets which therefore cannot be used for the reconstruction.

9.4.2 Reconstruction Using the Electron and the Current Jet

One method uses energy and polar angle θ of the electron, the second energy and polar angle of the current jet. These quantities have to be calculated from the tracks and deposited energies measured by the tracking system and the calorimeter. In the present study only the energies deposited in the calorimeter will be used.

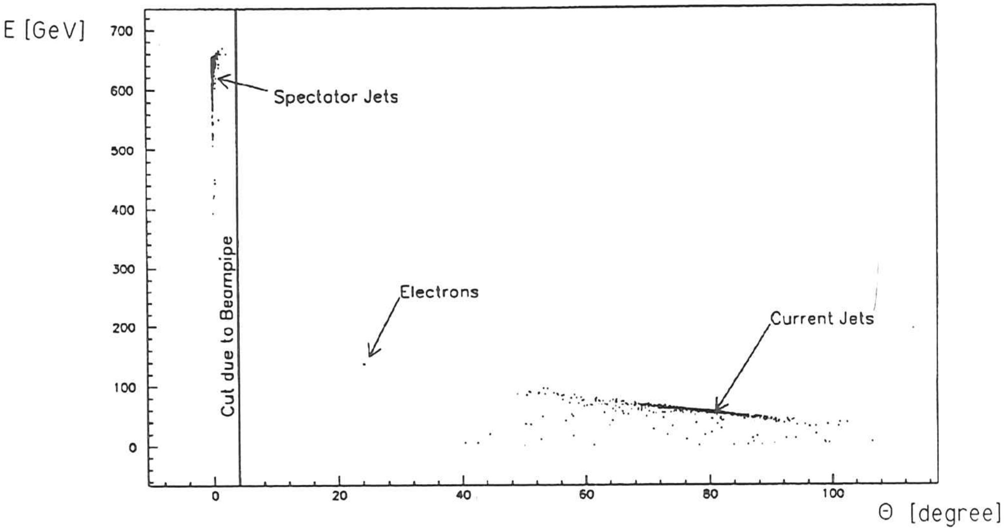

Figure 56: Energy versus polar angle for NC-events with $x = 0.2, y = 0.8$. The current jet, spectator jet and the electron is shown for each event. Particles which leave the vertex under an angle $\theta < 4^0$ are lost in the beampipe.

Using the Electron Two obvious methods exist to find the cell or the calorimeter cells in which the electron has deposited its energy. If the direction of the electron is known (e.g. from the tracking system), the cells can directly found. If the angle of the electron is not known one can use a cluster finding algorithm. It requires most of the energy deposited in one or a few EMC cells and nearly no energy in the HAC cells of the same tower. Using the energies (E_i) and the angles of the cells related to the electron, the energy and the angle of the electron coming from the interaction point can be calculated as

$$E'_e = \sum E_i \quad , \quad \theta_e = \frac{\sum E_i\theta_i}{\sum E_i} \quad , \quad \phi_e = \frac{\sum E_i\phi_i}{\sum E_i} \tag{44}$$

With θ_e relative to the direction of the incoming proton, the DIS variables can be calculated as

$$\begin{aligned} x &= \frac{E'_e \cos^2 \frac{\theta_e}{2}}{E_p(1 - \left(\frac{E'_e}{E_e}\right) \sin^2 \frac{\theta_e}{2})} \\ y &= 1 - \left(\frac{E'_e}{E_e}\right) \sin^2 \frac{\theta_e}{2} \\ Q^2 &= 2E_eE'_e(1 + \cos\theta_e) \end{aligned} \tag{45}$$

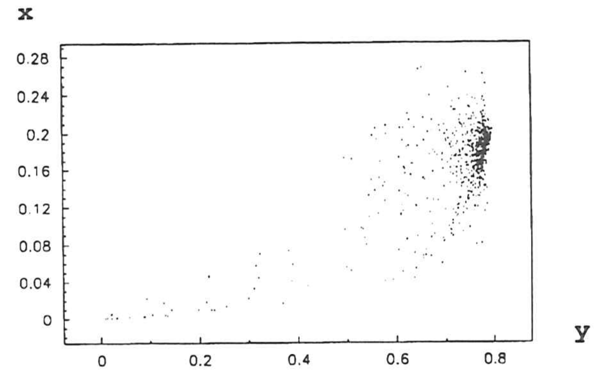

Figure 57: x versus y reconstructed from the current jet (equation 46) using event generator data with x=0.2, y=0.8

Using the Current Jet The angle of the current jet cannot be derived by the tracking system alone because one jet is made from several tracks. Therefore a cluster finding algorithm has to be used to determine the energy and the angle charged and neutral particles of the jet from the energy deposit in the calorimeter. A cluster is an area of connected cells in which an energy above a certain threshold has been deposited. The cluster finding algorithm searches through all calorimeter cells to find such groups. After the group of cells has been determined the energy (E_{cur}) and the angle (θ_{cur}, ϕ_{cur}) of the jet can be determined like in equation 44 for the electron. Then the DIS variables are given by

$$x = \frac{Q^2}{sy} = \frac{E_{cur}\cos^2\frac{\theta_{cur}}{2}}{E_p\left(1-\left(\frac{E_{cur}}{E_e}\right)\sin^2\frac{\theta_{cur}}{2}\right)}$$

$$y = \frac{E_{cur}}{2E_e}(1-\cos\theta_{cur}) = \frac{E_{cur}}{E_e}\sin^2\frac{\theta_{cur}}{2} \qquad (46)$$

$$Q^2 = \frac{E_{cur}^2\sin^2\theta_{cur}}{1-\frac{E_{cur}}{2E_e}(1-\cos\theta_{cur})}$$

Equation 46 is an approximation for zero jet mass; it does not take the production of gluons into account. Figure 56 shows that for events with fixed kinematic variables the current jets show a big spread in energy and especially angle whereas the electron always has the same energy and angle. Therefore the reconstructed values for x,y of figure 57 which have been calculated with the energies and angles of the current jet of figure 57 show a similar spread. The detector introduces further problems for the reconstruction. The current jet deposits its energy in far more cells than the electron and shows big longitudinal and transversal fluctuations. Therefore the identification of the current jet is much more complicated than the identification of an electron.
Up to here only the reconstruction method using the electron turned out to be precise. A different approach is used by the method of Jacquet and Blondel.

9.4.3 Reconstruction With the Method of Jacquet and Blondel

The method of Jacquet and Blondel [BLO79] uses the information of all detected particles apart from the lepton. It uses energy and momentum conservation and minimizes the influence of particles lost in the beampipe. The equations are:

$$y = \frac{\sum_i (E_i - p_{z,i})}{2E_e}$$

$$Q^2 = \frac{\left(\sum_i p_{T,i}\right)^2}{1-y} \qquad (47)$$

$$x = \frac{Q^2}{sy}$$

with:

E_i : energy of the particle i,

$p_{z,i}$: momentum component of the particle i parallel to the proton direction,

$p_{T,i}$: momentum component of the particle i transverse to the proton direction,

$\sum_i$: sum is over all particles except the electron.

For Monte Carlo data, the particle energies,momenta and angles can be used, whereas for detector data the energies deposited in the calorimeter cell i have to be used. Like the method based on the electron variables, the method of Jacquet and Blondel turns out to be precise. At ZEUS all particles which leave the vertex under a polar angle of $\theta < 4^0$ are lost for the reconstruction due to the beampipe. Figure 58 shows the reconstructed values for x and y if these particles are not used for the calculation. The result is satisfactory and shows that the beam pipe cut has not a major influence. The deviation from the mean values of x is 0.8 % and for y 0.1 %. The spread of x is 3 % and 0.1 % for y. The comparison between figure 57 and 58 shows that the errors introduced by the method of Jacquet and Blondel are at least a factor 10 smaller than the errors introduced by the method using the current jet. Thus only this method and the method based on the electron variables will be used for the further studies.

9.5 Influence of the Detector on the $x-y$ Reconstruction

The influence of effects due to the detector resolution, material in front of the calorimeter and the magnetic field will be investigated next.

9.5.1 Introduction

To investigate the reconstruction of the DIS variables with both reconstruction methods in different kinematic regions, NC event samples were produced with the LEPTO V5.2 generator for a number of fixed values of x and Q^2. Figure 59 gives an overview of the chosen samples of x and y. Nine different kinematical points in the $x-Q^2$ plane have been investigated. All these event samples show similarly small errors as these of the sample with $x=0.2, y=0.8$. These regions are marked by dots in figure 59. More detailed investigations were done on

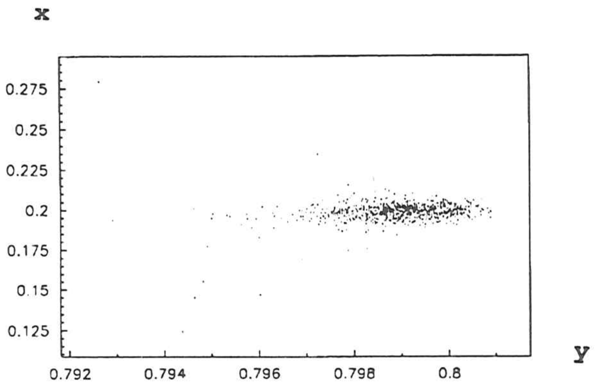

Figure 58: x versus y reconstructed by the method of Jacquet Blondel (equation 47) using event generator data with x=0.2, y=0.8

Parameter	x=0.2, y=0.8	x=0.001, y=0.8	x=0.2, y=0.3
θ of current jet	81.09^0	170.55^0	31.28^0
current jet energy [GeV]	56.8	24.82	123.8
current jet into	BCAL	RCAL	FCAL
θ of e^-	24.14^0	143.41^0	66.31^0
e^- energy [GeV]	137.2	6.656	70.2
e^- into	FCAL	RCAL	BCAL

Table 16: Parameters of the event samples at the three selected kinematic regions

three representative event samples which are indicated in figure 59 by crosses. The parameters of these samples are listed in table 16. The three event samples are chosen, because electron and current jet are covering all three parts of the calorimeter, front, barrel and rear, and so test the performance of all parts of the calorimeter.
The investigations have been started on the event generator level with a perfect resolution for the energy and angle but already introducing beampipe losses for angles $\theta < 4^0$. Step by step more realism is then introduced into the simulations. First, the event generator data is smeared with the Gaussian shaped energy resolution of the calorimeter. Then a detector Monte Carlo without the magnetic field and dead material in front of the calorimeter is used. Subsequently without and with the magnetic field the material in front of the calorimeter is introduced. A summary of the results is presented at the end of this section.
In the analysis mistakes in the Monte Carlo have been found - such events have been removed by cuts (see section A.2). A further cut on the leakage through the back of the calorimeter has been applied requiring that less than 10 % of the entire energy is deposited in the HAC2 sections.

The data have been generated with the use of the ZEUS offline software system (see section A.1) and the plots have been produced using PAW[7]. The plots shown in figures 60 to 69 consist of 3 rows with two histograms. The three rows correspond to the three kinematical regions. The top row shows the distribution of x and y reconstructed according to the Jacquet and Blondel method $x = 0.2, y = 0.8$. The middle row shows the distributions for $x = 0.001, y = 0.8$ and the bottom row for $x = 0.2, y = 0.3$. The distributions for x are in the left column and those for y in the right column. All distributions were fitted with a Gauss function. The two inserts at the right upper corner of each plot show the following data:
upper box:

ID : an arbitrary identifier for the histogram required by PAW

Entries : the number of entries in the histogram

Mean : mean value calculated over all the bins

RMS : root mean square calculated over all the bins

The lower box contains the results of the fit:

χ^2 : χ^2/NDF-value of the fit

Constant : value of the maximum of the Gauss function.

Mean : mean value of the fitted Gaussian.

Sigma : standard deviation sigma of the fitted Gaussian.

9.5.2 Results

Effect of Beam Pipe: The plain event generator data except for a cut ($\theta < 4^0$) which simulates the beampipe loss have been used for this study. The results for the reconstruction method using the electron are not shown because they have no error.
Figure 60 and table 17 show the results for the method of Jacquet and Blondel. The deviations of the reconstructed mean value from the true value are small (< 1%) except for the x value of the low x event sample (x=0.001,y=0.8), where the deviation of the calculated mean value is 2.4% and 1.2% for the fitted mean value. The deviations for y are always very small ($\sim$ 0.1%). The relative width ($Sigma/Mean$) is of the order of 1-2% for x and less than 0.3% for y except for the low x event samples where the relative width is 23%.
Already at this level some tails can be seen for the reconstructed values of x. About 1% of the reconstructed x values deviate up to 30% off from the generated value.

Effect of the Energy Resolution: For this study the energy of the particles have been smeared with a Gaussian distribution with a standard deviation given by

$$\frac{\sigma}{E} = \frac{20\%}{\sqrt{E}}$$

---

[7] Physics Analysis Workstation - a data analysis and presentation tool developed at CERN [BRU89]

Method:	Jacquet-Blondel			
Parameter:	$\Delta x/\bar{x}$	$\sigma_x/\bar{x}$	$\Delta y/\bar{y}$	$\sigma_y/\bar{y}$
$x = 0.2$ & $y = 0.8$	0.8 %	3.2 %	0.1 %	0.1 %
$x = 0.001$ & $y = 0.8$	2.4 %	26.5 %	0.2 %	0.1 %
$x = 0.2$ & $y = 0.3$	0.5 %	3.1 %	0.3 %	0.3 %

Table 17: Mean deviations and spread of the reconstructed values of x and y from the generated values for data with a beampipe cut

Method:	Electron				Jacquet-Blondel			
Parameter:	$\Delta x/\bar{x}$	$\sigma_x/\bar{x}$	$\Delta y/\bar{y}$	$\sigma_y/\bar{y}$	$\Delta x/\bar{x}$	$\sigma_x/\bar{x}$	$\Delta y/\bar{y}$	$\sigma_y/\bar{y}$
$x = 0.2$ & $y = 0.8$	0.1 %	2.1 %	0.1 %	0.4 %	3.6 %	26.2 %	0.4 %	4.6
$x = 0.001$ & $y = 0.8$	0.6 %	9.6 %	0.1 %	1.9 %	17.4 %	65.2 %	0.3 %	6.5
$x = 0.2$ & $y = 0.3$	0.4 %	8.0 %	0.1 %	5.5 %	0.1 %	5.5 %	1.1 %	3.2

Table 18: Mean deviations and spread of the reconstructed values of x and y from the generated values for data with a beampipe cut

for the electrons and

$$\frac{\sigma}{E} = \frac{35\%}{\sqrt{E}}, \quad \text{E in GeV},$$

for the hadrons. Figure 61 shows the results for the method which uses the electron. The mean values are reconstructed very well. The deviations in all cases are less than 0.6%. The relative width ($Sigma/Mean$) is 0.5% for y of the sample in the upper row (x=0.2,y=0.8) and 10% for the x of the low x sample (x=0.001,y=0.8). There are no long tails.

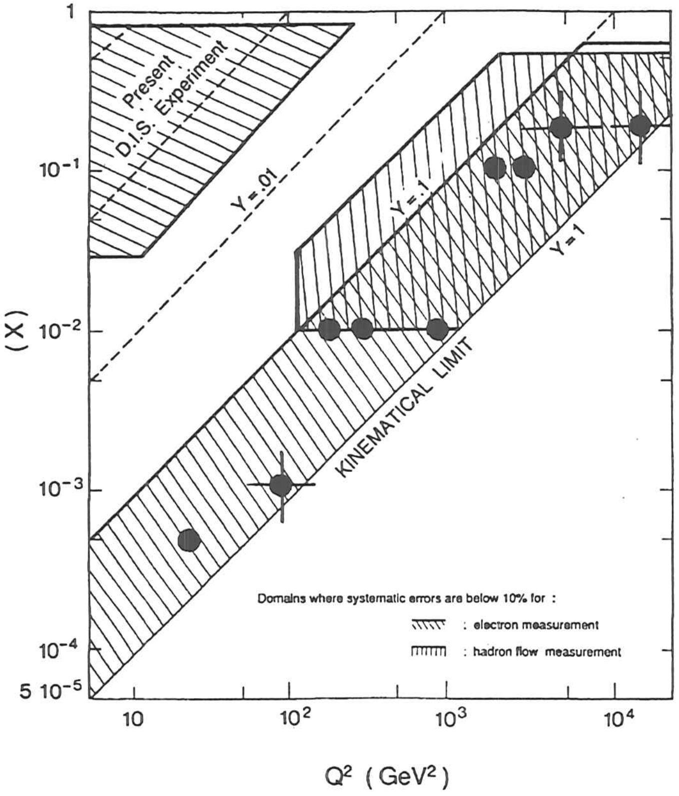

Figure 59: Accessible $x - Q^2$ plane of HERA [FEL87]. The dots indicate x and Q^2 of the nine event samples investigated. The crosses indicate the kinematic points chosen for a more detailed investigation.

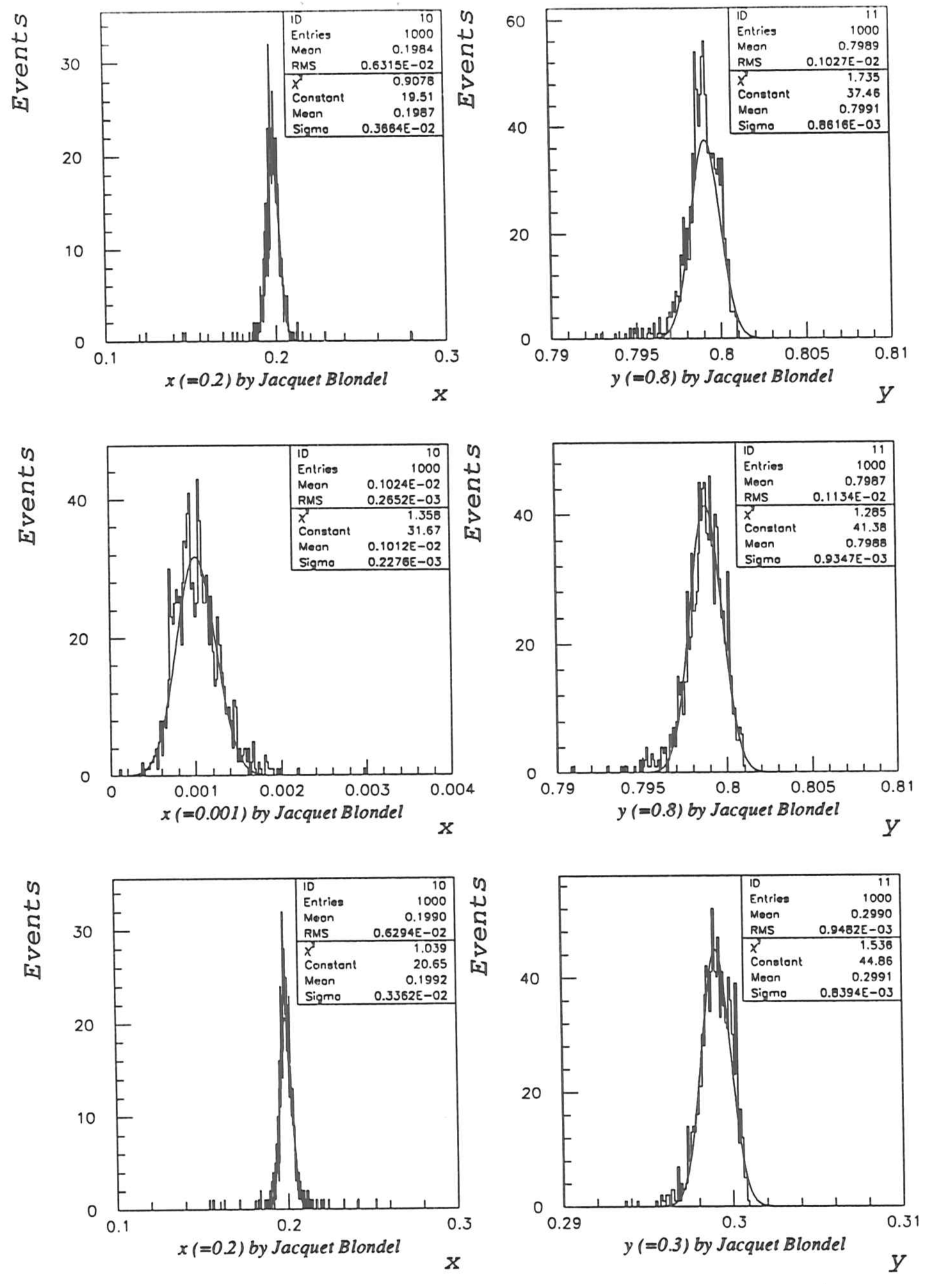

Figure 60: x and y reconstructed with the method of Jacquet and Blondel. The event generator data with a beampipe cut have been used.

Figure 62 shows the results using the method of Jacquet and Blondel. Table 18 lists the deviations of the mean values and the relative widths for both methods. Compared to the reconstructed values of the unsmeared data of figure 60 the deviations are only slightly larger. The relative width ($Sigma/Mean$) is of the order of 4-5% for x and y. However, for the low x event sample ($x = 0.001$, $y = 0.8$) the relative error is $\approx 80\%$ which indicates the limit for the reconstruction of low x events.

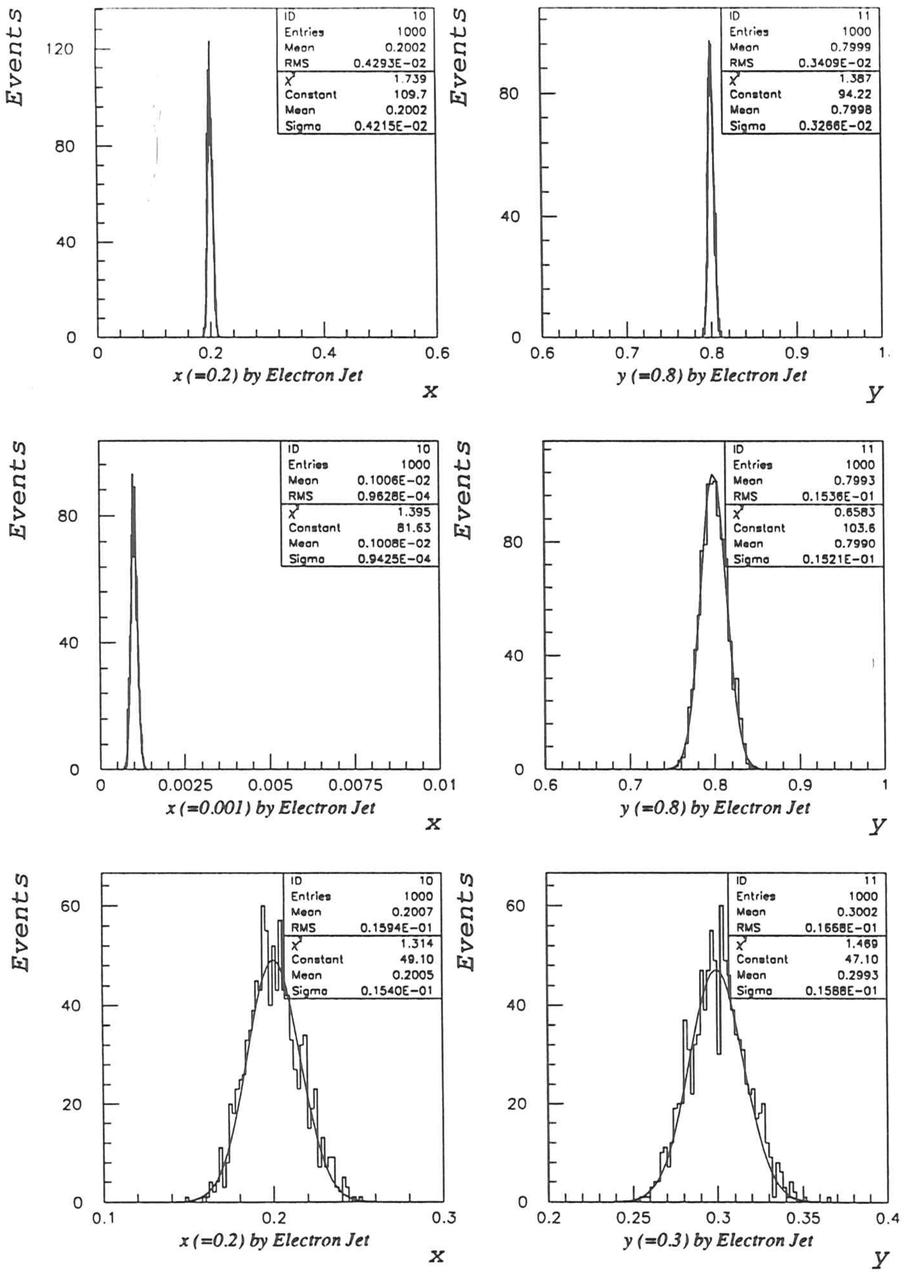

Figure 61: x and y reconstructed with the electron. The event generator data have been smeared with a resolution of $20\%/\sqrt{E}$.

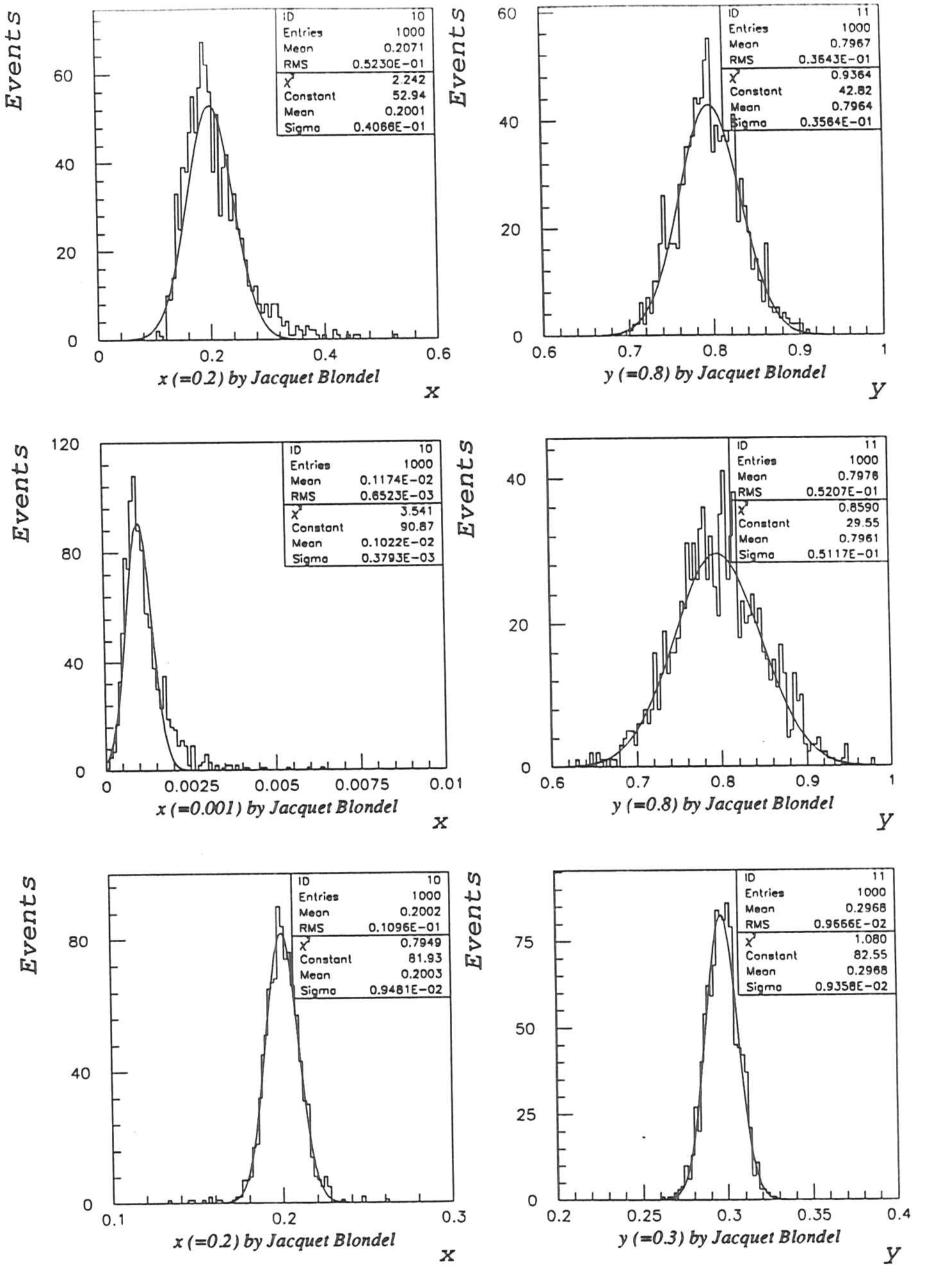

Figure 62: x and y reconstructed with the method of Jacquet and Blondel. The event generator data have been smeared with a resolution of $35\%/\sqrt{E}$.

Method:	Electron				Jacquet-Blondel			
Parameter:	$\Delta x/\bar{x}$	$\sigma_x/\bar{x}$	$\Delta y/\bar{y}$	$\sigma_y/\bar{y}$	$\Delta x/\bar{x}$	$\sigma_x/\bar{x}$	$\Delta y/\bar{y}$	$\sigma_y/\bar{y}$
$x = 0.2$ & $y = 0.8$	0.5 %	2.3 %	0.0 %	1.2 %	4.9 %	34.5 %	0.2 %	6.4
$x = 0.001$ & $y = 0.8$	7.4 %	10.6 %	1.0 %	2.2 %	15.6 %	51.0 %	6.0 %	9.5
$x = 0.2$ & $y = 0.3$	1.9 %	6.9 %	1.4 %	5.8 %	6.2 %	6.8 %	0.3 %	5.0

Table 19: Mean deviations and spread of the reconstructed values of x and y from the generated values for data with no material in front of the calorimeter and the magnetic field switched off

Effects of the Position and Energy Reconstruction in the Calorimeter For this study the individual particles have been propagated through the calorimeter and energy and angle reconstructed from the simulated energy deposits. This introduces several new effects. First, there is now a finite angular resolution of the angle. The energy resolution and especially the energy scale may lead to further differences. During this work errors in the calorimeter Monte Carlo have been detected leading to corrupted events which have been rejected via cuts (see section A.2).

With the method based on the electron (figure 63) the difference between the true and the reconstructed mean values is of the order of 1% or less. Only the mean value x of the events with $x = 0.001, y = 0.8$ differs about 8 % from the true value. The relative widths ($Sigma/Mean$) are of the same order as the smeared event generator data (figure 61) and there are no long tails in the distributions.

Figure 64 shows the results for the Monte Carlo study with the method of Jacquet and Blondel. In the Monte Carlo study the deviations of the reconstructed mean values from the true mean values are larger. This is due to the energy calibration which is still not perfect.

Effects of the Magnetic Field : In this step the magnetic field has been switched on. The method which uses the electron (equation 45) and the method of Jacquet and Blondel (equation 47) require the knowledge of the particle angles at the interaction point. Taking the direction from the interaction vertex to the cluster positions in the calorimeter is an approximation. The effect is negligible for the reconstruction with the electron. All deviations between the reconstruction without magnetic field (figure 63) and with magnetic field (figure 65) are of the order of 0.1% (see table 20).

For the method of Jacquet and Blondel the effect is bigger. Here the biggest variations are some percent (figure 66).

Effects of Material in Front of the Calorimeter: For a realistic study the material in front of the calorimeter has been inserted. Figure 67 shows its thickness (in radiation lengths) versus the polar angle θ.

Again the effects for the reconstruction with the electron (figure 68) are less than 1% except for the x of the events with $x = 0.001, y = 0.8$ where the deviation between the reconstructed and the true mean value is ≈3% (see table 21). A significant change in the relative width of the distribution cannot be seen.

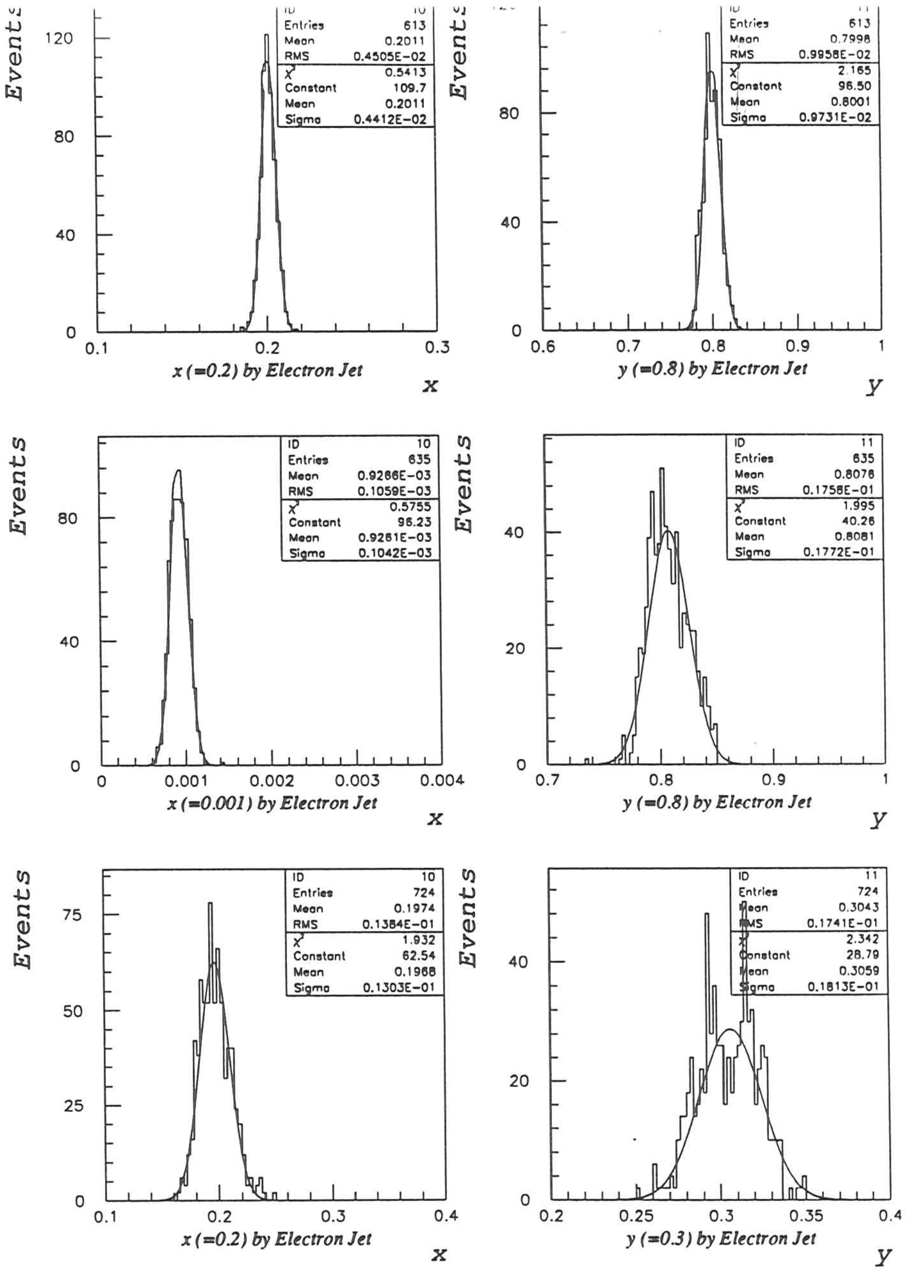

Figure 63: x and y reconstructed from the electron produced with the ZEUS Monte Carlo. The magnetic field is switched off and there is no material in front of the calorimeter.

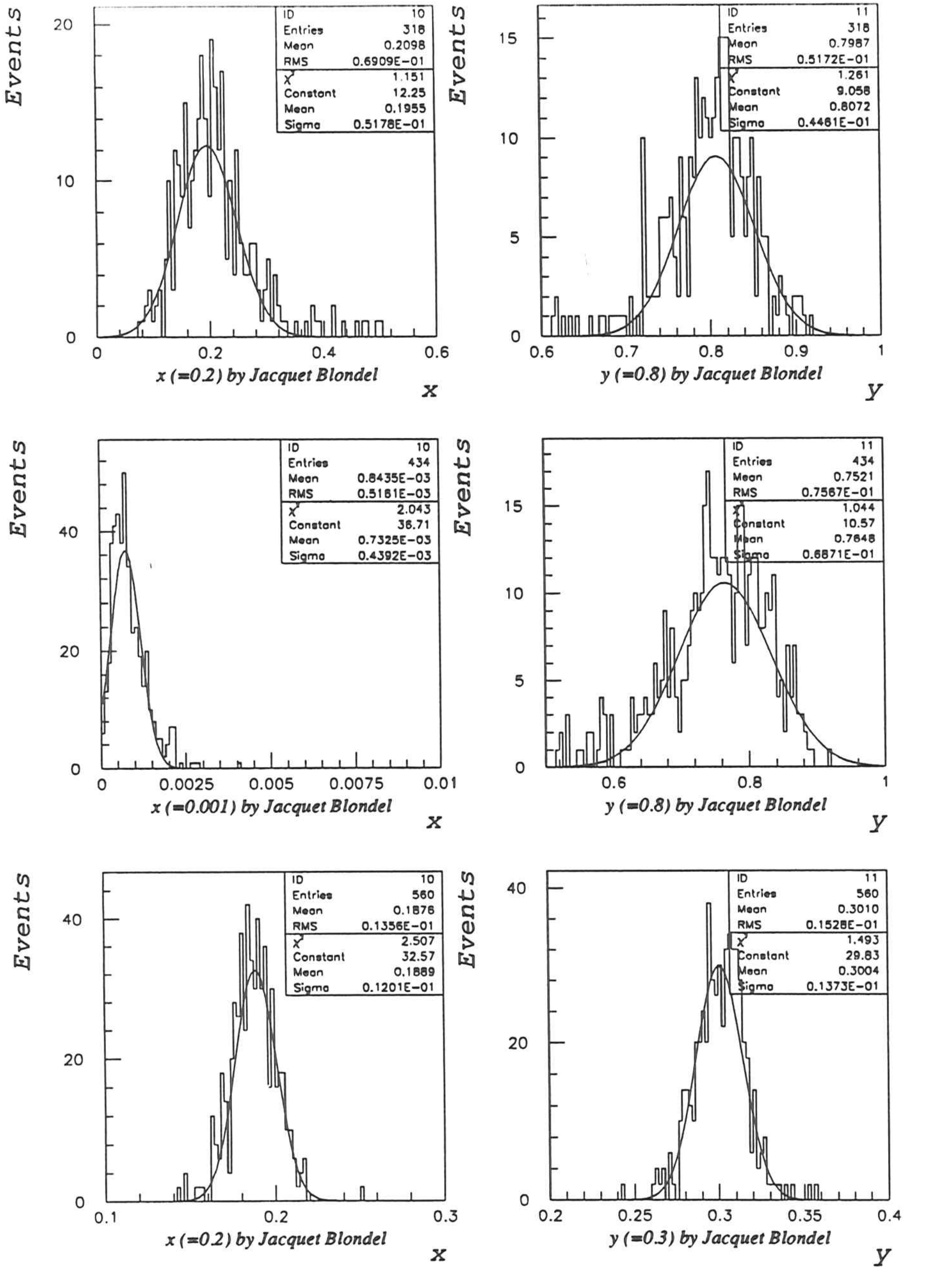

Figure 64: x and y reconstructed with the method of Jacquet and Blondel of events produced with the ZEUS Monte Carlo. The magnetic field is switched off and there is no material in front of the calorimeter.

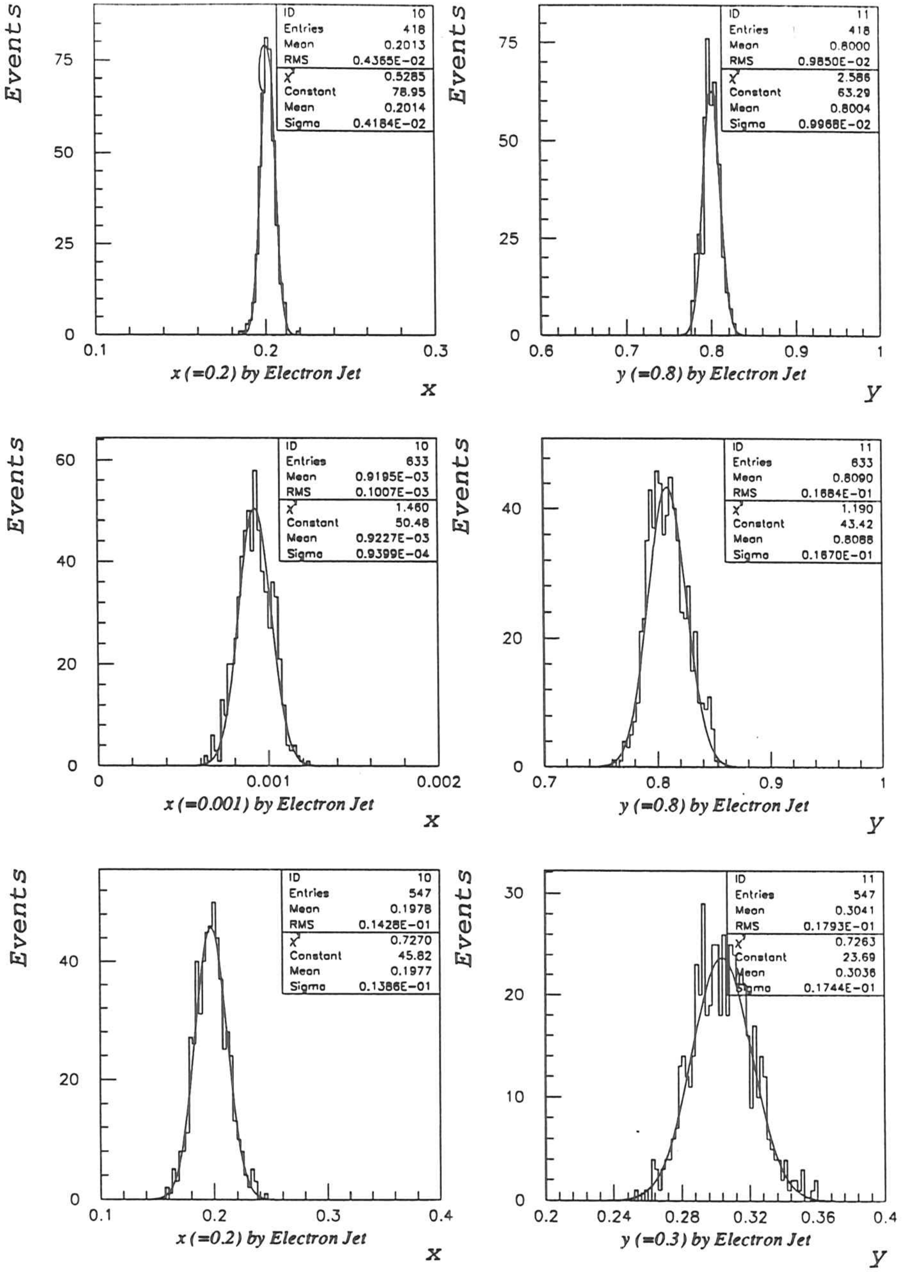

Figure 65: x and y reconstructed with the electron of events produced with the ZEUS Monte Carlo. The magnetic field is switched on and there is no material in front of the calorimeter.

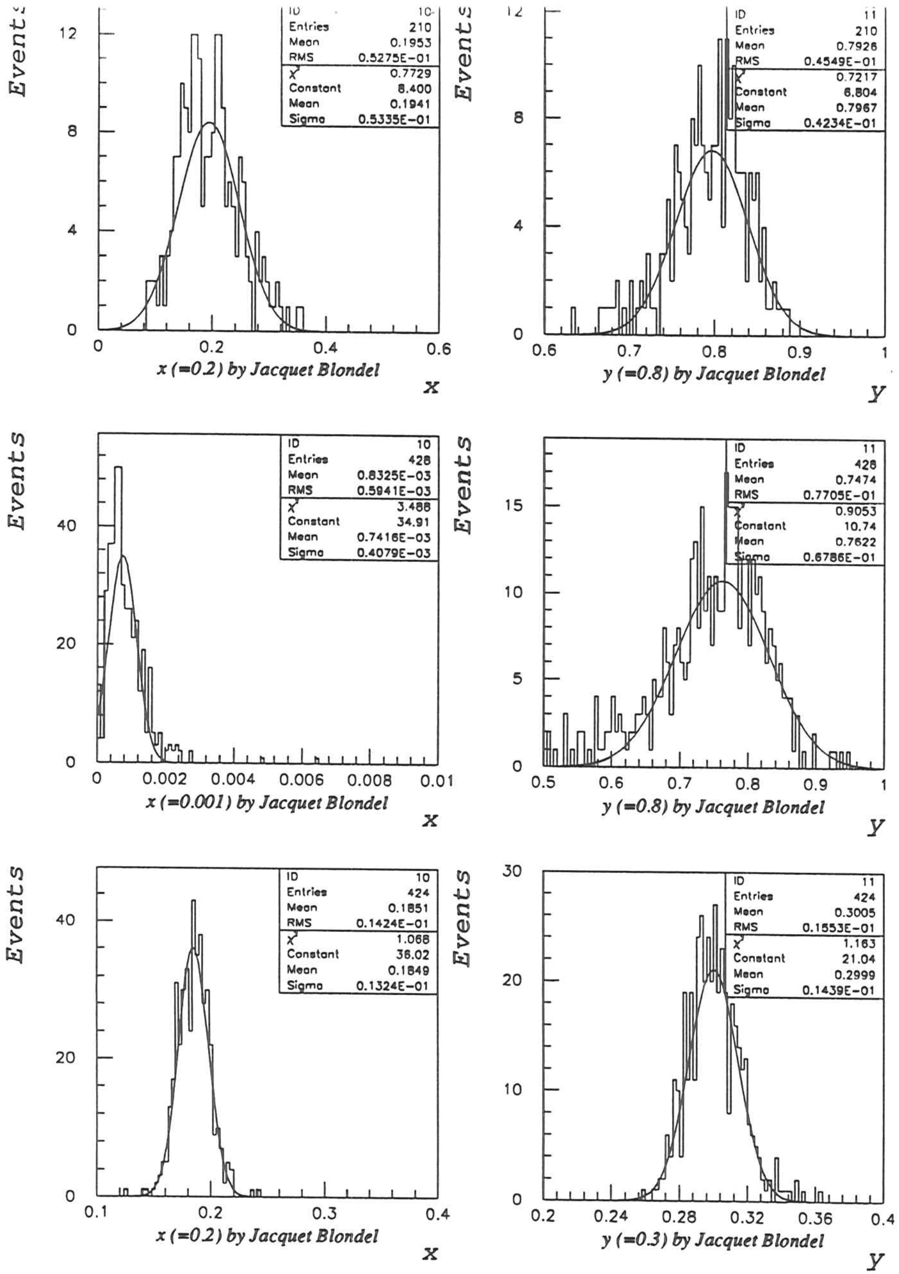

Figure 66: x and y reconstructed with the method of Jacquet and Blondel of events produced with the ZEUS Monte Carlo. The magnetic field is switched on and there is no material in front of the calorimeter.

Method:	Electron				Jacquet-Blondel			
Parameter:	$\Delta x/\bar{x}$	$\sigma_x/\bar{x}$	$\Delta y/\bar{y}$	$\sigma_y/\bar{y}$	$\Delta x/\bar{x}$	$\sigma_x/\bar{x}$	$\Delta y/\bar{y}$	$\sigma_y/\bar{y}$
$x = 0.2$ & $y = 0.8$	0.7 %	2.2 %	0.0 %	1.2 %	2.4 %	26.4 %	0.9 %	5.7
$x = 0.001$ & $y = 0.8$	8.1 %	10.0 %	0.9 %	2.1 %	16.8 %	59.4 %	6.6 %	9.6
$x = 0.2$ & $y = 0.3$	1.1 %	7.1 %	1.4 %	6.0 %	7.5 %	7.1 %	0.2 %	5.2

Table 20: Mean deviations and spread of the reconstructed values of x and y from the generated values for data with no material in front of the calorimeter and the magnetic field switched on

Method:	Electron				Jacquet-Blondel			
Parameter:	$\Delta x/\bar{x}$	$\sigma_x/\bar{x}$	$\Delta y/\bar{y}$	$\sigma_y/\bar{y}$	$\Delta x/\bar{x}$	$\sigma_x/\bar{x}$	$\Delta y/\bar{y}$	$\sigma_y/\bar{y}$
$x = 0.2$ & $y = 0.8$	0.1 %	2.2 %	0.3 %	1.2 %	13.9 %	24.2 %	3.2 %	6.2
$x = 0.001$ & $y = 0.8$	11.4 %	9.7 %	1.6 %	2.1 %	31.8 %	42.1 %	8.8 %	9.0
$x = 0.2$ & $y = 0.3$	2.5 %	6.5 %	2.3 %	5.6 %	13.1 %	7.6 %	0.5 %	5.3

Table 21: Mean deviation of the reconstructed values of x and y from the generated values for data with material in front of the calorimeter and the magnetic field switched on

For the method of Jacquet and Blondel a changing width due to the material in front of the calorimeter cannot be seen (figure 69), but there is a significant shift of the mean values. The relative deviations from the reconstructed values of x with and without material in front of the calorimeter are 12% for the sample with x=0.2,y=0.8 , 15% for the sample with x=0.001,y=0.8 and 6% for the sample with x=0.2,y=0.3. The effect for y is much smaller ($\approx 1\%$).

Reconstruction With a Cluster Finding Algorithm For all preceding studies the energies and angles of the electron had been selected with cuts on the solid angle. The accepted cells were in the range $\theta_{calc} \pm 5^0$ and $\phi_{calc} \pm 5^0$. Both angles (θ_{calc} and ϕ_{calc}) are know from the eventgenerator.

For a comparision the energy sums and angles used for determining x and y have been calculated with the cluster finding algorithm which is currently implemented in ZEPHYR (see section A.1). It is the same algorithm which is used in the second level trigger of the calorimeter.

Figure 70 can be directly compared with figure 68. Figure 70 shows that the mean values are reconstructed well, but there are two difficulties: first there are big tails which are absent in the plots of figure 68, which have been calculated from the same Monte Carlo data. The second problem is the low efficiency. For the sample with $x = 0.2, y = 0.8$ only 77%, for the sample with $x = 0.001, y = 0.8$ only 66%, and for the sample with $x = 0.2, y = 0.3$ only 95% of the events have been identified by the cluster algorithm. This means that clusters are not recognized efficiently enough, even though an identification as electron or hadron cluster has

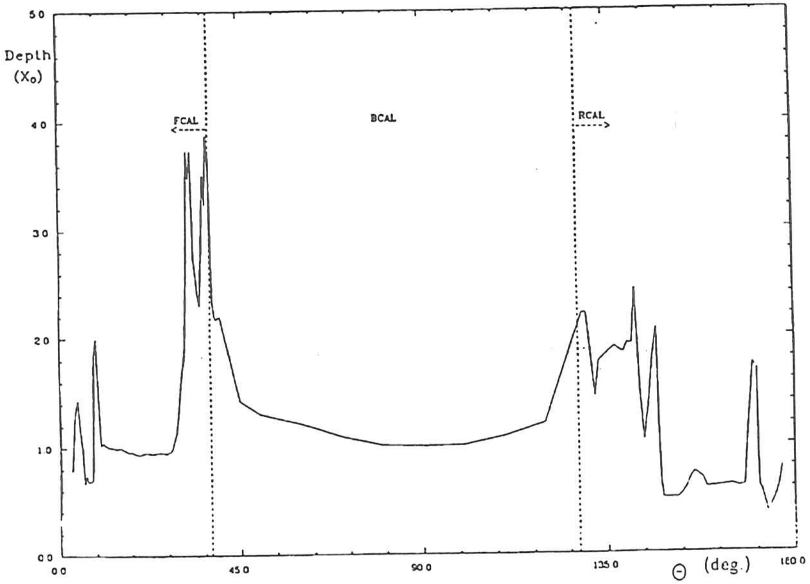

Figure 67: Dead material in front of the calorimeter versus the space angle θ [ZEU86]

been accepted.

9.5.3 Summary

Figure 71 summarizes the results of the previous plots. Like in the previous figure the three rows correspond to the three kinematical regions. These are from the top to the bottom, $(x = 0.2, y = 0.8)$, $(x = 0.001, y = 0.8)$ and $(x = 0.2, y = 0.3)$. The left column shows the results for the method of Jacquet Blondel and the right column for the method which uses the data from the electron. The plots show the relative errors of x and y $(\Delta x/\bar{x}$ and $\Delta y/\bar{y})$. The legend in the left bottom box explains the symbols. The used abreviations are:

Lepto (precise) : The events have been produced with the LEPTO V5.2 event generator. Only an angle cut which corresponds to the beampipe has been applied. Only the results for the method of Jacquet and Blondel are shown. The corresponding histograms are in figure 60.

Lepto 35,20 : The events produced as in LEPTO (precise) have been smeared with the energy resolutions $(\sigma/E) = 35\%/\sqrt{E}$ for hadrons and $= 20\%/\sqrt{E}$ for electrons. The corresponding histograms are shown in figure 62 and 61.

Lepto 50 : Like Lepto 35 but with an energy resolution of $50\%/\sqrt{E}$ for the hadrons. The corresponding histograms are not shown.

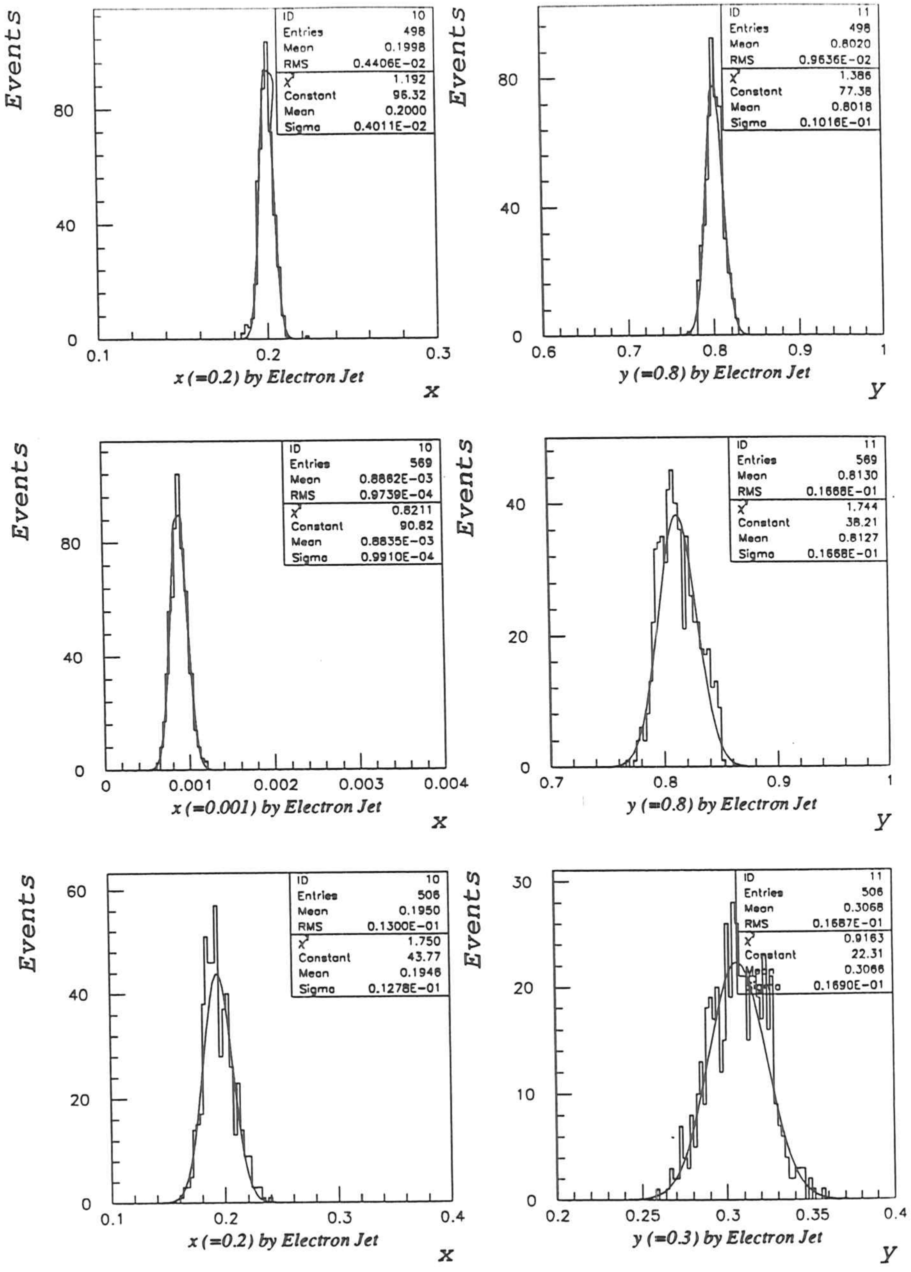

Figure 68: x and y reconstructed with the electron data produced with the ZEUS Monte Carlo. The magnetic field is switched on and the material in front of the calorimeter is inserted.

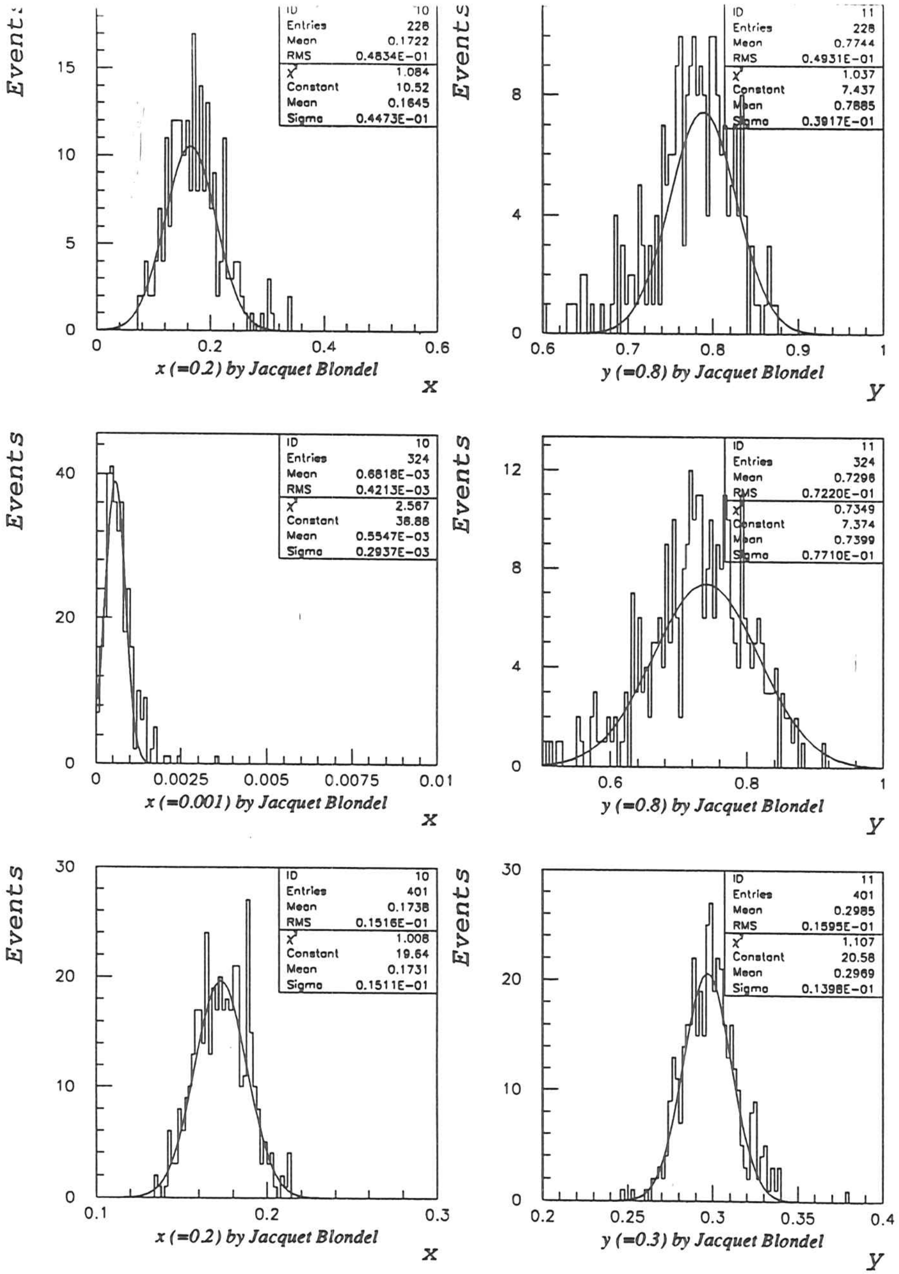

Figure 69: x and y reconstructed with the method of Jacquet and Blondel from data produced with the ZEUS Monte Carlo. The magnetic field is switched on and the material in front of the calorimeter is inserted.

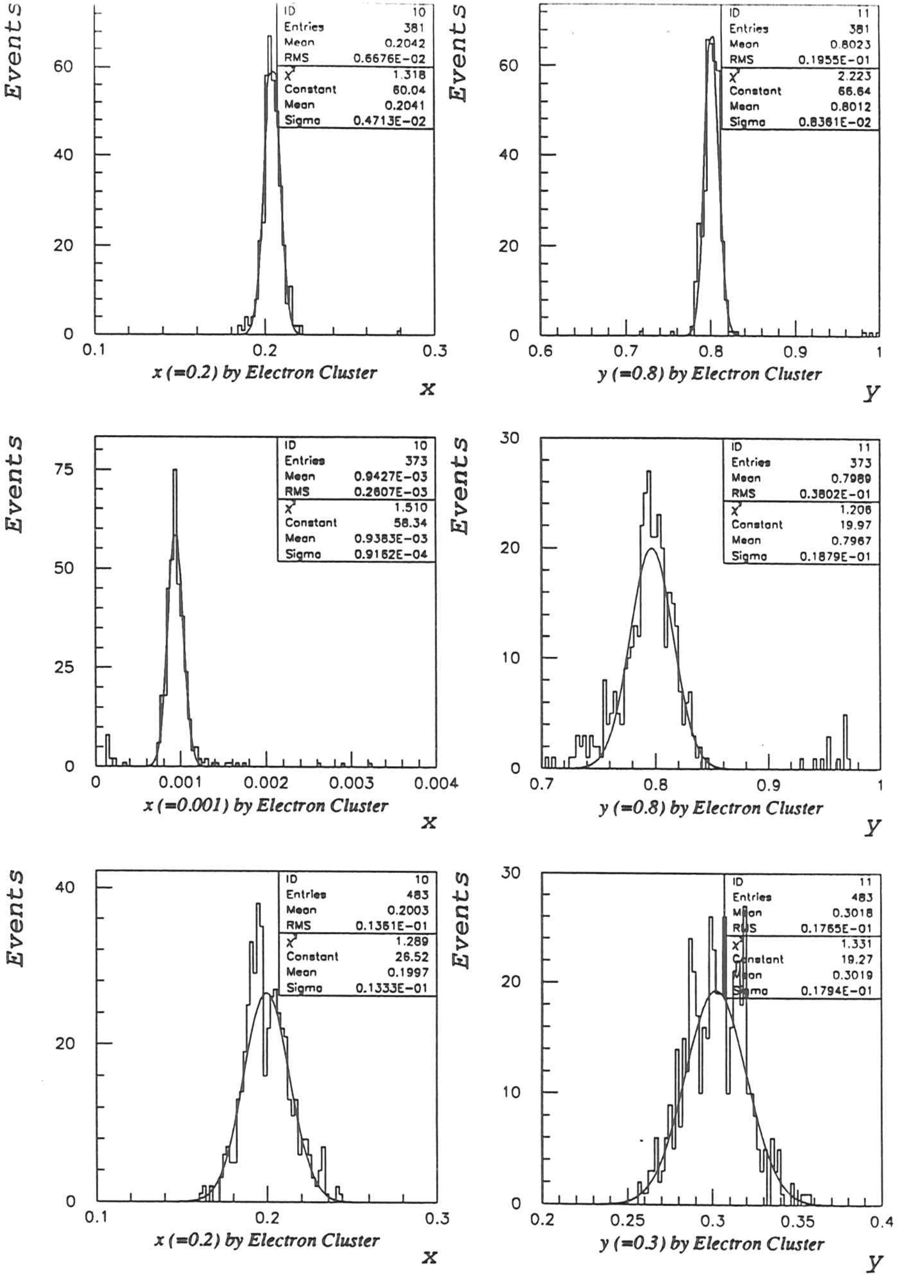

Figure 70: x and y reconstructed with the electron from data produced with the ZEUS Monte Carlo. The magnetic field is switched on and there is material in front of the calorimeter. A cluster finding algorithm has been used.

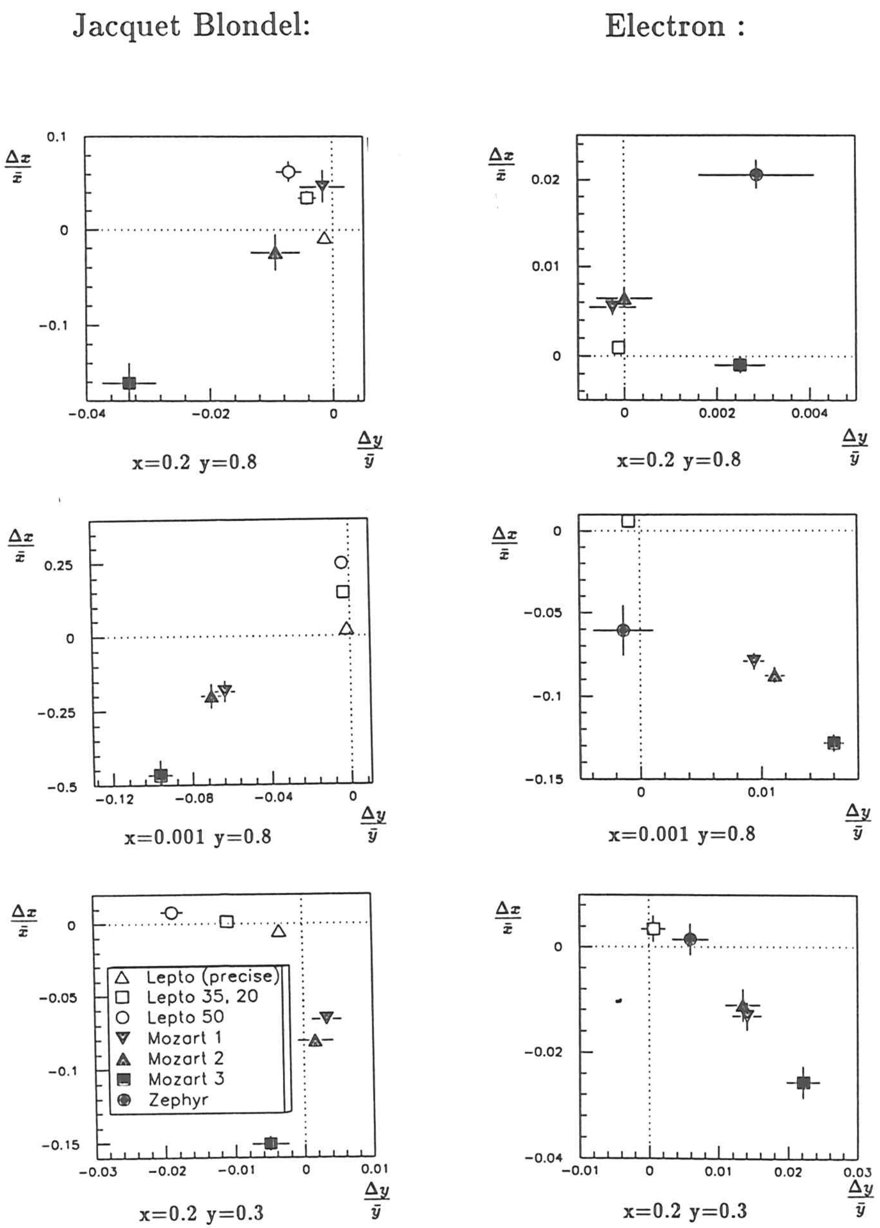

Figure 71: A summary of the relative errors in x,y for the various simulations is shown. The left column corresponds to the method of Jacquet and Blondel and the right column to the method based on the electron.

Method:	Jacquet-Blondel			
Parameter:	$\Delta x/\bar{x}$	$\sigma_x/\bar{x}$	$\Delta y/\bar{y}$	$\sigma_y/\bar{y}$
$x = 0.2$ & $y = 0.8$	2.1 %	3.3 %	0.3 %	2.4 %
$x = 0.001$ & $y = 0.8$	5.8 %	26.0 %	0.1 %	4.8 %
$x = 0.2$ & $y = 0.3$	0.2 %	6.8 %	0.6 %	5.9 %

Table 22: Mean deviations and spread of the reconstructed values of x and y from the generated values for data with material in front of the calorimeter and the magnetic field switched on. A cluster algorithm has been used.

Mozart 1	: The events produced as in Lepto (precise) have been passed through a detector simulation with the Monte Carlo program Mozart. The magnetic field was switched off and there was no material in front of the calorimeter. The corresponding histograms are displayed in figures 63 and 64.
Mozart 2	: Like Mozart 1, but the magnetic field has been switched on. The corresponding histograms are shown in figures 65 and 66.
Mozart 3	: Like Mozart 2, but in addition the material in front of the calorimeter has been inserted. The corresponding histograms are shown in figures 68 and 69.
Zephyr	: The cluster finding algorithm of Zephyr has been run for the identification of the electron clusters. The same data set as for Mozart 3 has been used. The corresponding histograms are in figure 70.

The results of these plots can be summarized as follows.

- The errors increase with a more realistic simulation. The method which uses the electron is much more precise than the method of Jacquet and Blondel.
- While the effect due to the magnetic field is relatively small there is a big effect due to the material in front of the calorimeter. The relative increase of this error is similar for both methods.
- The efficiency of the cluster finding algorithm currently implemented in ZEPHYR is too low.

9.6 Effects of Calibration Errors and Noise

So far a perfect readout system without any noise and calibration errors has been assumed. To determine their influence the data of the full Monte Carlo with the magnetic field and the material in front of the calorimeter has been used. The data sets have been smeared with the assumed noise and calibration errors and x and y have been reconstructed. Finally the mean deviation ($\Delta x/\bar{x}$ and $\Delta y/\bar{y}$) due to these errors have been calculated.

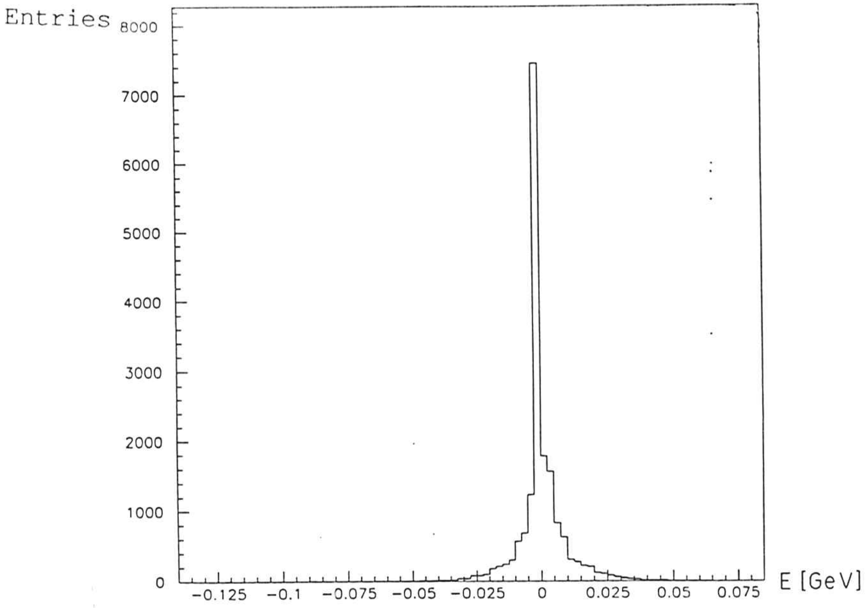

Figure 72: Noise spectrum of a calorimeter cell (EMC) determined by randomly triggered events. The RMS (noise) of the distribution is 0.0095 GeV (equivalent to 0.09 pC).

9.6.1 Noise

Two sources of noise in the calorimeter signals have been considered: uranium noise and electronic noise. The calorimeter signals are calibrated in a way that for many events without incoming particles the average value of each individual channel is zero. The noise adds a contribution to the true energy signal of every calorimeter section:

$$E_{meas} = E_{true} + E_{noise} \quad \text{with} < E_{noise} >= 0 \ .$$

Figure 72 shows the noise spectrum of a cell which had been read out in the test setup at CERN ($\approx$ 18 000 times) with a random trigger. The RMS of the noise distribution of this channel is $0.09pC$. This corresponds to $9.5MeV$ if one uses the result of the calibration at CERN that $1GeV$ corresponds to $9.51pC$. Figure 73 [AND91] shows the root mean square for all channels of one FCAL module. It is in between of $0.07 - 0.09pC$ for the channels of the EMC sections and $0.12 - 0.16pC$ for the channels of the HAC sections. The difference is due to the larger uranium signal in the HAC sections. The electronic part of the noise was determined by reducing the PMT voltage to 400 V. Its root mean square value is $0.04pC$.
At CERN there has been no evidence of correlation between different calorimeter cells. Correlations due to electronic pickup are sometimes difficult to avoid - so their influence has been studied also. Therefore two different kinds of noise are distinguished in this study: incoherent and coherent noise.

Incoherent Noise: Here the noise signals between the channels are not correlated. This is true for the uranium noise of different cells. A further contribution to the incoherent noise

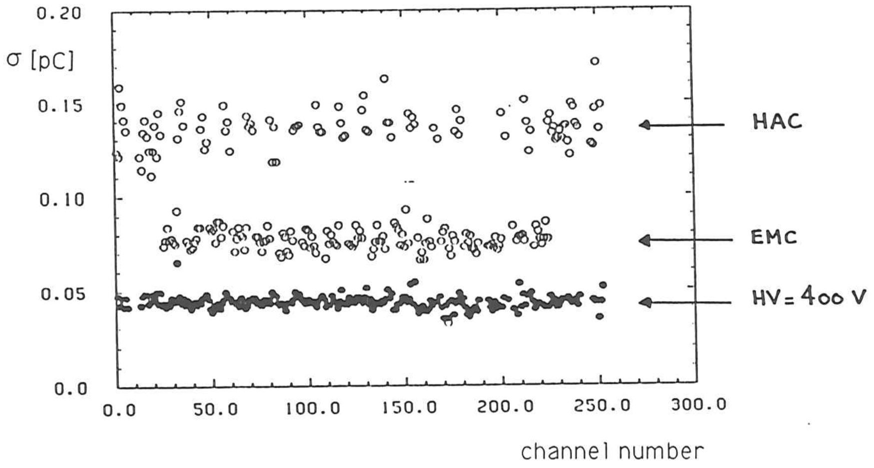

Figure 73: Root mean square of the noise spectrum of HAC and EMC for all channels of one FCAL module.

is the incoherent part of the electronic noise. This is the thermal noise of the amplifiers and drivers. The distribution function of the real noise does not have the shape of a Gaussian (figure 72), because the uranium noise consists of decays with different energies. But it does not show long tails and thus Gaussian distributed random numbers with a distribution of the correct width have been used for the simulation. Figure 73 shows that the noise in the EMC channels has a standard deviation in the order of $0.07 - 0.09pC$ (corresponding to 7 $\sim$ 9 MeV). Therefore Gaussian distributed random numbers with a sigma of 8 MeV have been used.

$$E_{noise,i} = S \cdot G(0, 8MeV)$$

$G(mean, \sigma)$: Gaussian distributed random numbers with mean value *mean* and rms σ

S = Scaling factor: The investigations have been with four different values of S With no noise (S=0), with the nominal noise (S=1) and twice and three times the nominal noise.

It turned out that the influence of the incoherent noise on the calorimeter reconstruction is very small. Even with an incoherent noise which is a factor 3 higher than the measured one, the error of the $x - y$ reconstruction is well below 1 % and thus can be neglected.

Coherent Noise: In this case the noise signals of the channels are correlated. There are several possibilities which can lead to coherent electronic noise. Power supplies which are not correctly shielded or grounded may induce a 50 Hz noise in cables. A value of the noise of 20 MeV has been used for the simulation.

$$E_{noise,c} = S \cdot 20MeV \cdot R$$

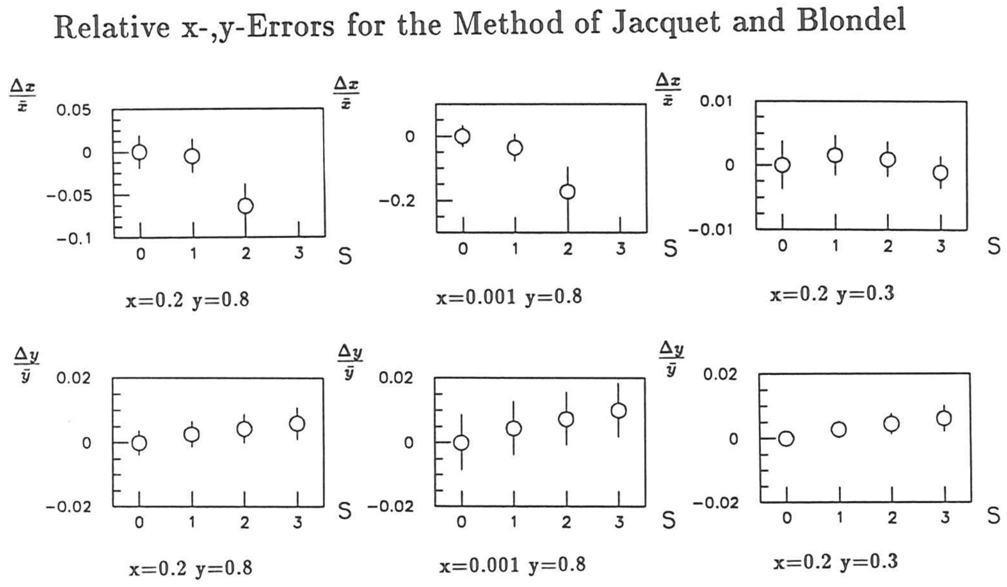

Figure 74: Relative error ($\Delta x/\bar{x}$ and $\Delta y/\bar{y}$) on the $x-y$ reconstruction for coherent noise. The plots show the relative error in x and y versus the scale for the noise.

R : flat random distribution between -1 and 1

S : scale factor (see above)

Figure 74 shows the resulting relative systematic shifts ($\Delta x/\bar{x}$ and $\Delta y/\bar{y}$) due to the coherent noise for the method of Jacquet and Blondel. This reconstruction method uses the information of many PMTs. Therefore coherent errors accumulate. The effect is especially critical for the x-value determination for the events with $x = 0.001$ and $y = 0.8$. A noise which is twice the assumed value results in a relative shift of ~ 20%.
In contrast, the relative shifts are very small for the reconstruction method which uses the electron.

9.6.2 Calibration Uncertainties

A coherent calibration error may be due to an uncertainty of the absolute value of the momentum of the CERN beam or a wrong intercalibration between EMC and HAC sections. results in a coherent calibration error. The calibration of the calorimeter has been done with great care. The aim of the work at CERN which has been described in chapter 6 was to determine the calibration values. Nevertheless there will be calibration uncertainties (ϵ):

$$E_{measured} = E_{true}(1+\epsilon)$$

section	energy & particles		$\sigma_{in}/\bar{E}$ [%] FCAL	$\sigma_{in}/\bar{E}$ [%] RCAL
EMC/HAC0	100 GeV/c	muons	1.0 %	0.8 %
	15 GeV/c	electrons	0.9 %	1.2 %
	100 GeV/c	electrons	1.0 %	1.3 %
HAC1	100 GeV/c	muons	0.4 %	0.6 %
	100 GeV/c	hadrons	1.0 %	1.1 %
HAC2	100 GeV/c	muons	0.6 %	-
	100 GeV/c	hadrons	2.4 %	-

Table 23: Spread of calibration ratios for all FCAL and RCAL modules calibrated with beam particles at CERN [AND91]. The quantity σ_{in} has been introduced in section 7.5 and uses the particle signals which are already normalized by the UNO signal.

As in the case of the calibration uncertainties we distinguish incoherent and coherent calibration errors.

Incoherent Calibration Error: This error is different for different photomultipliers. It has been assumed to be in the same as the spread of particle/UNO ratios which have been determined during the CERN test. Table 23 shows the spread in calibration ratios including the statistical errors averaged over all FCAL and RCAL channels which have been calibrated at CERN. These values are of the order of 1% except for hadrons in the HAC2 sections, where it is larger due to leakage effects. For the study an incoherent calibration error of 2% has been used for the simulation.

$$\epsilon = S \cdot G(0, 0.02)$$

The resulting error for x and y can be neglected like the effects due to incoherent noise. Within the statistical error the influence of a incoherent calibration is zero if it is averaged over many PMTs like it is done with the method of Jacquet Blondel.
There is a small effect for the method using the electron which uses only a few cells. For $S = 3$ this shift is 1 % in Δx (figure 75) for $x = 0.2$ and $y = 0.3$.

Coherent Calibration Error A wrong energy scale (e.g. like the absolute knowledge of the momentum of the CERN beam or a wrong intercalibration between EMC and HAC) results in a coherent calibration error. The error in the determination of the absolute beam momentum has been estimated to ~ 1% (see section 6). At ZEUS there may be additional effects like uncertainties due to the dead material in front of the calorimeter. The error used for the simulation has been assumed to be

$$\epsilon = 2\%.$$

Three different cases have been investigated. The calibration of the HAC and EMC sections can be both wrong and the calibration of each of them can be separately wrong.

At first a wrong calibration of HAC and EMC

$$\epsilon_{EMC} = 2\% \quad \epsilon_{HAC} = 2\%$$

is assumed. This has a severe influence on the reconstruction. The assumed calibration error results in errors in the order of 10% occur for the reconstruction of x with the method of Jacquet and Blondel. The third kinematic sample ($x = 0.2, y = 0.3$) is less sensitive to this reconstruction method. But this sample shows big relative errors for the method using the electron. The relative errors for the assumed calibration error are in this case:

$$\frac{\Delta x}{\bar{x}} = -7.6\% \text{ and } \frac{\Delta y}{\bar{y}} = 5.1\%.$$

This shows the importance of a precise absolute calibration.
To study the effect of a wrong intercalibration between the HAC and the EMC sections both have been varied independently. First a coherent calibration error of the HAC sections is assumed.

$$\epsilon_{EMC} = 0\% \quad \epsilon_{HAC} = 2\%$$

The plots (figure 77) show that a wrong calibration of the HAC sections only is less severe than a wrong calibration of the whole calorimeter. Obviously this wrong calibration has no influence on the reconstruction via the electron. The effect for the reconstruction via Jacquet Blondel is similar but less severe than a calibration error for the whole calorimeter. Finally there is the case that only the EMC has been calibrated wrongly.

$$\epsilon_{EMC} = 2\% \quad \epsilon_{HAC} = 0\%$$

The errors due to a miscalibration of the EMC sections can be understood in the same way as for the wrong calibration of the HAC sections. The errors induced into reconstruction via the electron are the same as for the miscalibration of the whole calorimeter. Even for the Jacquet Blondel method the error is slightly bigger than in the wrong calibration of only the HAC sections.
A list of the complete numerical results of this investigations is given in appendix D tables 26 to 31.

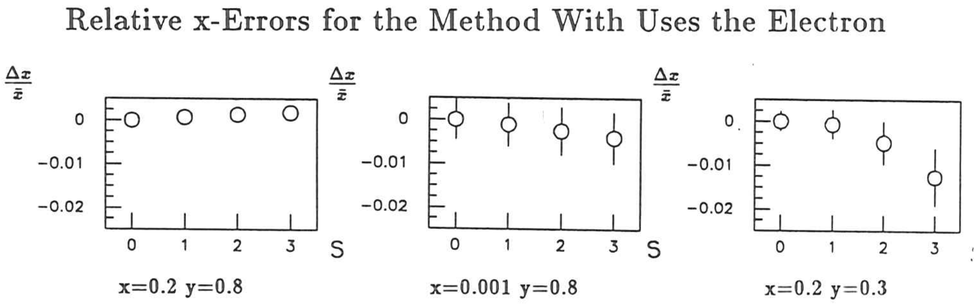

Figure 75: Relative error ($\Delta x/\bar{x}$) on the $x-y$ reconstruction for an incoherent calibration error. The plots show the relative error in x and y versus the calibration error. $S = 1$ correspond to twice the value expected for the ZEUS calorimeter. The three columns correspond to the three kinematic regions.

Relative x-,y-Errors for the Method of Jacquet and Blondel

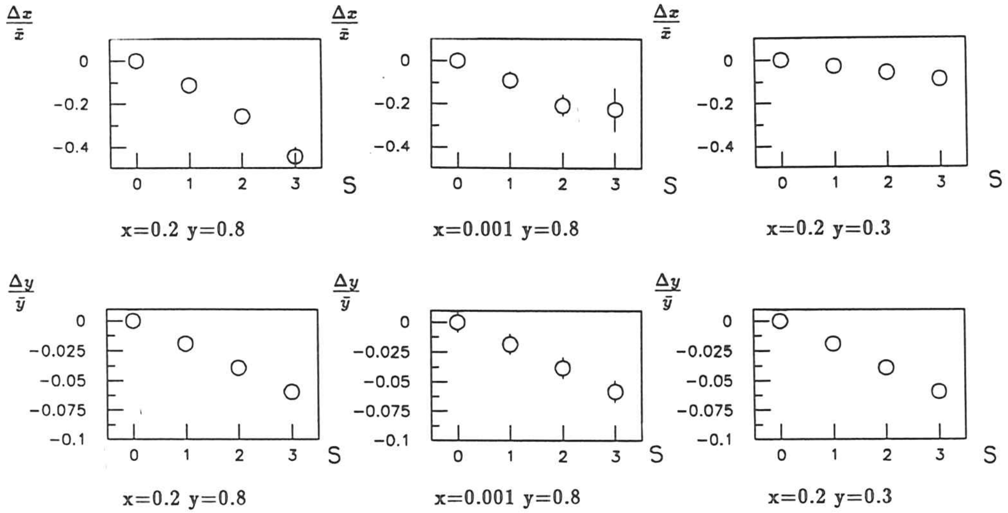

x=0.2 y=0.8 x=0.001 y=0.8 x=0.2 y=0.3

x=0.2 y=0.8 x=0.001 y=0.8 x=0.2 y=0.3

Relative x-,y-Errors for the Method Which Uses the Electron

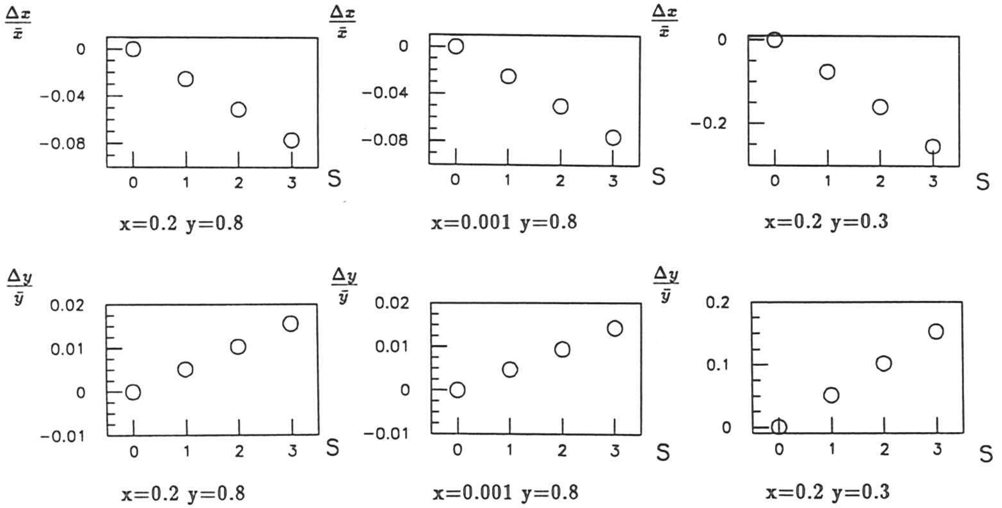

x=0.2 y=0.8 x=0.001 y=0.8 x=0.2 y=0.3

x=0.2 y=0.8 x=0.001 y=0.8 x=0.2 y=0.3

Figure 76: Relative error on the $x - y$ reconstruction for a coherent calibration error. The plots show the relative error in x and y versus the calibration error.

Relative x-,y-Errors for the Method of Jacquet and Blondel

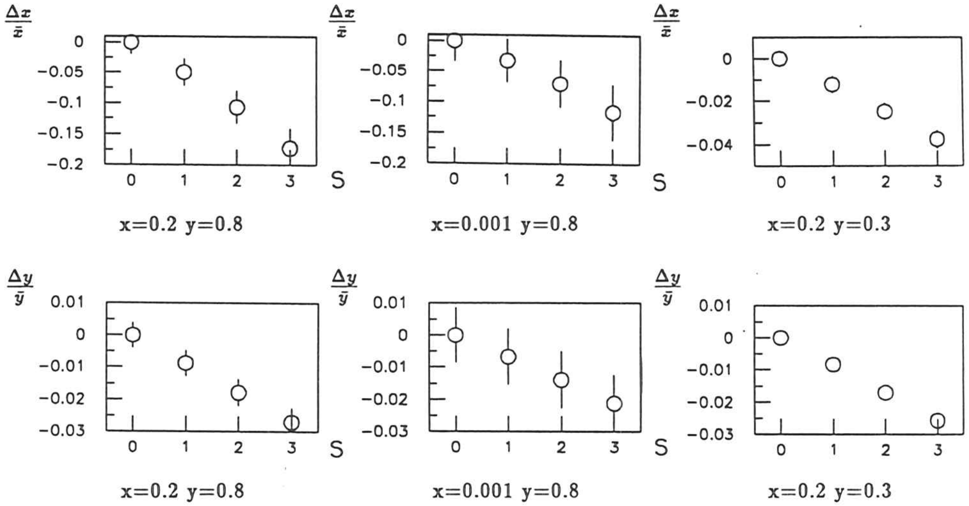

x=0.2 y=0.8 x=0.001 y=0.8 x=0.2 y=0.3

x=0.2 y=0.8 x=0.001 y=0.8 x=0.2 y=0.3

Figure 77: Relative error of the $x - y$ reconstruction for a wrong calibration of the HAC sections only. The plots show the relative error in x and y versus the scale for the calibration error.

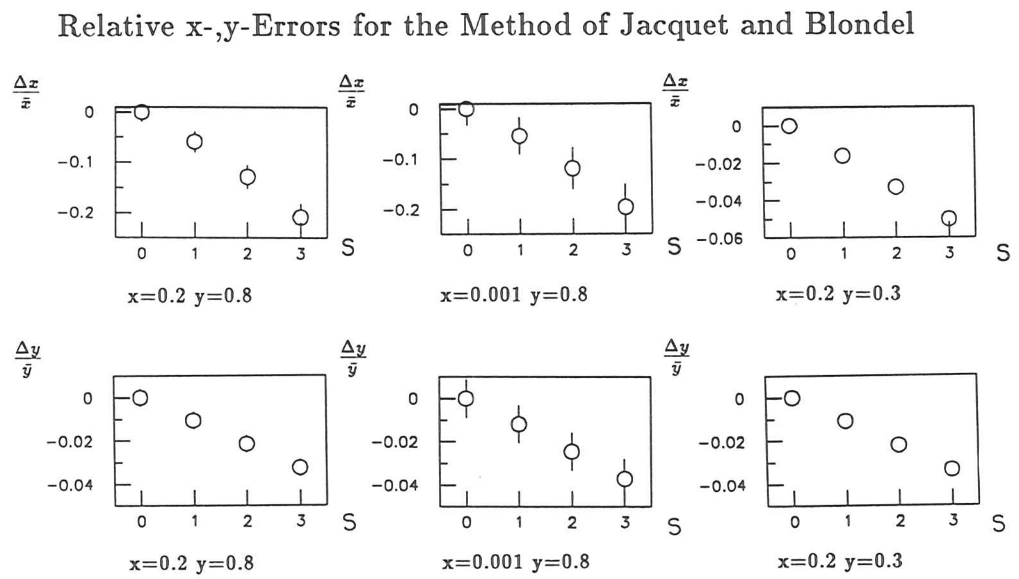

Figure 78: Relative error on the x-y reconstruction for a wrong calibration of the EMC sections only. The plots show the relative error in x and y versus the scale for the noise.

9.7 Summary of Reconstruction Errors

During the tests at CERN systematic errors of the momentum measurement of particles (electrons, muons and hadrons) have been measured with the ZEUS calorimeter. The main effects are noise and calibration errors. Both noise and calibration errors can be correlated or uncorrelated between the channels. The influence of these four systematic effects on the reconstruction of the DIS variables x and y has been investigated. For the investigation the deposited energies in the calorimeter which have been simulated by a Monte Carlo program have been smeared with the assumed errors.

It has been found that the method of Jacquet and Blondel is more sensitive than the reconstruction method which uses the electron. Effects which are correlated between the channels are much more severe than effects which are uncorrelated between the channels. In particular incoherent noise and calibration errors as measured for ZEUS have an effect which is smaller than 1%.

Also the value of x is more sensitive to systematic effects than the value of y. Especially the reconstruction for small values of x is very sensitive to all kinds of coherent calorimeter effects. The relative error of x and y introduced by the assumed correlated noise of 2% is below 1% except for the reconstructed x of the events with $x = 0.001$ & $y = 0.8$ where the error is 3.6%.

A wrong absolute energy scale has serious effects depending on the kinematic region both for the method which uses the electron and the method of Jacquet and Blondel. Even an assumed error of 2% limits the reconstruction accuracy of both methods. For the three tested samples the errors for x with the method of Jacquet and Blondel are $3-11\%$ and the errors for y are in the order of 2%. With the method which uses the electron the error for x is between $2.5-7.5\%$. Depending on the kinematic region the error for y is between 0.5 and 5%. Thus a common calibration error has the most severe influence on the $x-y$ reconstruction. All effects which introduce an additional error to the energy scale determined at CERN ($\delta p/p \sim 1\%$) have to be avoided. Therefore e.g. the effect due to the dead material in front of the calorimeter has to be well known.

10 Conclusion

In the first part a description and evaluation of the calibration methods for the ZEUS uranium scintillator calorimeter are given. A calibration procedure with muons has been developed. The method uses a fit of a truncated Landau distribution to the energy distribution of the muons in the calorimeter. It allows a calibration with muons which is of the same precision as the calibration with electrons. With the use of this method especially the precision of the calibration of the hadronic sections and the intercalibration between the electromagnetic and the hadronic sections has been improved by a factor 2.

In a further investigation the influence of calibration errors and noise on the reconstruction of the deep inelastic scattering variables x and y has been investigated. The Monte Carlo simulation shows that effects which are uncorrelated between individual channels introduce only negligible errors on the x and y reconstruction. Calorimeter effects like noise and calibration errors which are correlated between the channels show a large effect on the reconstruction of the DIS variables. Especially the method of Jacquet-Blondel which has to be used for charged current reactions is more sensitive to a common calibration error than the method which uses the electron jet only. The simulations show further that even a slight error in the energy scale of 1% will introduce an appreciable error in the reconstruction. For a calibration error of 2% which corresponds to 2 times the predicted error and using the method with the electron jet the error for the sample with $x = 0.2$, $y = 0.3$ is 7.5% for x and 5% for y. Using the method of Jacquet and Blondel the error for the samples with $x = 0.2$, $y = 0.8$ and $x = 0.001$, $y = 0.8$ is $\approx$ 10% for x and 2% for y.

Appendix

A Software Environment for the Monte Carlo Studies

A.1 Software Structure

The investigations of section 9.5 have been done in the environment of the ZEUS offline software.

It consists of the event generator ZDIS[8], the Monte Carlo Program MOZART[9], the reconstruction program ZEPHYR[10] and the package for user analysis routines EAZE[11]. Figure 79 shows the interaction of the programs.

The user enters the parameter for the event generator (x,y-range, interaction) into a control file. The program ZDIS reads the information of the control file and starts the specified event generator with the chosen parameters. For the current study the LEPTO[12] [ING89a] event generator version 5.2 has been used.

The output of ZDIS is written to a file in ADAMO[13] tables and ZEBRA [ZOL88] format.

This output file may be used as the input file for the ZEUS Monte Carlo MOZART. The Monte Carlo program takes the stable particles produced by the event generator and propagates them through the detector. The GEANT code is used for the propagation of the particles through matter. The output of MOZART consists of ADAMO tables. Several tables are available which describe the interactions in the calorimeter. The deposited energies with references to the particles which deposited the energy as well as calibrated PMT counts are available.

These tables may be analyzed by the ZEUS reconstruction code ZEPHYR. The clusters and reconstructed kinematic parameters calculated by algorithms implemented in ZEPHYR are written to ADAMO tables.

All these ADAMO data files can be analyzed with user code implemented in EAZE. EAZE allows also the manipulation of data sets. This facility has been used to study the effect of noise and calibration errors on the data sets (section 9.6.1). The filtering of corrupted Monte Carlo Events before further analysis has been done also with this program.

A.2 Cuts to Remove Corrupted Events due to Monte Carlo Errors

During the analysis two Monte Carlo errors have been detected. The effects occur only in the Monte Carlo and not in the real calorimeter.

Error 1: Electrons hitting the gap between two calorimeter modules and penetrating partly through the wavelength shifter deposit only a small fraction of their energy in the calorimeter. Thus the histograms for the energy deposition of electrons show unphysical tails towards lower energies (see figure 80).

---

[8] ZEUS Deep Inelastic Scattering

[9] Monte Carlo for ZEUS Reconstruction

[10] ZEus PHYsic Reconstruction

[11] Effortless Analysis of ZEUS Events

[12] The LUND Monte Carlo for Deep Inelastic LEPTOn-Nucleon Scattering

[13] Aleph DAta MOdel

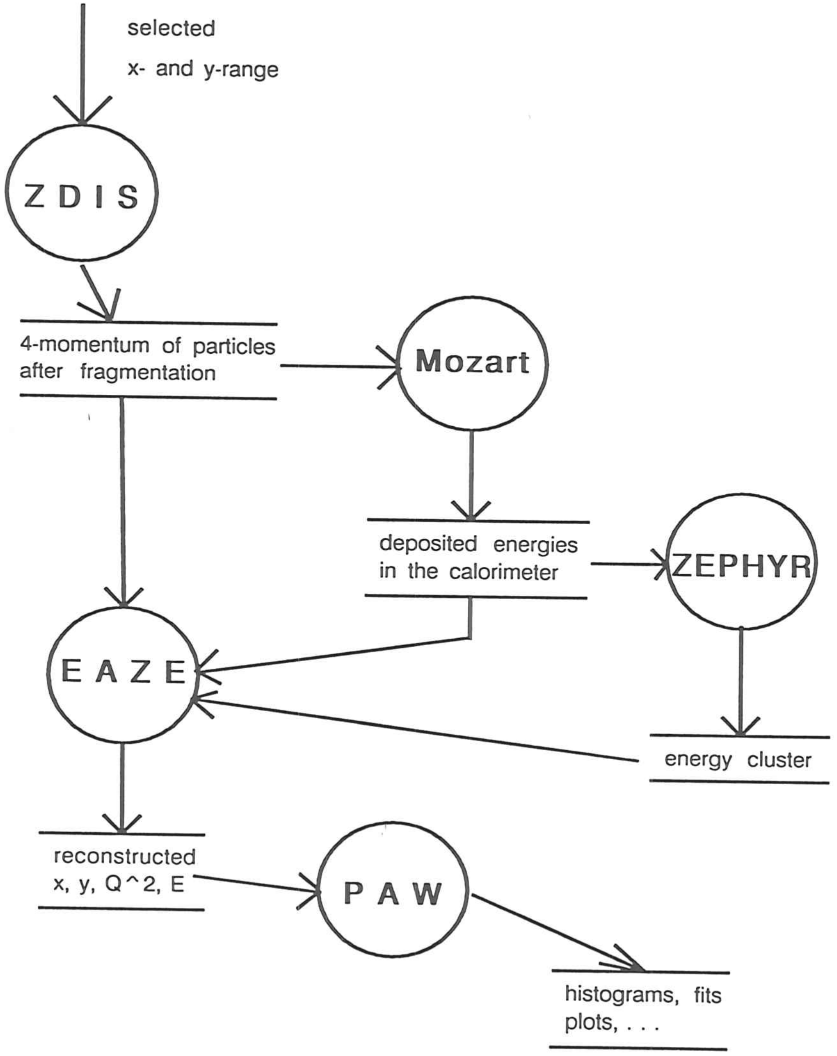

Figure 79: The structure of the ZEUS offline software. The figure uses the convention of a Data-Flow Diagram (DFD) of the SASD (Structured Analysis Structured Design) method. The arrows indicate data flows, the bubbles stand for processes and the pairs of bars are symbols for data stores.

	$x = 0.2$, $y = 0.8$	$x = 0.001$, $y = 0.8$	$x = 0.2$, $y = 0.3$
nominal e^- energy [GeV]	137.2	6.656	70.2
limit for e^- energy [GeV]	130.0	5.0	66.0
limit for p_T [GeV/c]	15.0	3.5	15.0
Fraction of rejected events	21 %	33 %	10 %

Table 24: Cuts applied to remove events with Monte Carlo errors

Error 2: In a small fraction of events neutrons and presumably other particles produced perpendicular to the beam do not deposit any energy in the calorimeter. Thus the momentum perpendicular to the beam (p_T) of the NC reactions shows unphysical tails towards higher momentum imbalances.

To remove the corrupted events cuts have been applied. The first error produces a long tail to lower energies in the energy deposition of electrons. Thus events with electrons which deposit not enough energy have been cut. Figure 80) illustrates which cuts are applied to remove events out of the Monte Carlo samples which are corrupted by the first detected Monte Carlo error (here called *Error 1*). The left side shows the electron energy of the event generator smeared with the energy resolution of $(20\%/\sqrt{E})$. The right side shows the deposited energies calculated by the Monte Carlo. The tails towards smaller energies are clearly seen. The applied cuts are indicated by the vertical lines in the plots. To remove these events which are corrupted by the second error only events with a momentum imbalance under a certain limit have been accepted. Figure 81 show the applied cuts to filter the corrupted events by the second Monte Carlo error (called *ERROR 2*) are shown. The plots show the momentum of the NC-events perpendicular to the beam. The left side shows the vertical momentum imbalance simulated with the event generator data smeared by the calorimeter resolution. In the Monte Carlo on the right side there are tails towards higher momentum imbalances. The tails are from particles which leave the vertex perpendicular to the beam and are not recognized. The vertical lines in the plots indicate the applied cuts. In both cases very wide cuts of at least 3 sigma have been applied to cut only corrupted events.
The deposited electron energy at the data samples with $x = 0.001$ and $y = 0.8$ show a very strong tail towards lower energies. Therefore a narrower cut of only 2.5 sigma has been used here. Table 24 shows which cuts are applied to remove the corrupted events. Only these events with an electron energy above the limit and a traverse momentum below the given limit are accepted.
A further problem with the used Monte Carlo version [HAR91] is that a part of the energy deposited by hadronic showers is lost. Therefore the response to hadrons is too low. To correct this effect samples of pions with 6 and 10 GeV have been shot into the three regions (FCAL, BCAL and RCAL) of the calorimeter. Table 25 shows the results of these tests. Especially in the RCAL a deviation from the nominal value was found (-7.5%). Therefore correction factors which have been calculated by the mean values of the runs with the two energies have been used. A significant improvement in the mean values has been found.

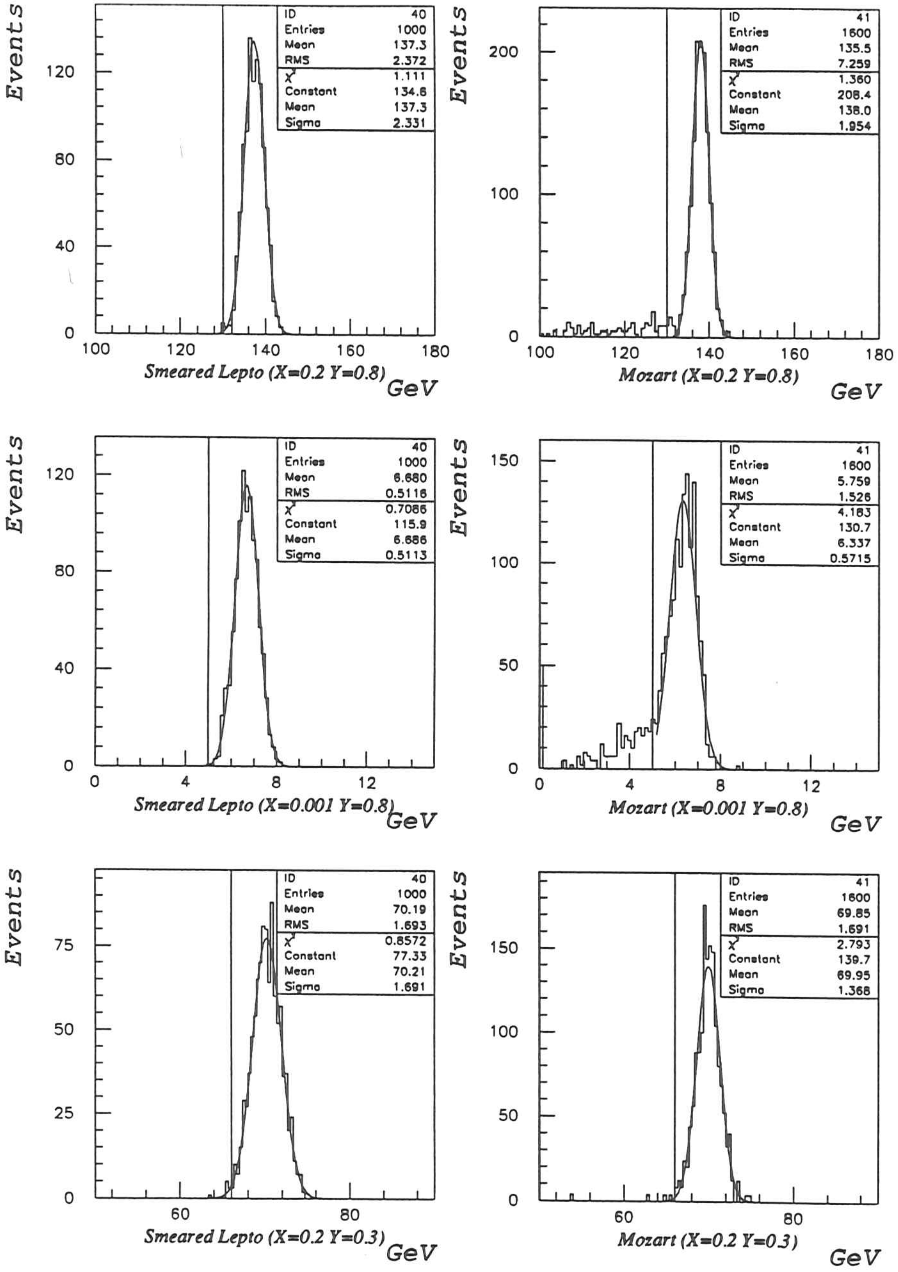

Figure 80: Cuts to filter events with a wrong electron energy

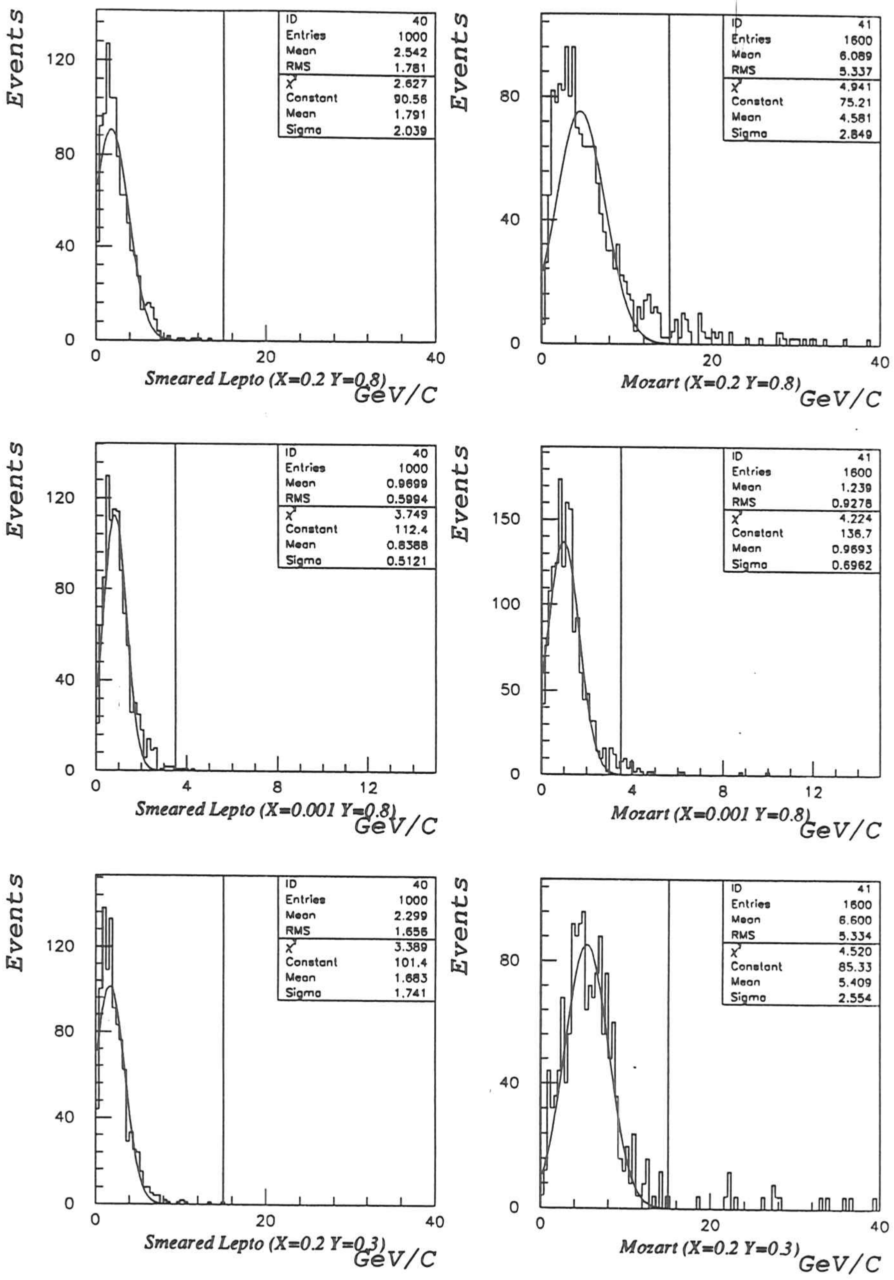

Figure 81: Cuts applied to remove events with wrong momentum perpendicular to the beampipe

Calorimeter Section	Particle	Energy	Measured Energy	Deviation [%]
FCAL	π^-	$6GeV$	5.742	- 4.3
		$10GeV$	9.718	- 2.8
BCAL	π^-	$6GeV$	5.890	- 1.8
		$10GeV$	9.761	- 2.4
RCAL	π^-	$6GeV$	5.549	- 7.5
		$10GeV$	9.254	- 7.5

Table 25: Results of Mozart test runs with single particles

B Parameters Chosen for the LEPTO Event Generator

For the current investigations the LEPTO event generator V5.2 has been used. As the interaction type electromagnetic and weak neutral current with interference has been selected. The calculations have been done in 1st order of α_s with string fragmentation. The F_2-parametrization has been done after Eichten et al. [EIC84] with $\Lambda_{0.2} = 0.2$. For the further parameters the default values have been used. The important ones of them are listed below:

- random rotation in azimutal angle of the whole event is done,
- fragmention is enabled,
- hard, first order QCD processes are enabled,
- max. number of flavours in expression for α_s is set to 4,
- the maximum flavour in sea structure functions is set to 4,
- the maximum flavour produced in 'photon'-gluon fusion is 4,
- baryon production from target remnant is included,
- the integrated cross-section is derived by an adaptive Gauss-Integration
- the sigma for the primordial transverse momentum distribution is set to 0.44,
- the probability that a ud-diquark in target remnant is I=S=0,
- $sin^2\theta_W = 0.215$,
- the minimum Q^2 in structure functions is 4 GeV^2.

C Comparison of Chi-Square and Maximum Likelihood Fits

The two most commonly methods for the estimation of parameters from experimental data are the Chi-square and the Maximum Likelihood Method.
If the data are filled into K bins with n_i entries in the bin i, and if σ_i is the standard deviation of the number of entries in the bin i and $f_i(\theta)$ is the value of the fit function dependent on a vector θ of fit parameters in the bin i, then the quantity which has to be minimized in the case of a Chi-Square fit is the following:

$$\chi^2 = \frac{1}{K}\sum_{i=1}^{K}\frac{[n_i - f_i(\theta)]^2}{\sigma_i^2} \qquad (48)$$

This equation assumes that there are no correlations between the bins. In the case of the Maximum Likelihood method the following quantity has to be minimized:

$$F = -\ln L(n \mid \theta) = -\sum_{i=1}^{K}\ln f(n_i, \theta) \qquad (49)$$

with the so called likelihood function $L(n \mid \theta)$. The function $f(n_i, \theta)$ is the probability that the fit function depending on the parameters θ agrees with the experimental data in bin i. It can be shown that both estimates are asymptotically identical in the case of infinite statistics. But it can also be shown that the m.l. method converges much faster. 'In particular, the m.l. method has usually no problems with bins with zero or few events.' 'These drawbacks are usually cured by grouping bins but at the price of loss of information. In contrast, the m.l. method for binned events becomes equivalent to the ordinary m.l. method when the width of the bins go to zero.' (from [EAD71] page 171)
This is in agreement with the investigations which have been made during this work.
The dependence on the cut Q_{max} was investigated. Figure 82 shows that the parameter fitted with the Maximum-Likelihood method is less sensitive to a variation of the upper cut. The corresponding plots for the parameter S are not shown because they look similar as the plots for W. The plots show that the value derived by both methods agree with a upper cut of $\sim 80pC$. Therefore Maximum Likelihood fits with a high upper cut of $80pC$ have been used for these data sets.

D Data for Noise and Calibration Uncertainties

Table 26 to 31 contain the complete data for the plots of section 9.6. Both Bjorken scale variables x and y have been reconstructed with the method of Jacquet Blondel and with the use of the electron. The nominal value of the noise or calibration uncertainty has been measured during the calibration of the calorimeter modules (e.g. [AND91]). The numbers in the column *Factor* indicate the factor with which the nominal noise has been multiplied before it has been added to the signal. All other numbers given are relative errors ($\delta x/\bar{x}$ and $\delta y/\bar{y}$) in percent.
These values have been calculated in the following way.
The smeared and the unsmeared values are based on the same Monte Carlo events and therefore correlated. Due to the correlation of the data the error has been calculated with

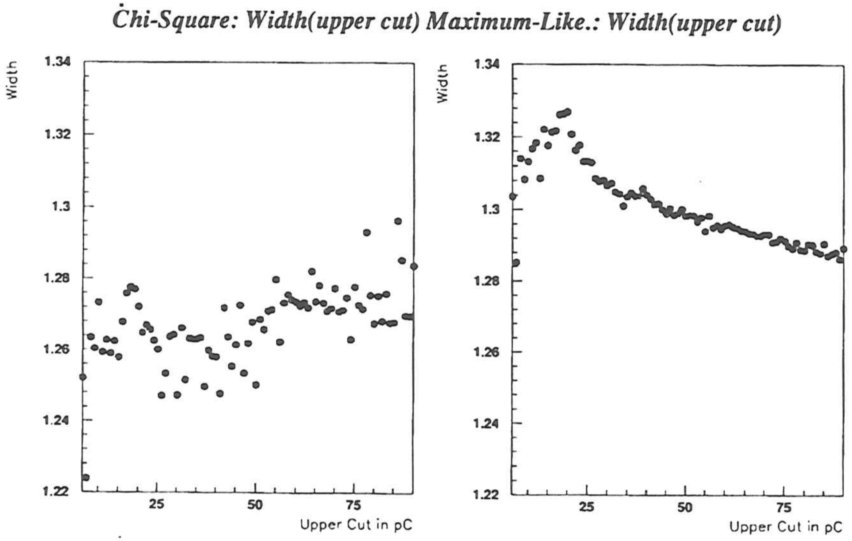

Figure 82: Value of the fitted parameter W as a function of the upper cut (Q_{max}) for the Chi-square (a) and the Maximum-Likelihood Method (b) with 100 bins

care using the fluctuations of subgroups. Each sample of ≈ 500 events has been split into 10 groups. Then the mean value of each group has been calculated. The error given in the tables 26 to 31 is the statistical error on the mean values of these 10 groups.

Variable	Factor	$x = 0.2$ & $y = 0.8$	$x = 0.001$ & $y = 0.8$	$x = 0.2$ & $y = 0.3$
Bjorken x by method of Jacquet Blondel	0	(0.0 ± 1.961) %	(0.0 ± 3.386) %	(0.0 ± 0.377) %
	1	(0.422 ± 1.924) %	(0.368 ± 3.416) %	(0.082 ± 0.380) %
	2	(0.364 ± 1.905) %	(-0.019 ± 3.496) %	(0.093 ± 0.385) %
	3	(0.278 ± 1.896) %	(-0.553 ± 3.595) %	(0.089 ± 0.388) %
Bjorken y by method of Jacquet Blondel	0	(0.0 ± 0.388) %	(0.0 ± 0.864) %	(0.0 ± 0.225) %
	1	(0.090 ± 0.388) %	(0.142 ± 0.866) %	(0.095 ± 0.224) %
	2	(0.078 ± 0.387) %	(0.119 ± 0.869) %	(0.060 ± 0.227) %
	3	(0.066 ± 0.387) %	(0.093 ± 0.873) %	(0.033 ± 0.227) %
Bjorken x by method of electron	0	(0.0 ± 0.131) %	(0.0 ± 0.463) %	(0.0 ± 0.237) %
	1	(0.002 ± 0.131) %	(-0.010 ± 0.467) %	(0.008 ± 0.238) %
	2	(0.006 ± 0.131) %	(-0.040 ± 0.471) %	(0.018 ± 0.239) %
	3	(0.006 ± 0.131) %	(-0.070 ± 0.476) %	(0.015 ± 0.239) %
Bjorken y by method of electron	0	(0.0 ± 0.058) %	(0.0 ± 0.117) %	(0.0 ± 0.264) %
	1	(0.0 ± 0.058) %	(0.002 ± 0.118) %	(-0.005 ± 0.265) %
	2	(-0.001 ± 0.058) %	(0.007 ± 0.119) %	(-0.012 ± 0.266) %
	3	(-0.001 ± 0.058) %	(0.013 ± 0.120) %	(-0.010 ± 0.267) %

Table 26: Relative errors ($\delta x/\bar{x}$ and $\delta y/\bar{y}$) due to the uncorrelated noise

Variable	Factor	$x = 0.2$ & $y = 0.8$	$x = 0.001$ & $y = 0.8$	$x = 0.2$ & $y = 0.3$
Bjorken x by method of Jacquet Blondel	0	(0.0 ± 1.961) %	(0.0 ± 3.386) %	(0.0 ± 0.377) %
	1	(-0.496 ± 1.994) %	(-3.590 ± 4.213) %	(0.155 ± 0.314) %
	2	(-6.346 ± 2.595) %	(-17.281 ± 7.643) %	(0.092 ± 0.271) %
	3	(-55.269 ± 25.888) %	(67.324 ± 91.355) %	(-0.110 ± 0.254) %
Bjorken y by method of Jacquet Blondel	0	(0.0 ± 0.388) %	(0.0 ± 0.864) %	(0.0 ± 0.225) %
	1	(0.269 ± 0.405) %	(0.444 ± 0.830) %	(0.279 ± 0.254) %
	2	(0.440 ± 0.442) %	(0.732 ± 0.820) %	(0.451 ± 0.324) %
	3	(0.607 ± 0.494) %	(1.002 ± 0.841) %	(0.618 ± 0.415) %
Bjorken x by method of electron	0	(0.0 ± 0.131) %	(0.0 ± 0.463) %	(0.0 ± 0.237) %
	1	(0.0 ± 0.131) %	(0.049 ± 0.450) %	(0.025 ± 0.236) %
	2	(-0.001 ± 0.132) %	(0.081 ± 0.456) %	(0.044 ± 0.235) %
	3	(0.003 ± 0.132) %	(0.146 ± 0.439) %	(0.054 ± 0.238) %
Bjorken y by method of electron	0	(0.0 ± 0.058) %	(0.0 ± 0.117) %	(0.0 ± 0.264) %
	1	(0.0 ± 0.058) %	(-0.011 ± 0.117) %	(-0.019 ± 0.261) %
	2	(0.0 ± 0.059) %	(-0.017 ± 0.118) %	(-0.033 ± 0.258) %
	3	(-0.001 ± 0.058) %	(-0.031 ± 0.114) %	(-0.041 ± 0.259) %

Table 27: Relative errors ($\delta x/\bar{x}$ and $\delta y/\bar{y}$) of the $x - y$ reconstruction due to correlated noise

Variable	Factor	$x = 0.2$ & $y = 0.8$	$x = 0.001$ & $y = 0.8$	$x = 0.2$ & $y = 0.3$
Bjorken x by method of Jacquet Blondel	0	(0.0 ± 1.961) %	(0.0 ± 3.386) %	(0.0 ± 0.377) %
	1	(0.378 ± 1.870) %	(0.415 ± 3.418) %	(0.031 ± 0.372) %
	2	(0.188 ± 1.809) %	(0.165 ± 3.509) %	(-0.030 ± 0.373) %
	3	(-0.179 ± 1.766) %	(-0.250 ± 3.615) %	(-0.097 ± 0.375) %
Bjorken y by method of Jacquet Blondel	0	(0.0 ± 0.388) %	(0.0 ± 0.864) %	(0.0 ± 0.225) %
	1	(0.097 ± 0.375) %	(0.150 ± 0.871) %	(0.088 ± 0.237) %
	2	(0.100 ± 0.362) %	(0.143 ± 0.883) %	(0.063 ± 0.248) %
	3	(0.100 ± 0.351) %	(0.129 ± 0.895) %	(0.037 ± 0.262) %
Bjorken x by method of electron	0	(0.0 ± 0.131) %	(0.0 ± 0.463) %	(0.0 ± 0.237) %
	1	(0.070 ± 0.103) %	(-0.114 ± 0.497) %	(-0.071 ± 0.335) %
	2	(0.132 ± 0.098) %	(-0.258 ± 0.540) %	(-0.489 ± 0.486) %
	3	(0.179 ± 0.120) %	(-0.411 ± 0.588) %	(-1.259 ± 0.657) %
Bjorken y by method of electron	0	(0.0 ± 0.058) %	(0.0 ± 0.117) %	(0.0 ± 0.264) %
	1	(-0.015 ± 0.055) %	(0.021 ± 0.124) %	(-0.024 ± 0.321) %
	2	(-0.031 ± 0.054) %	(0.045 ± 0.131) %	(-0.033 ± 0.415) %
	3	(-0.045 ± 0.056) %	(0.069 ± 0.140) %	(-0.031 ± 0.523) %

Table 28: Relative errors ($\delta x/\bar{x}$ and $\delta y/\bar{y}$) of the $x - y$ reconstruction due to a random calibration error

Variable	Factor	$x = 0.2$ & $y = 0.8$	$x = 0.001$ & $y = 0.8$	$x = 0.2$ & $y = 0.3$
Bjorken x by method of Jacquet Blondel	0	(0.0 ± 1.961) %	(0.0 ± 3.386) %	(0.0 ± 0.377) %
	1	(-11.248 ± 2.413) %	(-8.991 ± 3.919) %	(-2.857 ± 0.390) %
	2	(-25.730 ± 3.113) %	(-20.768 ± 4.982) %	(-5.833 ± 0.405) %
	3	(-44.452 ± 4.288) %	(-22.559 ± 10.047) %	(-8.872 ± 0.412) %
Bjorken y by method of Jacquet Blondel	0	(0.0 ± 0.338) %	(0.0 ± 0.864) %	(0.0 ± 0.225) %
	1	(-1.923 ± 0.397) %	(-1.857 ± 0.877) %	(-1.991 ± 0.230) %
	2	(-3.934 ± 0.405) %	(-3.844 ± 0.895) %	(-3.921 ± 0.234) %
	3	(-5.951 ± 0.416) %	(-5.833 ± 0.920) %	(-5.924 ± 0.241) %
Bjorken x by method of electron	0	(0.0 ± 0.131) %	(0.0 ± 0.463) %	(0.0 ± 0.237) %
	1	(-2.535 ± 0.134) %	(-2.509 ± 0.458) %	(-7.553 ± 0.278) %
	2	(-5.108 ± 0.140) %	(-5.020 ± 0.472) %	(-15.943 ± 0.322) %
	3	(-7.705 ± 0.145) %	(-7.624 ± 0.481) %	(-25.412 ± 0.381) %
Bjorken y by method of electron	0	(0.0 ± 0.058) %	(0.0 ± 0.117) %	(0.0 ± 0.264) %
	1	(0.516 ± 0.059) %	(0.471 ± 0.117) %	(5.090 ± 0.275) %
	2	(1.035 ± 0.061) %	(0.938 ± 0.120) %	(10.159 ± 0.281) %
	3	(1.554 ± 0.062) %	(1.421 ± 0.122) %	(15.256 ± 0.289) %

Table 29: Relative error ($\delta x/\bar{x}$ and $\delta y/\bar{y}$) of the $x - y$ reconstruction due to a common calibration error

Variable	Factor	$x = 0.2$ & $y = 0.8$	$x = 0.001$ & $y = 0.8$	$x = 0.2$ & $y = 0.3$
Bjorken x by method of Jacquet Blondel	0	(0.0 ± 1.961) %	(0.0 ± 3.386) %	(0.0 ± 0.377) %
	1	(-4.917 ± 2.243) %	(-3.243 ± 3.577) %	(-1.229 ± 0.385) %
	2	(-10.664 ± 2.643) %	(-7.026 ± 3.866) %	(-2.496 ± 0.396) %
	3	(-17.267 ± 3.215) %	(-11.652 ± 4.475) %	(-3.769 ± 0.410) %
Bjorken y by method of Jacquet Blondel	0	(0.0 ± 0.388) %	(0.0 ± 0.864) %	(0.0 ± 0.225) %
	1	(-0.876 ± 0.400) %	(-0.680 ± 0.871) %	(-0.834 ± 0.225) %
	2	(-1.789 ± 0.414) %	(-1.397 ± 0.879) %	(-1.706 ± 0.227) %
	3	(-2.706 ± 0.430) %	(-2.126 ± 0.887) %	(-2.574 ± 0.231) %
Bjorken x by method of electron	0	(0.0 ± 0.131) %	(0.0 ± 0.463) %	(0.0 ± 0.237) %
	1	(0.0 ± 0.131) %	(0.0 ± 0.463) %	(0.0 ± 0.237) %
	2	(0.0 ± 0.131) %	(0.0 ± 0.463) %	(0.0 ± 0.237) %
	3	(0.0 ± 0.131) %	(0.0 ± 0.463) %	(0.0 ± 0.237) %
Bjorken y by method of electron	0	(0.0 ± 0.058) %	(0.0 ± 0.117) %	(0.0 ± 0.264) %
	1	(0.0 ± 0.058) %	(0.0 ± 0.117) %	(0.0 ± 0.264) %
	2	(0.0 ± 0.058) %	(0.0 ± 0.117) %	(0.0 ± 0.264) %
	3	(0.0 ± 0.058) %	(0.0 ± 0.117) %	(0.0 ± 0.264) %

Table 30: Relative error ($\delta x/\bar{x}$ and $\delta y/\bar{y}$) of the $x-y$ reconstruction due to a wrong calibration of the HAC sections

Variable	Factor	$x = 0.2$ & $y = 0.8$	$x = 0.001$ & $y = 0.8$	$x = 0.2$ & $y = 0.3$
Bjorken x by method of Jacquet Blondel	0	(0.0 ± 1.961) %	(0.0 ± 3.386) %	(0.0 ± 0.377) %
	1	(-5.894 ± 2.112) %	(-5.457 ± 3.688) %	(-1.618 ± 0.385) %
	2	(-12.851 ± 2.313) %	(-11.937 ± 4.090) %	(-3.295 ± 0.394) %
	3	(-20.841 ± 2.584) %	(-19.628 ± 4.586) %	(-5.006 ± 0.399) %
Bjorken y by method of Jacquet Blondel	0	(0.0 ± 0.388) %	(0.0 ± 0.864) %	(0.0 ± 0.225) %
	1	(-1.047 ± 0.386) %	(-1.177 ± 0.870) %	(-1.077 ± 0.231) %
	2	(-2.145 ± 0.384) %	(-2.447 ± 0.880) %	(-2.215 ± 0.237) %
	3	(-3.246 ± 0.386) %	(-3.707 ± 0.898) %	(-3.349 ± 0.246) %
Bjorken x by method of electron	0	(0.0 ± 0.131) %	(0.0 ± 0.463) %	(0.0 ± 0.237) %
	1	(-2.535 ± 0.134) %	(-2.509 ± 0.458) %	(-7.553 ± 0.278) %
	2	(-5.108 ± 0.140) %	(-5.020 ± 0.472) %	(-15.943 ± 0.322) %
	3	(-7.705 ± 0.145) %	(-7.624 ± 0.481) %	(-25.412 ± 0.381) %
Bjorken y by method of electron	0	(0.0 ± 0.058) %	(0.0 ± 0.117) %	(0.0 ± 0.264) %
	1	(0.516 ± 0.059) %	(0.471 ± 0.117) %	(5.090 ± 0.275) %
	2	(1.035 ± 0.061) %	(0.938 ± 0.120) %	(10.159 ± 0.281) %
	3	(1.554 ± 0.062) %	(1.421 ± 0.122) %	(15.256 ± 0.289) %

Table 31: Relative error ($\delta x/\bar{x}$ and $\delta y/\bar{y}$) of the $x-y$ reconstruction due to a wrong calibration of the EMC sections

References

[AGO89] **d'Agostini, G. et al.**; Experimental Study of Uranium Plastic Scintillator Calorimeters; Nuclear Instruments and Methods A274 (1989) 134

[ALL75] **Allkofer O.C.**; Introduction to Cosmic Radiation;
Verlag Karl Thiemig (1975)

[AMA81] **Amaldi, U.**; Fluctuations in Calorimetry Measurements;
Phys. Scripta 23(1981)409

[AND88] **Anders, B.**; On Sampling Fractions and the Hadronic Resolution;
ZEUS-Note 88-026 (1988)

[AND90] **Andresen, A., et al.**; Response of a uranium-scintillator calorimeter to electrons, pions and protons in the momentum range 0.5-10 GeV/c; NIM A290 (1990) 95

[AND91] **Andresen, A., et al.**; Construction and Beam Tests of the ZEUS Forward and Rear Calorimeter; DESY-Note 91-026, PRC 91-02, ISSN 0418-9833 (1991)

[BAR68] **Bartel, W. et al.**; Phys. Lett. 28B, 148 (1968)

[BAR89] **Barreiro, F., et al.**; Measurements of Longitudinal and Transverse Profiles for Hadron Showers in the Range 10-100 GeV and Comparisons with Monte Carlo Simulations; DESY-Note 89-171 (1989)

[BEH89] **Behrens, U., et al.**; Test of the ZEUS Forward Calorimeter Prototype; DESY-Note 89-128 (1989)

[BEH90] **Behrens, U.**; Vergleich von Monte-Carlo-Simulationen und experimentellen Ergebnissen für ein hadronisches Uran-Szintillator-Sampling-Kalorimeter;
PhD-Thesis Hamburg University (1990)

[BEN91] **Bénard, F. et al.**; ZEUS Third Level Trigger Monte Carlo Studies; ZEUS-Note 91-050 (1991)

[BER87A] **Bernardi, E. et al.**; Performance of a Compensating Lead-Scintillator Hadronic Calorimeter; Nuclear Instruments and Methods A262 (1987) 229

[BER87B] **Bernardi, E.**; On the Optimization of the Energy Resolution of Hadron Calorimeters; PhD-Thesis Hamburg University (1987)

[BER88] **Bernstein, A., Caldwell, A.**; Beam Study of Calorimeter Electronics;
ZEUS-Note 88-048 (1988)

[BEV69] **Bevington, P.R.**; Data Reduction and Error Analysis for the Physical Sciences;
McGraw-Hill Book Company (1969)

[BLO79] **Blondel, A., Jacquet, F.**; Proceedings of the study of an ep facility for Europe, Ed. U. Amaldi; DESY 79/48 (1979) 391 Data Reduction and Error Analysis for the Physical Sciences; McGraw-Hill Book Company (1969)

[BRU89] **Brun, R. , Couet, O. , Vandoni, C. , Zanarini, P.**; PAW - Physics Analysis Workstation: The Complete Reference; Version 1.07 (October 1989)

[BJO69] **Bjorken, J.D. , Paschos S.D.**; Phys. Rev. 185 (1969) 1975

[BLO69] **Bloom, E.D. et al.**; Phys. Rev. Lett. 23 (1969) 930

[BOT87] **Boterenbrood, H. et.al.**; A two-transputer VME module for the ZEUS experiment; NIKHEF-H, 1988

[BRA76] **Brandt, S.**; Statistical and Computational Methods in Data Analysis;
North-Holland Publishing Company (1976)

[BRE69] **Breidenbach, M. et al.**; Phys. Rev. Lett. 23 (1969) 935

[BRU87] **Brueckmann, H.**; On the Theoretical Understanding and Calculation of Sampling Calorimeters; DESY 87-064(1987)

[CAL89a] **Caldwell, A.**; Scale factors for the DU Calorimeter; February 18 (1989)

[CAL89b] **Caldwell, A.**; Calibration of the BCAL at FNAL and Beyond - version 1.0;
Draft July 18 (1989)

[CAL89c] **Caldwell, A., Fürtjes, A., Ros, E., Tsurugai,T.**; Test of Calorimeter Electronics and other Results obtained at the CERN-PS (November/December 88);
ZEUS-Note 89-45 (1989)

[Cat87] **Catanesi, M.G. et al.**; Hadron, Electron and Muon Response of a Uranium Scintillator Calorimeter; NIM A260 (1987) 43

[DIE90] **Dierks, K.**; Entwicklung eines präzisen Hadron-Kalorimeters;
PhD-Thesis Hamburg University, Interner Bericht DESY F35-90-01 (1990)

[EAD71] **Eadie, W.T., Dryard, D., James, F.E., Roos, M., Sadoulet, B.**;
Statistical Methods in Experimental Physics;
CERN, Geneva, North-Holland Publishing Company, Amsterdam, London (1971)

[EIC84] **Eichten, et al.**; Proton Structure Functions; Rev. Mod. Phys. 56 (1984) 579

[FAB85] **Fabjan , C.W.**; Calorimetry in High Energy Physics ; CERN-EP/85-54(1985)

[FAB87] **Fabjan, C.W.**; Calorimetry in High Energy Physics in : Ferbel, T. ;
Experimental Techniques in High Energy Physics, Addison-Wesley (1987)257

[FAW91] **Fawcett, H.F.**; The Effect of Variations in DU Plate Thickness on the Calibration of the ZEUS FCAL and RCAL; ZEUS-Note 91-28 (1991)

[FEL87] **Feltesse, J.**; Measurement of Inclusive Differential Cross Sections; Proceedings of the HERA Workshop Vol.1 (1987) 33-57

[FUE89] **Fürtjes, A., Ros, E., Tsurugai, T.**; Calorimeter Tests at the CERN-PS (I);
ZEUS-Note 89-69 (1989)

[FUE90] **Fürtjes, A.**; Verhalten des ZEUS Uran-Szintillator-Kalorimeters für niederenergetische Teilchen mit Energien von 0.2 - 10.0 GeV; Diploma Thesis Hamburg; Interner Bericht DESY F35-90-02 (1990)

[GEL68] **Gell-Mann, M. et al.**; Phys. Lett. 8 (1964) 214

[GLA91] **Glaeser, R.**; I/O for ZEUS Reconstruction; ZEUS-Note 91-29 (1991)

[GRE90] **Greif, H.**; Untersuchungen zur kalorimetrischen Messung von Jeteigenschaften in hochenergetischen Elektron-Proton Speicherring-Experimenten; PhD-Thesis Technische Universität München (1990)

[HAG90] **Hagge, L.**; Anwendungen von Transputern in der Hochenergiephysik; Diploma Thesis of Computer Science University Hamburg, October (1990)

[HAL84] **Halzen, F. and Martin, A.D.**; Quarks and Leptons; John Wiley and Sons, New York, Chichester, Brisbane, Toronto (1984)

[HAM88] **Hamatsu, R., Ros, E., Troconiz, J., and Tsurugai, T.**; First Test Results from the FCAL Prototype; ZEUS-Note 88-028 (1988)

[HAN83] **Hancock, S., James, F., Movchet, J., Rancoita, P.G., VanRossum, L.**; Energy-loss distributions for single particles and several particles in a thin Silicon absorber; Geneva, September 5 (1983)

[HAR91] **Hartner, G.**; private communication (1991)

[HER91] **Hervas, L.**; The Pipelined Readout for the ZEUS Calorimeter; PhD-Thesis Madrid University, Internal Report DESY F35D-91-01 (1991)

[H1D86] **H1 Collaboration**; Technical Proposal for the H1-Detector; DESY, Hamburg 1986 (1986)

[IMS89] **INMOS**; The Transputer Applications Notebook - Systems and Performance; INMOS Ltd., Bristol (1989)

[ING87] **Ingelman, G. et al.**; Deep Inelastic Physic and Simulation; Proceedings of the HERA Workshop Vol.1 (1987) 3-17

[ING89a] **Ingelman, G.**; LEPTO version 4.3, The LUND Monte Carlo for Deep Inelastic Lepton-Nucleon Scattering; The LUND Monte Carlo Programs (1989) 191-197

[ING89b] **Ingelman, G. , Rückl, R.**; Quark Momentum Distributions from *ep* Collisions: Strategies and Prospects; DESY 89-025 ISSN 0418-9833 (1989)

[KAW90] **Kawulski, N.**; Vergleich zwischen experimentellen Daten und Simulation im ZEUS - Kalorimeter; Diploma Thesis Hamburg University, December 1990

[KLA88] **Klanner, R.**; Test Program for the ZEUS Calorimeter; Nuclear Instruments and Methods A265 (1988) 200-209

[KLE84] **Kleinknecht, K.**; Detektoren für Teilchenstrahlung; Teubner (1984)

[KRU90] **Krüger, J.**; Length of Calorimeter and Effect of Absorber in Front of Calorimeters; DESY 90-163, ISSN 0418-9833

[KOE84] **K.S.Kölbig, K.S. and Schorr, B.**; A Program Package for the Landau Distribution; Computer Physics Communications 31 (1984) 97-111

[KRA90] **Krämer, M.**; Kalibration des ZEUS-Vorärtskalorimeters; PhD-Thesis Bonn University October (1990), ISSN-0172-8741

[KRE75] **Kreyszig, E.**; Statistische Methoden und Ihre Anwendungen; Vandenhoeck & Ruprecht in Goettingen (1975)

[LAN44] **Landau, L.**; On the Energy Loss of Fast Particles by Ionization; JOURNAL of PHYSICS Volume 8, No. 4 (1944)

[LOH81] **Lohrmann, E.**; Hochenergiephysik; Teubner (1981)

[LOH83] **Lohrmann, E. and Mess K.-H.**; Remarks on the Kinematics of e-p Collisions in HERA;
DESY HERA 83/08 (1983)

[LOH85] **Lohmann, W., Kopp, R., Voss, R.**; Energy Loss of Muons in the Energy Range 1-10000 GeV; CERN 85-03 (1985)

[LOH87] **Lohrmann, E.**; The HERA Machine - Status and Opportunities; DESY Internal Report F35D-87-01 (1987)

[MEN90] **Mennerich, F.**; Einlese und Transport von Experiment-Daten durch den ZEUS-Eventbuilder; Diploma Thesis Hamburg (1987)

[MOY54] **Moyal, J.E.**; Theory of Ionization Fluctuations; Phil. Magazine 46 (1955)263

[NAS89] **Nash, T.**; Proceedings of the Oxford Conference on Computing in High Energy Physics; Oxford April (1989)

[PDG88] **Particle Data Group**; Particle Properties Data Booklet from 'Review of Particle Properties'; Physics Letters B204, April 1988

[PER82] **Perkins, D.H.**; Introduction to High Energy Physics; Addison-Wesley(1982)

[ROS52] **Rossi, B.**; High Energy Particles; Prentice-Hall, Englewood Cliffs, NJ, (1952)

[ROS88] **Ros, E. and Tsurugai, T.**; Test of the FCAL Prototype Modules at High Energies; ZEUS-Note 88-086 (1988)

[SCH74] **Schorr, B.**; Programs for the Landau and the Vavilov Distributions and the Corresponding Random Numbers; Computer Physics Communications 7 (1974) 215-224

[SEL62] **Seltzer, S.M. and Berger, M.J.**; Energy-Loss Straggling of Protons and Mesons Tabulation of the Vavilov Distribution;
Nat. Ac. of Sciences, Nuclear Science Series 39, (1964)

[SOE90] **Söding, P.**; Status and Physics Program of HERA; talk given at the LHC Workshop Aachen, October (1990)

[SMI90] **Smith, W.H. et al.** ; The ZEUS Trigger System; ZEUS-Note 89-084 (1990)

[STE84] **Sternheimer, R.M., Berger, M.J. & Seltzer, S.M.**; Atomic Data and Nuclear Data Tables; 30 (1984) 261

[STR89] **Straver, J.**; Drift Chambers for a F/RCAL Cosmic Ray Calibration Telescope; ZEUS-Note 89-123 (1989)

[STR91] **Straver, J.**; Design, Construction and Beam Tests of the High Resolution Uranium Scintillator Calorimeter of ZEUS; PhD-Thesis University of Amsterdam (1991)

[TIE89] **Tiecke, H., et al.**; Contribution of intrinsic and sampling fluctuations to the total hadronic energy resolution; NIM A277 (1989) 42

[TSU91] **Tsurugai, T.**; private communication (1991)

[VAV57] **Vavilov, P.V.**; Zh. Exper. Teor. Fiz. 32 ; 920 Transl.JETP 5 (1957) 749

[VOG90] **Vogel, W.O., Lohmann, F.O., Woeniger, T., Behrens, U., Hagge, L., Mennerich, F.**; The Eventbuilder of the ZEUS Detector; Computing in high energy physics, AIP Conference Proceedings 209, (1990) 163-169

[WEG89] **Wegener, D.**; Hadronkalorimeter - Entwicklung und Anwendungen; Physikalische Blätter 45, (1989) Nr.9

[Wig86] **Wigmans, R.**; On the Energy Resolution of Uranium- and other Hadron Calorimeters; CERN/EF 86-18, September 1986

[Wig87a] **Wigmans, R.**; On the Energy Resolution of Uranium- and other Calorimeters; NIM A259 (1987) 389

[WOE89] **Woeniger, T.**; Concepts for a Transputer Based Eventbuilder; ZEUS-Note 89-112 November (1989)

[WOE90] **Woeniger, T.**; An Introduction to Transputers; DESY 90-024 March (1990)

[WOL85] **Wolf, G.**; Precision of Q^2, x as determined from the electron and the current jet; ZEUS-Note 85-34 December (1985)

[WOL86] **Wolf, G.**; Hera: Physics, Machine and Experiments; DESY 86-089 August, ISSN 0418-9833 (1986)

[YOS84] **Yost, G.P.**; Lectures on Probability and Statistics; LBL-16993 Rev. 84/HENP/3 June (1985)

[ZEU85] **ZEUS Collaboration**; ZEUS - A Detector for HERA, Letter of Intent (1985)

[ZEU86] **ZEUS Collaboration**; The ZEUS Detector, Technical Proposal (1986)

[ZEU87] **ZEUS Collaboration**; The ZEUS Detector, Status Report 1987 (1987)

[ZOL88] **Zoll, J.**; ZEBRA Reference Manual, MZ Memory Management; Program Library, DD Division (1988)

E Acknowledgements

This thesis had been done in the surrounding of a big experiment with some hundred scientists from several countries involved. During the last three years coming from the eventbuilder online group to the calorimeter calibration and finally to the Monte-Carlo Offline group I had contact to a huge number of people from ZEUS. I thank them all for their support especially to:

- Prof. Dr. E. Lohrmann for enabling me to start my work and the huge effort spent into the permanent support over all the time of my work;
- Dr. R. Klanner helping me to start the physic part of my thesis and providing me the guidance to finish this part successfully;
- all the members which worked in the calibration of the calorimeter with special regards to Jim Crittenden and Tatsu Tsurugai;
- the group around Wolfgang Vogel: Ulf Behrens, Lars Hagge, F.O. Lohmann, J.Mainusch, Thorsten Schlichting and Wolfgang Vogel himself being more like friends than just colleges;
- the offline group with special thanks to Jim Whitmore, Nikolaus Pavel, Paul de Jong, Stefan Schlenstedt and last not least Till Poser answering me all my questions about ADAMO, ZEBRA and all these programs;
- and finally Mike Crombie for converting my basic English into an understandable language.